Measurement of Non-flow Correlations and Elliptic Flow Fluctuations in Au+Au collisions at RHIC

by

Burak Han Alver

B.S., Boğaziçi University (2004)

Submitted to the Department of Physics
in partial fulfillment of the requirements for the degree of

Doctor of Philosophy

at the

MASSACHUSETTS INSTITUTE OF TECHNOLOGY

June 2010

Author . . . .
Department of Physics
May 21st, 2010

Certified by . . . .
Gunther Roland
Associate Professor of Physics
Thesis Supervisor

Accepted by . . . .
Krishna Rajagopal
Associate Department Head for Education

Measurement of Non-flow Correlations and Elliptic Flow Fluctuations in Au+Au collisions at RHIC

by

Burak Han Alver

Submitted to the Department of Physics
on May 21st, 2010, in partial fulfillment of the
requirements for the degree of
Doctor of Philosophy

Abstract

Measurements of collective flow and two-particle correlations have proven to be effective tools for understanding the properties of the system produced in ultrarelativistic nucleus-nucleus collisions at the Relativistic Heavy Ion Collider (RHIC). Accurate modeling of the initial conditions of a heavy ion collision is crucial in the interpretation of these results.

The anisotropic shape of the initial geometry of heavy ion collisions with finite impact parameter leads to an anisotropic particle production in the azimuthal direction through collective flow of the produced medium. In "head-on" collisions of Copper nuclei at ultrarelativistic energies, the magnitude of this "elliptic flow" has been observed to be significantly large. This is understood to be due to fluctuations in the initial geometry which leads to a significant anisotropy even for most central Cu+Cu collisions. This thesis presents a phenomenological study of the effect of initial geometry fluctuations on two-particle correlations and an experimental measurement of the magnitude of elliptic flow fluctuations which is predicted to be large if initial geometry fluctuations are present.

Two-particle correlation measurements in Au+Au collisions at the top RHIC energies have shown that after correction for contributions from elliptic flow, strong azimuthal correlation signals are present at $\Delta\phi = 0$ and $\Delta\phi \approx 120$. These correlation structures may be understood in terms of event-by-event fluctuations which result in a triangular anisotropy in the initial collision geometry of heavy ion collisions, which in turn leads to a triangular anisotropy in particle production. It is observed that similar correlation structures are observed in A Multi-Phase Transport (AMPT) model and are, indeed, found to be driven by the triangular anisotropy in the initial collision geometry. Therefore "triangular flow" may be the appropriate description of these correlation structures in data.

The measurement of elliptic flow fluctuations is complicated by the contributions of statistical fluctuations and other two-particle correlations (non-flow correlations) to the observed fluctuations in azimuthal particle anisotropy. New experimental techniques, which crucially rely on the uniquely large coverage of the PHOBOS detector at RHIC, are developed to quantify and correct for these contributions. Relative elliptic flow fluctuations of approximately 30-40% are observed in 6-45% most central Au+Au collisions at $\sqrt{s_{\mathrm{NN}}} = 200$ GeV. These results are consistent with the predicted initial geometry fluctuations.

Thesis Supervisor: Gunther Roland
Title: Associate Professor of Physics

Contents

1 Introduction

At the extremely high temperatures of the early universe, it is expected that there exists a new phase of strongly interacting matter known as the Quark Gluon Plasma (QGP). Collisions of heavy ions at ultra-relativistic velocities is the only known technique for exploring the properties of matter at such extreme conditions. The highest energy heavy ion collisions to date have been produced at the Relativistic Heavy Ion Collider (RHIC) in Brookhaven National Laboratory (BNL). Angular correlations between the produced particles in heavy ion collisions is one of the most promising probes to study the properties of the hot medium produced at RHIC.

1.1 QCD Phase Diagram

Quantum Electrodynamics (QED) is the underlying theory which leads to all the various phase diagrams (e.g. water, ^{4}He, ^{3}He, liquid crystals) most physicists are accustomed to. The non-abelian nature of Quantum Chromodynamics (QCD) which leads to peculiar phenomena such as asymptotic freedom and confinement should also result in a very rich phase structure. Technical challenges in QCD calculations make it difficult to determine the properties of the QCD phase diagram precisely. Fig. 1.1 [1] shows a qualitative illustration of the phase diagram of QCD matter as a function of temperature, T, and baryon chemical potential, μ_B. The baryon chemical potential is the amount of energy that is added to a system held at constant volume and entropy with the addition of one baryon and can be thought of as a measure of net baryon density.

In the low temperature and long times scales of our daily lives, the only stable strongly interacting matter are nuclei made up of protons and neutrons. Therefore, strongly interacting matter is observed in a mixed phase of droplets of nuclear matter surrounded by regions of vacuum. The required energy to add a baryon to a nucleus is roughly given by the mass of a proton, i.e. $\mu_B \approx 940$ MeV. At temperatures above the nuclear binding energy ($\approx 1 - 10$ MeV), or at low values of μ_B, the nuclear matter evaporates into a hadron gas, similar to the liquid-gas transition of electromagnetically interacting particles.

At extremely high temperatures, where the average momentum transfer in thermal interactions is of orders of many GeV, it is predicted that QCD matter should exist in a phase of weakly interacting partons known as the weakly interacting QGP as a consequence of asymptotic freedom. Lattice calculations performed at $\mu_B = 0$ suggest that a crossover transition from a hadronic to a partonic phase occurs at a much lower temperature of roughly of $T_c \approx 170$ MeV($\approx 2 \times 10^{12}$ K)[2, 3]. Fig. 1.2 [3]

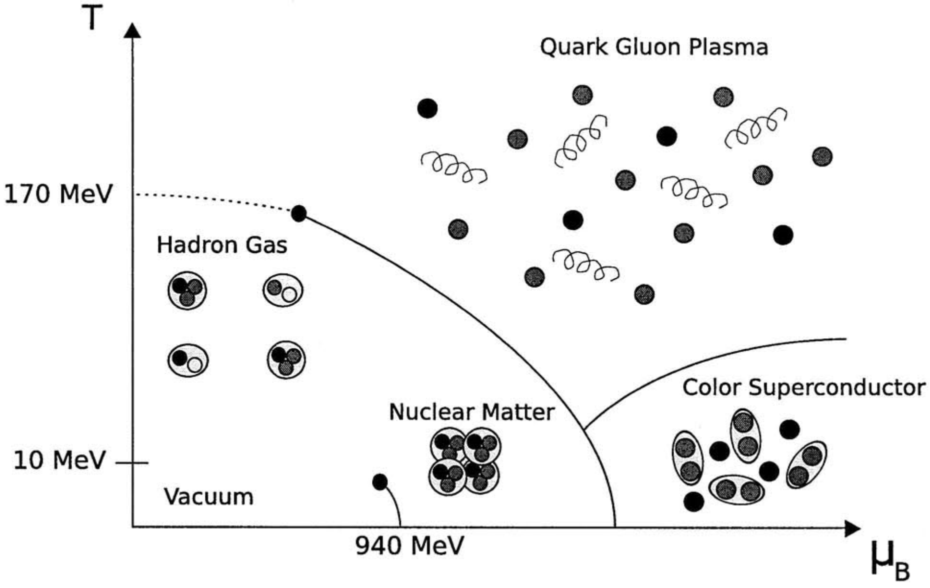

Figure 1.1: Cartoon representation of the different phases of QCD matter as a function of temperature (T) and baryon chemical potential (μ_B) [1].

shows the number of degrees of freedom as a function of temperature in units of the critical temperature. The number of degrees of freedom is observed to increase steeply at the transition and reaches a value of about 80% of the value at the Stefan-Boltzmann limit for an ideal gas non-interacting system of quarks and gluons. In a wide range of gravitational theories, which may be applicable in the study of QCD plasmas due to AdS/CFT correspondence, the number of degrees of freedom in a very strongly interacting system is found to be roughly 3/4 of that in a very weakly interacting system [4, 5]. This observation suggests that the QGP slightly above T_c may have thermodynamic properties vastly different from the weakly interacting QGP at extremely high temperatures[1].

Another region of the QCD phase diagram under recent theoretical study is the limit of high baryon densities at low temperatures. As more and more cold nuclear matter is compressed to a small volume, a first order transition to quark matter is expected to occur at high μ_B. This transition leads to a color superconductor phase due to Cooper pairing of quarks analogous to pairing of electrons into "quasi-bosons" that is responsible for superconductivity in solid-state physics. The difference between the masses of three light quarks leads to a much richer structure than depicted in Fig. 1.1 with different possible pairings of quarks at different T and μ_B (see [6] for a review of the phase structure of color superconductors). Neutron stars are the densest material objects in the universe, with masses of the order of the sun and radii of order ten km, and are the best candidate for observing quark matter at such high densities [7].

Since the transition to quark matter is a first order transition at high μ_B and a

---

[1] It should be noted that the fact that the QGP created at RHIC is strongly coupled was experimentally established before this argument from AdS/CFT correspondence was developed.

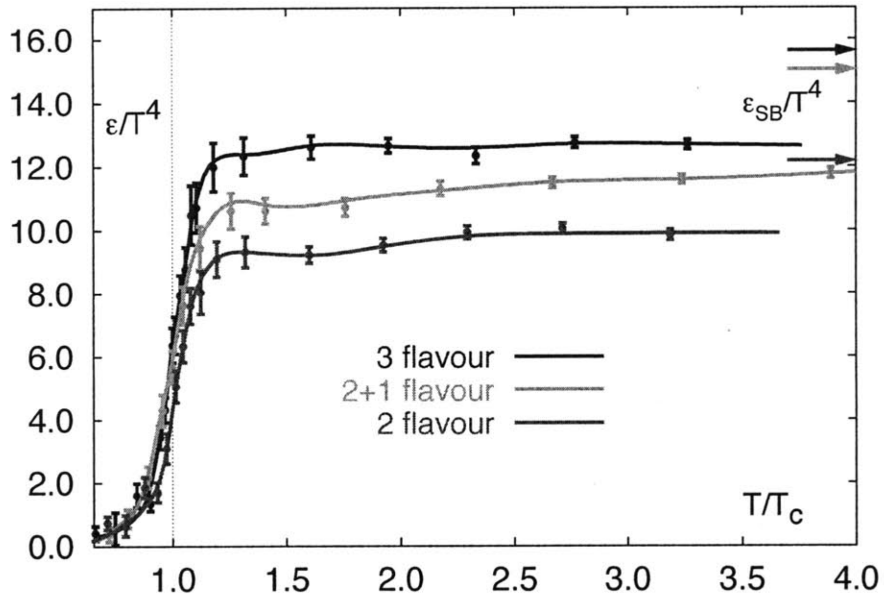

Figure 1.2: The number of degrees of freedom, ϵ/T^4, as a function of temperature, T, in lattice QCD calculations [3]. ϵ_{SB}/T^4 corresponds to the Stefan-Boltzmann limit of an ideal gas non-interacting system. The critical temperature T_c at transition is around 170 MeV.

crossover at $\mu_B = 0$, at least one critical point exists in the QCD phase diagram in between. However, lattice calculations at finite μ_B are complicated by the "fermion sign problem" [8] and the precise location of the critical point is very dependent on the value of the input quark mass [9]. As shown in Fig. 1.3(a), there is a large variation in the theoretical predictions for the location of the critical point. Measurement of fluctuations, which may be enhanced around the critical point, in heavy ion collisions with center of mass energy in the range $5 < \sqrt{s_{\rm NN}} < 40$ is the most promising experimental approach to discover the QCD critical point [10].

1.2 Relativistic Heavy Ion Collisions

A large amount of energy can be dumped into a very small volume by colliding heavy ions at relativistic energies. Fixed target experiments at the Alternating Gradient Synchrotron (AGS) at BNL and the Super Proton Synchrotron (SPS) at European Organization for Nuclear Research (CERN) have recorded collisions of light ions up to Au+Au and Pb+Pb at center-of-mass energies per nucleon pair ($\sqrt{s_{\rm NN}}$) from 2 to 17 GeV. The highest energies achieved to date have been at RHIC, where billions of d+Au, Cu+Cu, and Au+Au collisions have been recorded at energies up to $\sqrt{s_{\rm NN}} = 200$ GeV. Pb+Pb collisions at the Large Hadron Collider (LHC) are

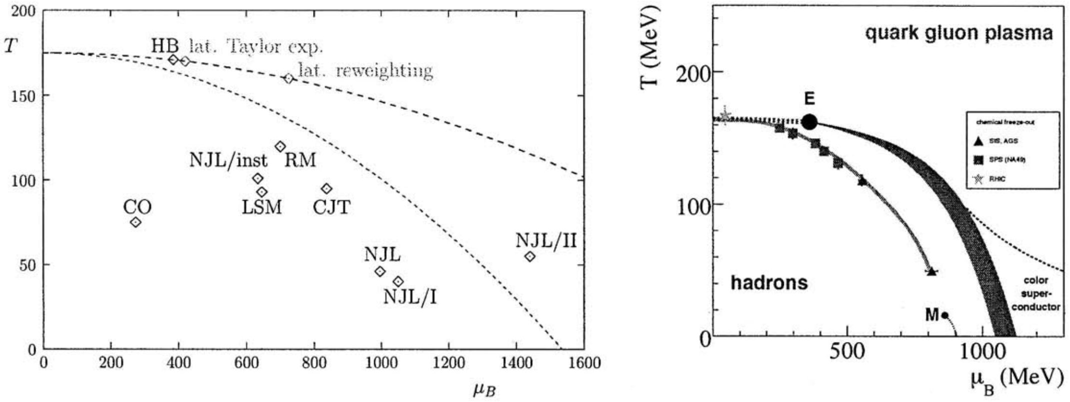

(a) (b)

Figure 1.3: QCD phase diagram as a function of temperature (T) and baryon chemical potential (μ_B). (a) Theoretical (models and lattice) predictions for the location of the critical point [11]. (b) The hadronic chemical freeze-out points in heavy ion collisions in the energy range $\sqrt{s_{\rm NN}}$ = 0.4–200 GeV obtained from statistical model fits to relative yields of different particle species [12].

expected to begin at the end of 2010 and reach energies of up to $\sqrt{s_{\rm NN}}$ = 5.5 TeV.

Heavy ion collisions are pictured in terms of a number of stages ending with particles observed in the detectors located around the collision points. Various experimental observables have been measured, relating detectable signals to the properties of the matter at the different stages of collisions. The current understanding of the different stages of a Au+Au collision at $\sqrt{s_{\rm NN}}$ = 200 GeV is outlined below along with a brief description of the supporting experimental evidence.

For Au+Au collisions at $\sqrt{s_{\rm NN}}$ = 200 GeV, Lorentz-contracted nuclei pass through each other in roughly $\tau = 0.1$ fm/c$\approx 3 \times 10^{-25}$ s. The vacuum left behind is filled with a color field conveying the attraction of the two disintegrating nuclei. The energy of the color field relaxes through the production of matter and antimatter. The impact parameter of the collision roughly defines how many of the total 394 nucleons in the two gold nuclei participate in a collision ($N_{\rm part}$), how many binary nucleon-nucleon collisions occur ($N_{\rm coll}$) and how the initial energy density is distributed in the collision region. Collisions with a small impact parameter are referred to as "central" collisions, whereas collisions with a large impact parameter are denoted "peripheral".

The photons produced in the initial collisions are expected to be unaffected by the later stages of the collision. Measurements of direct photon spectra show that the photon yield at high $p_{\rm T}$ scales with the number of binary collisions, consistent with this expectation [13]. The multiplicity of charged particles produced in the collision, however, is observed to scale with the number of participating nucleons [14]. Furthermore the multiplicity per participant pair is found to be very close to the value observed in $e^+ + e^-$ collisions [14]. These findings suggest that the total entropy of

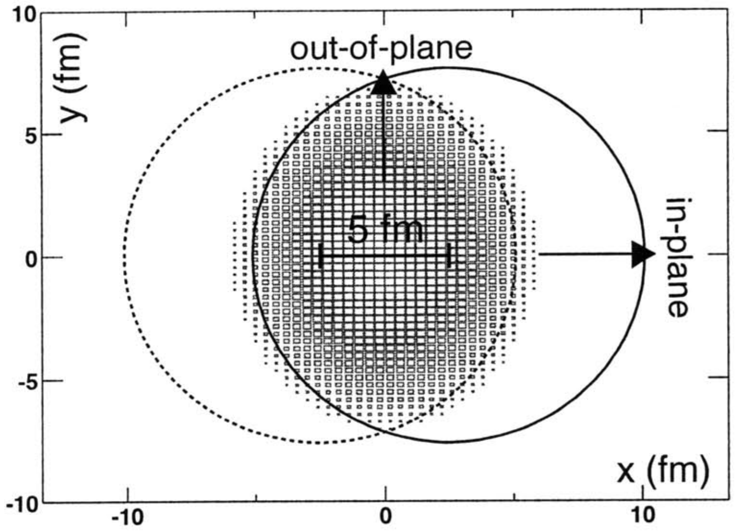

Figure 1.4: Average transverse overlap density for Au+Au collisions at $\sqrt{s_{\mathrm{NN}}} = 200$ GeV with impact parameter $b = 5$ fm calculated in a Glauber Model. Impact parameter and beam directions are given by the x and z coordinates, respectively [15].

the system is defined early on in the collision and does not increase significantly in the later stages.

For collisions at finite impact parameter, the initial geometry of the collision region is anisotropic in the azimuthal direction[2] as illustrated in Fig. 1.4 [15]. After the initial binary collisions, the interacting system reaches local thermal equilibrium and pressure gradients arise. The pressure gradients are steeper in the direction of the impact parameter leading to an anisotropy in the momentum distribution of particles, referred to as elliptic flow. Elliptic flow is quantified by the second Fourier coefficient, v_2, of the azimuthal particle distribution relative to the reaction plane, defined by the impact parameter and the beam axis (the xz-plane in Fig. 1.4). The measurement of elliptic flow in Au+Au collisions at $\sqrt{s_{\mathrm{NN}}} = 200$ GeV suggests that local thermal equilibrium is established in $\tau < 2$ fm/c [16]. The energy density of the system at the time of equilibration is estimated to be greater than 3 GeV/fm^3 from the measurements of charged particle multiplicity and transverse momentum distributions [17].

The expansion of the thermalized system is found to be well described by relativistic hydrodynamic models with very low viscosity [18], i.e. the dynamic properties of the medium resemble the conditions of a liquid rather than a gas. Another interesting feature of the liquid-like matter produced at RHIC is discovered by studying the azimuthal anisotropy of final state particles for different particle species. As shown

---

[2] See Appendix A for the coordinate system conventions.

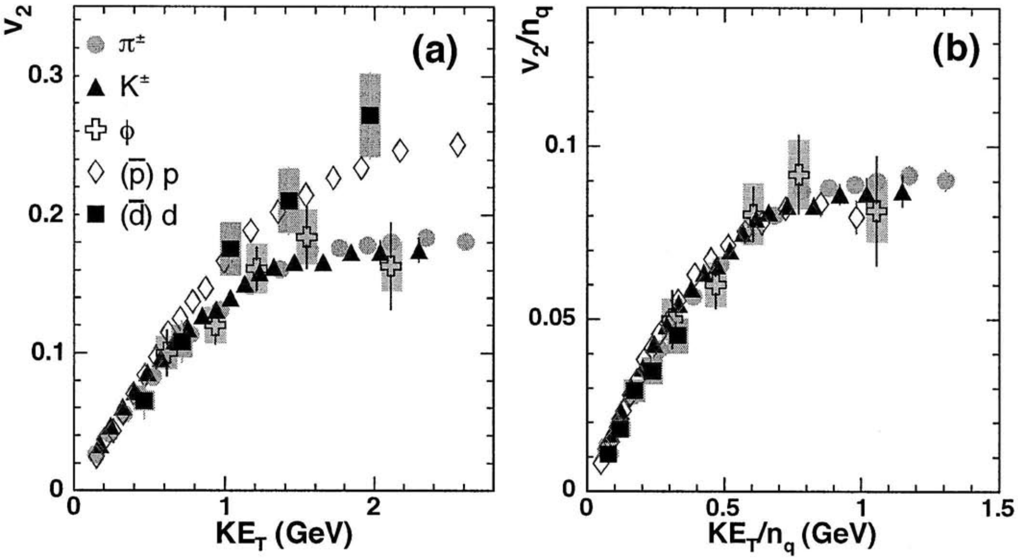

Figure 1.5: (a) Elliptic flow, v_2, as a function of transverse kinetic energy, KE_T, for several identified species in 20-60% most central Au+Au collisions at $\sqrt{s_{\mathrm{NN}}} = 200$ GeV. (b) The same data in panel (a) presented with both axes scaled by $1/n_q$, the number of constituent quarks [19].

in Fig. 1.5 [19], the magnitude of elliptic flow for different particle species shows a striking scaling with the number of constituent quarks, $n_q = 2$ for mesons and $n_q = 3$ for (anti-)baryons. This result indicates that the flowing thermalized system is best described in terms of partonic degrees of freedom.

It is possible to "probe" the hot and dense medium produced in heavy ion collisions via measurements of high p_{T} particles. High p_{T} partons are expected to be produced through hard processes in the initial binary nucleon collisions. If these partons hadronize with little interaction after their production, the number of produced hadrons at high p_{T} should scale with number of binary collisions similar to the number of high p_{T} photons. The number of produced hadrons at high p_{T} is, in fact, observed to be significantly reduced compared to this expectation (up to 5 times in most central Au+Au collisions) indicating that the medium is opaque for high p_{T} partons [20, 21, 22]. A more differential study of high p_{T} probes can be made by measuring azimuthal correlations between particle pairs at high p_{T}. Figure 1.6 [23] shows the azimuthal distribution of hadrons with $p_{\mathrm{T}} > 2$ GeV correlated to a trigger particle with $p_{\mathrm{T}} > 4$ GeV. Pairs of particles from the same jet result in a correlation near $\Delta\phi = 0$, while pairs taken from back-to-back jets are observed at $\Delta\phi \approx \pi$. The near-side correlation structure is found to be similar for the p+p and Au+Au systems, while the away-side correlation is absent in central Au+Au events [24]. These observations along with the elliptic flow results discussed above indicate that an opaque, strongly interacting partonic matter is created in the high energy Au+Au collisions at RHIC.

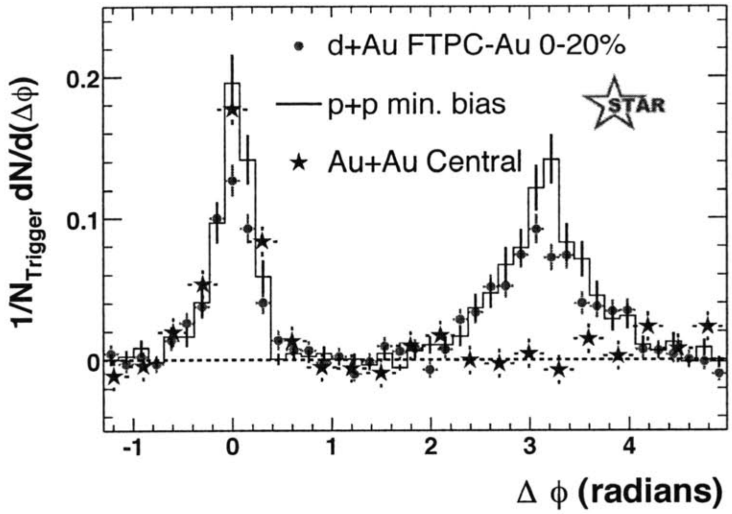

Figure 1.6: Azimuthal correlations between pairs of high-p_T hadrons in p+p, d+Au, and Au+Au collisions at $\sqrt{s_{NN}} = 200$ GeV [23].

As the collision system expands and cools, the partonic matter is transformed into hadrons. These hadrons initially go through inelastic collisions as the system keeps cooling down. When the temperature drops below a certain point, inelastic collisions between hadrons cease and the yield of different particle species is completely defined. This stage of the collision is therefore referred to as "chemical freeze-out". As shown in Fig. 1.7(a) [25], statistical models using the grand canonical ensemble with only two free parameters are very successful in describing the relative abundance of different particle species. Fig. 1.3(b) [12] shows the statistical model estimates on the temperature and baryon chemical potential values at chemical freeze-out for heavy ion collisions at different center-of-mass energies. For Au+Au collisions at $\sqrt{s_{NN}} = 200$ GeV, the best fit results yield a chemical freeze-out temperature of roughly $T \approx 160$ MeV [25].

After the chemical freeze-out, as the system expands and cools further, hadrons continue to undergo elastic collisions. The time at which the produced particles cease colliding is known as "kinetic freeze-out". Fits to charged hadron transverse momentum spectra based on the blast-wave models yield an estimate of the kinetic freeze-out temperature at roughly $T \approx 105$ MeV [26, 27] (see Fig. 1.7(b) [27]).

Although a crude understanding of the different stages of heavy ion collisions exist, there is currently no model of heavy ion collisions which is able to predict all aspects of the collision in a self-consistent manner. The theoretical understanding of heavy ion collisions relies on a mosaic of small models which have their own assumptions, adjusted parameters and quantitative uncertainties. As these theoretical models are developed to become more and more realistic, they need to be tested with more precise and differential experimental measurements. The latest experimental and theoretical developments in the field of heavy ion physics are presented in the "Quark

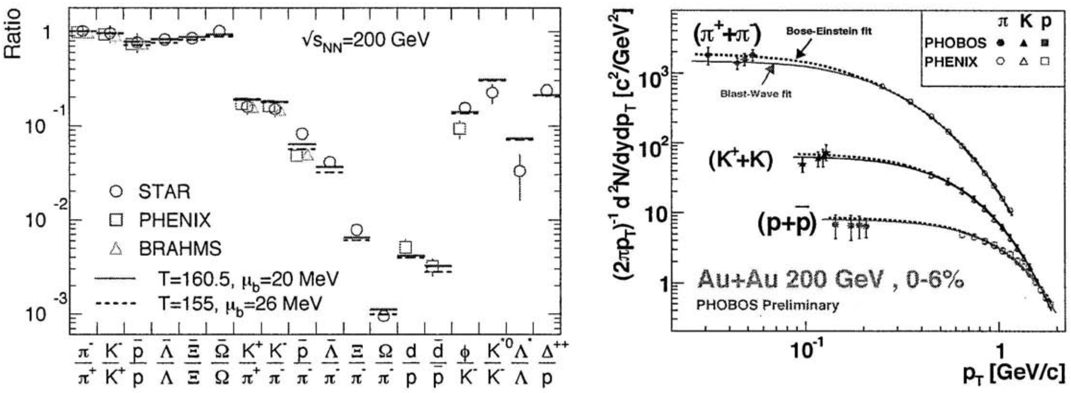

(a) (b)

Figure 1.7: Estimation of the chemical and kinetic freeze-out temperatures for Au+Au collisions at $\sqrt{s_{\mathrm{NN}}} = 200$ GeV. (a). Experimental results on relative hadron yields and statistical model fits to the data used to estimate the chemical freeze-out temperature [25]. (b) Identified transverse momentum spectra for low p_{T} particles. Blast-Wave (solid line) and Bose-Einstein (dotted line) parameterizations are fitted over the PHENIX data to estimate the kinetic freeze-out temperature [27, 28].

Matter" international conference series [29, 30, 31, 32]. A more thorough overview of relativistic heavy ion physics at RHIC can also be found in the "white papers" published by the four RHIC experiments [17, 23, 33, 34].

1.3 Two Puzzles in Flow and Correlation Studies: Outline of this Thesis

As discussed in the previous section, differential studies of different observables are required to arrive at a complete and coherent theory of heavy ion collisions. The goal of this thesis is to resolve two puzzling results which have arisen in the systematic study of elliptic flow and two-particle correlations and improve the understanding of the early stages of heavy ion collisions.

The first puzzle arose with the measurement of elliptic flow in Cu+Cu collisions. Fig. 1.8 [35] shows the elliptic flow signal in Au+Au and Cu+Cu collisions at $\sqrt{s_{\mathrm{NN}}} = 200$ GeV as a function number of participating nucleons. Since elliptic flow is driven by the azimuthal anisotropy in the initial geometry of the collision, it was predicted that the elliptic flow signal should be small for most central collisions where the initial geometry is expected to be roughly circular. For the most central Cu+Cu collisions, however, the elliptic flow signal is observed to be significantly large [35].

The second surprising observation is the rich structure in angular correlation measurements in heavy ion collisions. Fig. 1.9 [36] shows the correlated yield with respect to a trigger particle with $p_{\mathrm{T}} > 2.5$ GeV in p+p collisions, modeled by PYTHIA, and

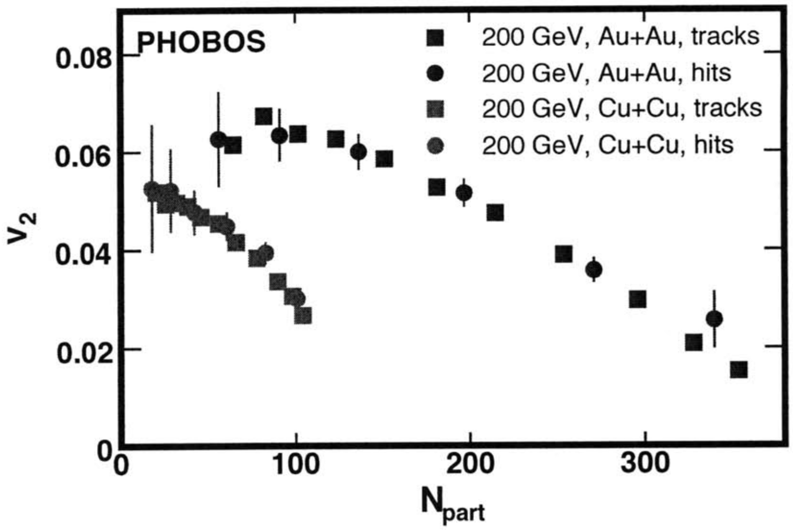

Figure 1.8: Elliptic flow parameter v_2 as a function of number of participating nucleons in Au+Au (blue) and Cu+Cu (red) collisions at $\sqrt{s_{\rm NN}} = 200$ GeV [35].

0-30% most central Au+Au events[3] at $\sqrt{s_{\rm NN}} = 200$ GeV as a function of pseudorapidity and azimuth separations, $\Delta\eta$ and $\Delta\phi$, between particle pairs. A very rich correlation structure is observed in Au+Au collisions in comparison the p+p system with excess yield of correlated particles at $\Delta\phi = 0°$ and $\Delta\phi \approx 120°$ extending out to $\Delta\eta > 2$. These structures, referred to as the "ridge" and "broad away side", have been extensively studied experimentally [36, 37, 38, 39, 40, 41] and various theoretical models have been proposed to understand their origin [42, 43, 44, 45, 46, 47, 48]. However, none of the theoretical models successfully describe all of the observed experimental features of these structures [49].

It has been proposed that the observed elliptic flow results for Cu+Cu and Au+Au collisions can be reconciled if event-by-event fluctuations in the initial geometry are considered [35]. The anisotropy of the initial geometry can be characterized by the eccentricity of the transverse shape of the initial nuclear overlap region [50]. In a Glauber model description of the colliding nuclei, the eccentricity of the region defined by the event-by-event distribution of nucleon-nucleon interaction points is finite even for the most the central collisions. The event-by-event fluctuations in the shape of the interaction region is found to have a larger effect in the smaller Cu+Cu system. A detailed description of the effect of initial geometry fluctuations on elliptic flow results is presented in Ch. 2.

In Ch. 3, it is proposed that the fluctuations in the initial collision geometry may also be the key to understanding the source of the ridge and broad away side structures in two-particle correlation measurements. Event-by-event fluctuations can re-

---

[3] The contribution of elliptic flow to two-particle correlations is subtracted to obtain the correlated yield in Au+Au collisions.

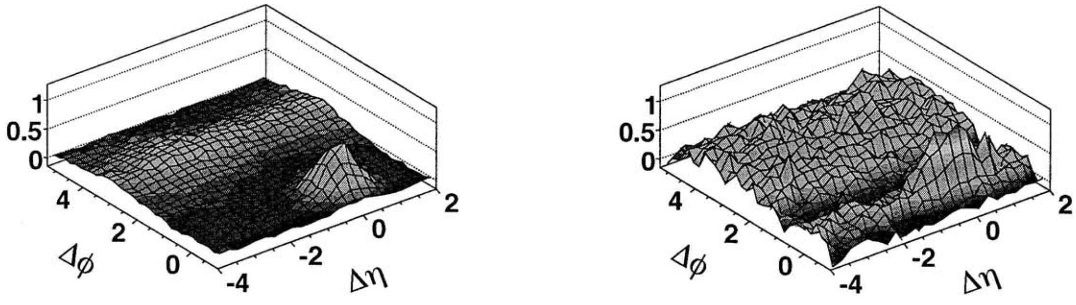

(a)

(b)

Figure 1.9: Correlated yield as a function of $\Delta\eta$ and $\Delta\phi$ for (a) PYTHIA p+p model and (b) 0-30% central Au+Au data at $\sqrt{s_{\mathrm{NN}}} = 200$ GeV with respect to a trigger particle with $p_{\mathrm{T}}^{trig} > 2.5$ GeV/c [36].

sult in a triangular anisotropy in the initial collision geometry of heavy ion collisions, which can lead to a triangular anisotropy in particle production. The concepts of "triangularity" and "triangular flow", analogous to eccentricity and elliptic flow, are introduced to quantify this effect. The relation between triangular flow and the ridge and broad away side structures are investigated using A Multi-Phase Transport (AMPT) model.

If initial geometry fluctuations are present and elliptic flow is driven by the eccentricity of the initial collision region, an event-by-event measurement of elliptic flow should exhibit sizable fluctuations even at fixed impact parameter. Chapters. 4-7 describe the experimental evaluation of this prediction using the PHOBOS detector at RHIC. The experimental setup of the PHOBOS detector and the triggering, reconstruction, characterization and selection of collision events are summarized in Ch. 4. The measurement of elliptic flow fluctuations is complicated due to statistical fluctuations from stochastic particle production and correlations between particles other than flow, referred to as non-flow. The analysis technique to account for statistical fluctuations and non-flow correlations and measure underlying elliptic flow fluctuations is introduced in Ch. 5. Dynamic v_2 fluctuations including contributions from elliptic flow fluctuations and non-flow correlations are measured in Ch. 6. The magnitude of non-flow correlations and results on elliptic flow fluctuations are calculated in Ch. 7. The conclusions of the thesis are presented in Ch. 8.

2 Eccentricity and Elliptic Flow

Anisotropies in particle momentum distributions relative to the reaction plane, often referred to as anisotropic collective flow, have been studied in heavy ion collisions for more than a decade. Traditionally, azimuthal anisotropy in particle production is characterized by a Fourier decomposition with respect to the reaction plane angle, ψ_R, [51]

$$\frac{1}{N}\frac{\mathrm{d}N}{\mathrm{d}\phi} = \frac{1}{2\pi}\left\{1 + \sum_n 2v_n \cos(n(\phi - \psi_R))\right\}. \tag{2.1}$$

The sine terms in this expansion are dropped since the particle production is on average symmetric around the reaction plane. The second Fourier coefficient, v_2, characterizes elliptic flow which arises from the anisotropy in the initial collision geometry.

The anisotropy of the collision geometry is commonly quantified by the eccentricity,

$$\varepsilon = \frac{\langle y^2 - x^2 \rangle}{\langle y^2 + x^2 \rangle}, \tag{2.2}$$

where x and y are the transverse coordinates along and perpendicular to the reaction plane angle, respectively (see Fig. 1.4). The eccentricity of the initial collision region cannot be determined directly. However, models of the very early stages of a collision can be used to relate the fractional cross-section of collision events to relevant variables of the initial geometry. The most commonly used approach is to apply a Glauber model description of the colliding nuclei to determine the positions of nucleons which participate in the collision.

2.1 The Physics of Elliptic Flow

In 1992, Ollitrault predicted that "anisotropies in transverse-momentum distributions [will] provide an unambiguous signature of transverse collective flow in ultrarelativistic nucleus-nucleus collisions" [50]. He applied ideal hydrodynamic calculations to quantify this effect for different initial conditions and equations of state. In 1994, Voloshin proposed Fourier analysis of azimuthal distributions as an appropriate tool to study different transverse flow effects [51]. He coined the term "elliptic flow" to the second term in the Fourier expansion. Elliptic flow signal has since been measured for heavy ion collisions at the AGS [52, 53], SPS [54] and RHIC [55].

Elliptic flow is caused by the rescattering of particles produced in the initial nucleon-nucleon collisions. Therefore at low densities, the elliptic flow signal should

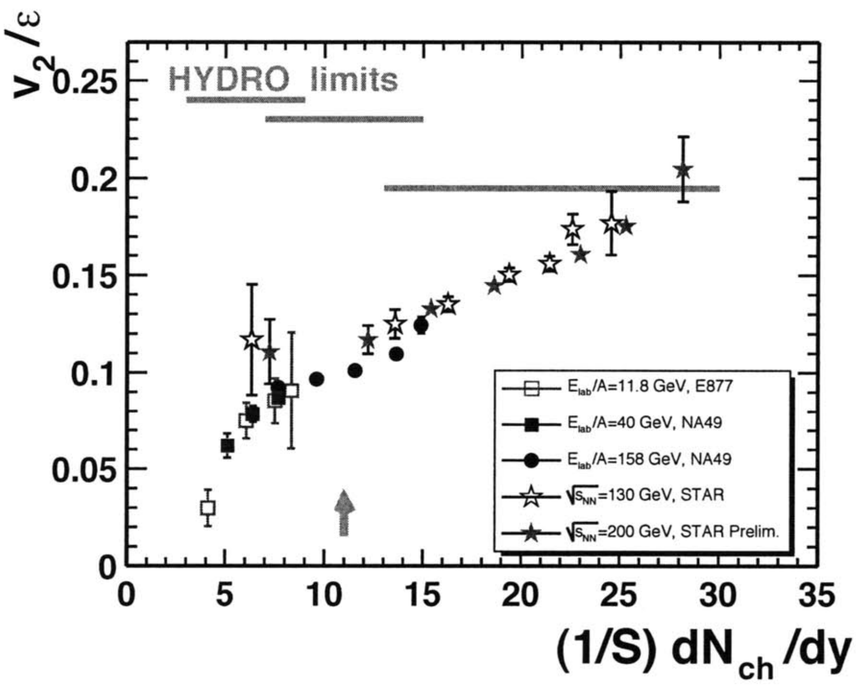

Figure 2.1: Elliptic flow scaled by eccentricity, v_2/ε, as a function of particle density in the transverse plane, $1/S(\mathrm{d}N/\mathrm{d}y)$, for different collision systems, center-of-mass energies and centrality ranges [54]. The initial overlap area, S, and eccentricity are taken from Glauber model calculations.

be proportional to the particle density in the transverse plane [56, 57]. At the limit of very high density and vanishingly small mean free path, elliptic flow signal is expected to saturate at a value imposed by hydrodynamic calculations. In addition, as the elliptic flow should be zero for an azimuthally symmetric system, for small anisotropies in the initial geometry, elliptic flow should be proportional to eccentricity. It was shown in the very first hydrodynamic calculation by Ollitrault that the proportionality between elliptic flow and eccentricity holds well even for rather large values of ε [50].

Based on these observations, Voloshin and Poskanzer proposed that the physics of elliptic flow can be best studied by plotting elliptic flow scaled by eccentricity, v_2/ε, as a function of particle density in the transverse plane, $1/S(\mathrm{d}N/\mathrm{d}y)$, where the initial overlap area, S, and eccentricity, ε are taken from Glauber model calculations [57]. The idea of the plot, shown in Fig. 2.1 [54] for elliptic flow results from AGS, SPS and RHIC experiments, is to compare the results obtained at different collision energies, with different projectiles, and at different centralities. A non-smooth dependence on this plot could indicate the onset of a new physics mechanism and a saturation at high densities may signal an approach to ideal hydrodynamic evolution.

Figure 2.1 shows that for the most central collisions at the top RHIC energies, the elliptic flow value reaches the predicted hydrodynamic limit. This observation lead to the conclusion that heavy ion collisions satisfy the assumptions made in hydrodynamic calculations of very early thermalization and interactions near the zero mean-free path limit [17, 23, 33]. It will be interesting to see if heavy ion collisions at the much higher energy of $\sqrt{s_{\rm NN}}$=5.5 TeV at the LHC, will indeed show the saturation expected from these calculations.

In the recent years, much experimental and theoretical work has been put in to refine the different components of Fig. 2.1. (For a review of recent developments, see [58, 59].) Quantum mechanical arguments and AdS/CFT correspondence have been shown to suggest a lower bound on the magnitude of viscosity [60]. Hydrodynamic calculations which implement finite mean-free path, have shown the elliptic flow results to be very sensitive to the viscosity of the system even at the conjectured lower limit [61]. The effects of the hadronization stage on elliptic flow have been investigated in more detail [62]. It was shown that ideal hydrodynamic calculations, if tuned to describe the transverse momentum spectra, yield larger elliptic flow values than obtained previously [63]. Different approaches used to quantify the initial geometry parameters have shown a large uncertainty in the value of eccentricity. The measured value of elliptic flow has been found to be sensitive to event-by-event fluctuations, which as this thesis demonstrates are significantly large. Both theoretical and experimental uncertainties need to be reduced to evaluate the importance of these different effects and to extract the thermodynamic properties of the medium precisely. The results presented in this thesis provide an important ingredient in reducing the uncertainties arising from eccentricity calculations and elliptic flow fluctuations.

2.2 Implementation of a Glauber Model

Glauber models are used to calculate geometric quantities in the initial state of heavy ion collisions, such as impact parameter, number of participating nucleons and initial eccentricity. These models fall in two main classes. (For a recent review, see [64].) In the so called "optical" Glauber calculations, a smooth matter density is assumed, typically described by a Fermi distribution in the radial direction and uniform over the solid angle. In the Monte Carlo based models, individual nucleons are stochastically distributed event-by-event and collision properties are calculated by averaging over multiple events. These two type of models lead to mostly similar results for simple quantities such as the number of participating nucleons ($N_{\rm part}$) and impact parameters (b), but give different results in quantities where event-by-event fluctuations are significant [64, 65].

The PHOBOS experiment uses a Monte Carlo based Glauber Model implementation [66]. The model calculation is performed in two steps. First, the nucleon positions in each nucleus are stochastically determined. Then, the two nuclei are "collided", assuming the nucleons travel in a straight line along the beam axis (eikonal approximation) such that nucleons are tagged as wounded (participating) or spectator.

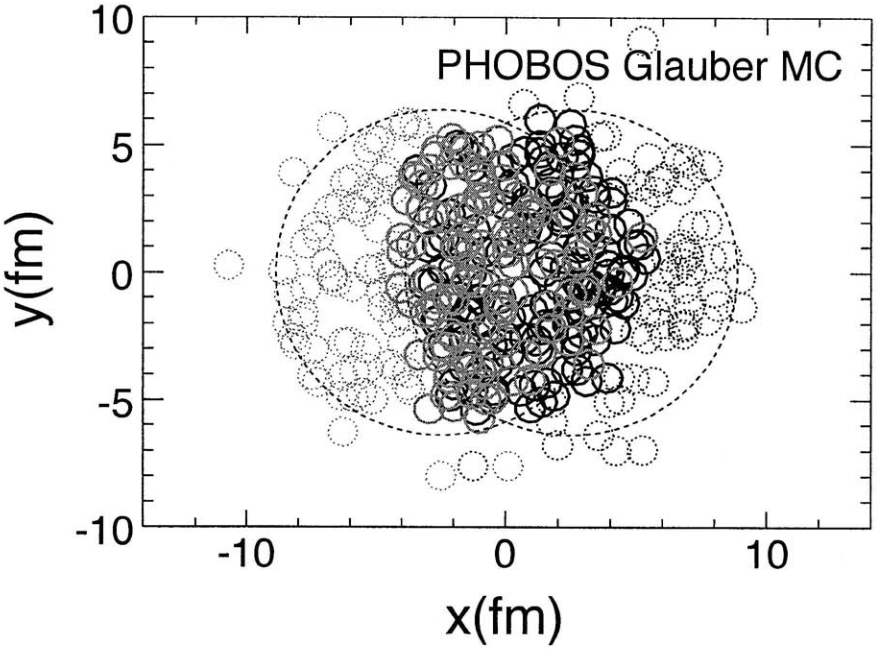

Figure 2.2: Distribution of nucleons on the transverse plane for a typical Au+Au simulation event at $\sqrt{s_{\mathrm{NN}}} = 200$ GeV. Wounded nucleons (participants) are indicated as solid circles, while spectators are dotted circles [66].

The position of each nucleon in the nucleus is determined according to a probability density function. In a quantum mechanical picture, the probability density function can be thought of as the single-particle probability density and the position as the result of a position measurement. In the determination of the nucleon positions in a given nucleus, it is possible to require a minimum inter-nucleon separation (d_{min}) between the centers of the nucleons.

The probability distribution is typically taken to be uniform in azimuthal and polar angles. The radial probability function is modeled from nuclear charge densities extracted in low-energy electron scattering experiments [67]. The nuclear charge density is usually parameterized by a Fermi distribution with three parameters:

$$\rho(r) = \rho_0 \frac{1 + w(r/R)^2}{1 + exp(\frac{r-R}{a})}, \tag{2.3}$$

where ρ_0 is the nucleon density, R is the nuclear radius, a is the skin depth and w corresponds to deviations from a spherical shape. The overall normalization (ρ_0) is not relevant for this calculation. The values of the parameters for a gold nucleus are R=6.38 fm, a=0.535 fm, q=0.535 fm, w=0.0 fm.

The impact parameter of the collision is chosen randomly from a distribution $\mathrm{d}N/\mathrm{d}b \propto b$ up to some large maximum b_{max} with $b_{\mathrm{max}} \simeq 20\,\mathrm{fm} > 2R_A$. The centers of the nuclei are calculated and shifted to $(-b/2, 0, 0)$ and $(b/2, 0, 0)$, where the

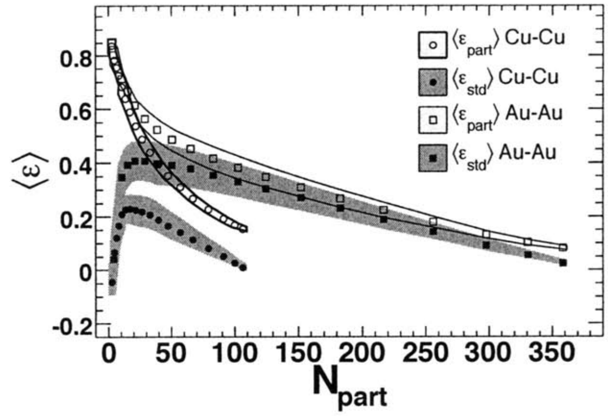

Figure 2.3: The average eccentricity defined in two ways, $\varepsilon_{\text{part}}$ and ε_{std} $(=\varepsilon_{\text{RP}})$, as a function of number of participating nucleons, N_{part}, for simulated Cu+Cu and Au+Au collisions at $\sqrt{s_{\text{NN}}} = 200$ GeV [35].

z-axis points along the beam direction. (The longitudinal coordinate does not play a role in the calculation.)

The inelastic nucleon-nucleon cross section (σ_{NN}), which is only a function of the collision energy is extracted from p+p collisions. At the top RHIC energy of $\sqrt{s_{\text{NN}}} = 200$ GeV, it is found to be $\sigma_{\text{NN}} = 42$ mb. The "ball diameter" is defined as:

$$D = \sqrt{\sigma_{NN}/\pi}. \tag{2.4}$$

Two nucleons from different nuclei are assumed to collide if their relative transverse distance is less than the ball diameter. If no such nucleon–nucleon collision is registered for any pair of nucleons, then no nucleus–nucleus collision occurred. A typical Glauber Monte Carlo event is shown in Fig. 2.2 [66].

2.3 Characterization of the Collision Eccentricity

The positions of the participating nucleons obtained with the PHOBOS Glauber Monte Carlo implementation can be used to estimate transverse energy density distribution in the very early stages of a heavy ion collision. The eccentricity of the region defined by the participating nucleons can be calculated with respect to the reaction plane angle as

$$\varepsilon_{\text{RP}} = \frac{\langle y^2 \rangle - \langle x^2 \rangle}{\langle y^2 \rangle + \langle x^2 \rangle}, \tag{2.5}$$

where the averages are calculated over the positions of participating nucleons. This way of quantifying the initial anisotropy, referred to as "reaction plane eccentricity"[1],

---

[1] Reaction plane eccentricity is also referred to as standard eccentricity, since it was the original was of quantifying the initial anisotropy.

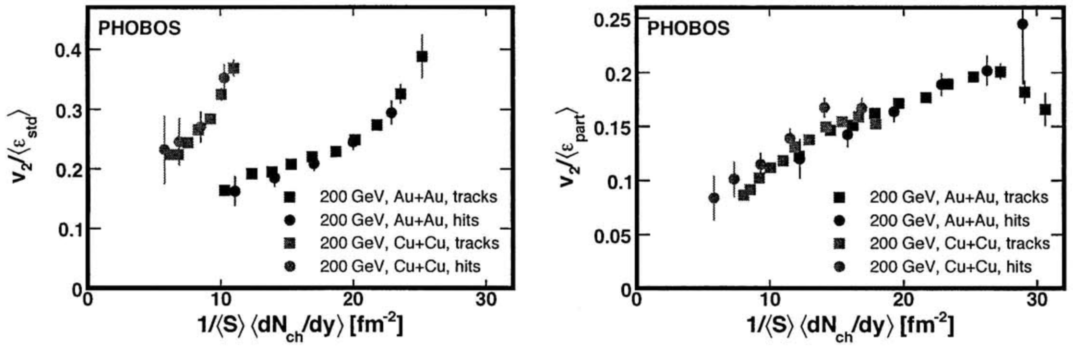

(a) (b)

Figure 2.4: Elliptic flow scaled by eccentricity, v_2/ε, as a function of particle density in the transverse plane, $1/S(\mathrm{d}N/\mathrm{d}y)$ for Cu+Cu and Au+Au collisions at $\sqrt{s_{\mathrm{NN}}} = 200$ GeV using (a) the reaction plane, $\varepsilon_{\mathrm{RP}}$, and (b) participant, $\varepsilon_{\mathrm{part}}$, eccentricity definitions [35].

has an intrinsic assumption that the event-by-event fluctuations in the Glauber model interpretation are not realistic and each collision is, in fact, symmetric with respect to the reaction plane angle.

For a Glauber Monte Carlo event, the minor axis of eccentricity of the region defined by the participating nucleons does not necessarily point along the reaction plane vector. If Glauber Monte Carlo calculations are taken to be physically relevant event-by-event, it should be expected that elliptic flow should develop relative to this tilted axis rather than strictly the reaction plane direction. "Participant eccentricity" is calculated from the positions of participating nucleons with no reference to the reaction plane angle as (see Appendix A in [65] for a derivation)

$$\varepsilon_{\mathrm{part}} = \frac{\sqrt{(\sigma_y^2 - \sigma_x^2)^2 + 4(\sigma_{xy})^2}}{\sigma_y^2 + \sigma_x^2}, \tag{2.6}$$

where σ_x^2, σ_y^2, and σ_{xy} are the event-by-event (co-)variances of the participant nucleon distributions projected on the transverse axes, x and y.

The average value of eccentricity calculated with the two definitions is plotted as a function of centrality for Au+Au and Cu+Cu collisions in Fig. 2.3. The two methods of calculating eccentricity is seen to differ significantly for the smaller Cu+Cu system.

2.4 Evaluation of Different Eccentricity Models

Until 2005, the reaction plane eccentricity (see Eq. 2.5) was used to characterize initial collision geometry. The comparison of $v_2/\varepsilon_{\mathrm{RP}}$ in Cu+Cu and Au+Au collisions, shown in Fig. 2.4(a), yielded a huge discrepancy between the two systems. The significantly large v_2 in the smaller Cu+Cu system, in particular for the most central collisions had not been anticipated.

The PHOBOS collaboration suggested that the results for Cu+Cu and Au+Au collisions can be reconciled if event-by-event fluctuations in the initial eccentricity are considered [35]. The participant eccentricity, defined in Eq. 2.6, was introduced to account for these fluctuations. As discussed in the previous section, taking into account the fluctuations in the initial geometry has a large effect for the smaller Cu+Cu system. As shown in Fig. 2.4(b), elliptic flow scaled by participant eccentricity, $v_2/\varepsilon_{\text{part}}$, is indeed in agreement for the Cu+Cu and Au+Au systems.

Reaction plane and participant eccentricity definitions have different underlying assumptions on "the picture of a nucleus at E=100 GeV per nucleon taken in 10^{-25} seconds." The success of participant eccentricity at unifying elliptic flow results for different collision systems suggests that the colliding nuclei can be pictured as a collection of nucleons, the positions of which are "measured" in the collision process, similar to the Glauber Monte Carlo event shown in Fig. 2.2. An implication of this conclusion is that eccentricity of collisions will show event-by-event fluctuations, even at fixed impact parameter. Measurement of elliptic flow fluctuations presented in this thesis provides a direct test of this prediction.

3 Triangularity and Triangular Flow

Measurements of two-particle angular correlations in heavy ion collisions are sensitive to various phenomena including collective flow of the produced medium, the interaction of high p_{T} partons with the flowing medium and the hadronization process. It is customary to subtract the contribution of elliptic flow to two-particle correlations to study the correlation structures in the context of elementary collisions.

Comparison of elliptic-flow-subtracted azimuthal correlations in Au+Au collisions to the p+p data shows an excess correlated yield at $\Delta\phi = 0$ and $\Delta\phi \approx 120$, referred to as the "ridge" and "broad away side", respectively. The ridge and broad away side features in heavy ion collisions were first observed for high p_{T} triggered correlations at short range in pseudorapidity [37]. Since then, they have been extensively studied experimentally [36, 37, 38, 39, 40, 41]. In particular, it was shown that these structures extend out to pseudorapidity separations of $\Delta\eta = 4$ [36]. Furthermore, the same structures can be seen in inclusive two-particle correlation results in Ref. [68] to extend out to $\Delta\eta = 5.5$ if the second Fourier component of azimuthal correlations is subtracted. The presence of these correlations at such large rapidity separations suggests that they must arise at very early times in the collision process. If the fluctuations in the initial collision geometry are considered, it may be possible to explain these correlation structures as a next order collective flow effect.

Event-by-event fluctuations may result in a triangular anisotropy in the initial collision geometry of heavy ion collisions, which it turn leads to a triangular anisotropy in particle production [69]. This effect can be quantified by introducing the new variables participant triangularity and triangular flow analogous to participant eccentricity and elliptic flow. A Multi-Phase Transport (AMPT) model, which uses Glauber type initial conditions and successfully reproduces qualitative features of elliptic flow results in data provides a good testing ground to assess the connection between triangularity and the ridge and broad away side features in two-particle correlations.

3.1 Triangularity in a Glauber Model

The implementation of a Glauber Model Monte Carlo and the calculation of participant eccentricity in the model are described in Sections 2.2 and 2.3. The definition of eccentricity[1] can be easily generalized to anisotropy measures in higher order if the coordinate system in the Glauber Monte Carlo calculation is shifted to the center

---

[1] For the rest of this chapter, "eccentricity" refers to participant eccentricity and is denoted ε_2, exclusively.

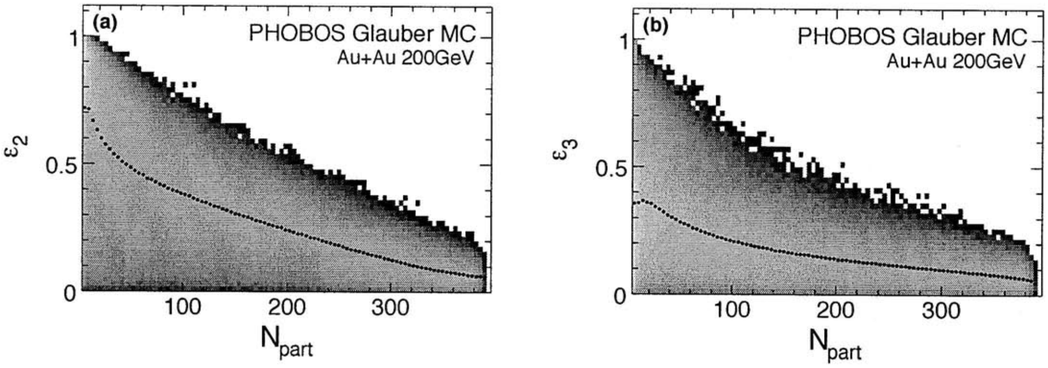

Figure 3.1: Distribution of (a) eccentricity, ε_2, and (b) triangularity, ε_3, as a function of number of participating nucleons, N_{part}, in simulated Au+Au collisions at $\sqrt{s_{\text{NN}}} = 200$ GeV.

of mass of the participating nucleons such that $\langle x \rangle = \langle y \rangle = 0$. The definition of eccentricity in this shifted coordinate system is equivalent to

$$\varepsilon_2 = \frac{\sqrt{\langle r^2 \cos(2\phi_{\text{part}}) \rangle^2 + \langle r^2 \sin(2\phi_{\text{part}}) \rangle^2}}{\langle r^2 \rangle}, \tag{3.1}$$

where r and ϕ_{part} are the polar coordinate positions of participating nucleons. The minor axis of the ellipse defined by this region is given as

$$\psi_2 = \frac{\text{atan2}\left(\langle r^2 \sin(2\phi_{\text{part}}) \rangle, \langle r^2 \cos(2\phi_{\text{part}}) \rangle\right) + \pi}{2}. \tag{3.2}$$

Since the pressure gradients are largest along ψ_2, the collective flow is expected to be strongest in this direction. The definition of v_2 has conceptually changed to refer to the second Fourier coefficient of particle distribution with respect to ψ_2 rather than the reaction plane

$$v_2 = \langle \cos(2(\phi - \psi_2)) \rangle. \tag{3.3}$$

This change has not impacted the experimental definition since the directions of the reaction plane angle or ψ_2 are not a priori known.

Drawing an analogy to eccentricity and elliptic flow, the initial and final triangular anisotropies can be quantified as participant triangularity, ε_3, and triangular flow, v_3, respectively:

$$\varepsilon_3 \equiv \frac{\sqrt{\langle r^2 \cos(3\phi_{\text{part}}) \rangle^2 + \langle r^2 \sin(3\phi_{\text{part}}) \rangle^2}}{\langle r^2 \rangle} \tag{3.4}$$

$$v_3 \equiv \langle \cos(3(\phi - \psi_3)) \rangle, \tag{3.5}$$

where ψ_3 is the minor axis of participant triangularity given by

$$\psi_3 = \frac{\text{atan2}\left(\langle r^2 \sin(3\phi_{\text{part}}) \rangle, \langle r^2 \cos(3\phi_{\text{part}}) \rangle\right) + \pi}{3}. \tag{3.6}$$

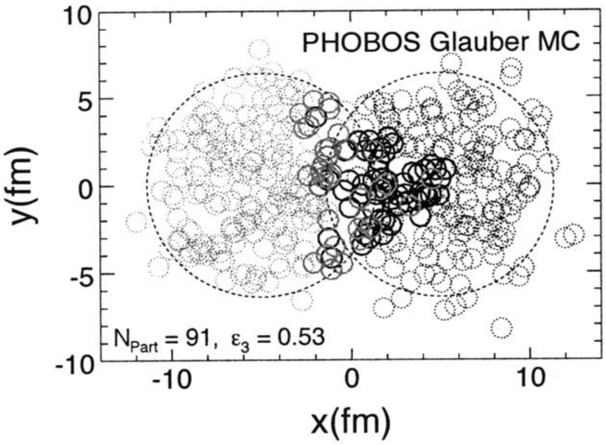

Figure 3.2: Distribution of nucleons on the transverse plane for a Au+Au collision event at $\sqrt{s_{\mathrm{NN}}} = 200$ GeV with ε_3=0.53 from Phobos Glauber Monte Carlo. The nucleons in the two nuclei are shown in gray and black. Wounded nucleons (participants) are indicated as solid circles, while spectators are dotted circles.

It is important to note that the minor axis of triangularity is found to be uncorrelated with the reaction plane angle and the minor axis of eccentricity in Glauber Monte Carlo calculations.

The distributions of eccentricity and triangularity calculated with the PHOBOS Glauber Monte Carlo implementation [66] for Au+Au events at $\sqrt{s_{\mathrm{NN}}} = 200$ GeV are shown in Fig. 3.1. The value of triangularity is observed to fluctuate event-by-event and have an average magnitude of the same order as eccentricity. Transverse distribution of nucleons for a sample Monte Carlo event with a high value of triangularity is shown in Fig. 3.2. A clear triangular anisotropy can be seen in the region defined by the participating nucleons.

3.2 Elliptic and Triangular Flow in the AMPT Model

The AMPT model is a hybrid model which consists of four main components: initial conditions, parton cascade, string fragmentation and A Relativistic Transport Model for hadrons. AMPT successfully describes main features of the dependence of elliptic flow on centrality and transverse momentum [70]. Ridge and broad away side features in two-particle correlations are also observed in the AMPT model [71, 72]. Furthermore, the dependence of quantitative observables such as away-side RMS width and away-side splitting parameter D on transverse momentum and reaction plane in AMPT reproduces the experimental results successfully, where similar methodology is applied to account for the contribution of elliptic flow to two-particle correlations to both the data and the model [73, 74].

The initial conditions of AMPT are obtained from Heavy Ion Jet Interaction

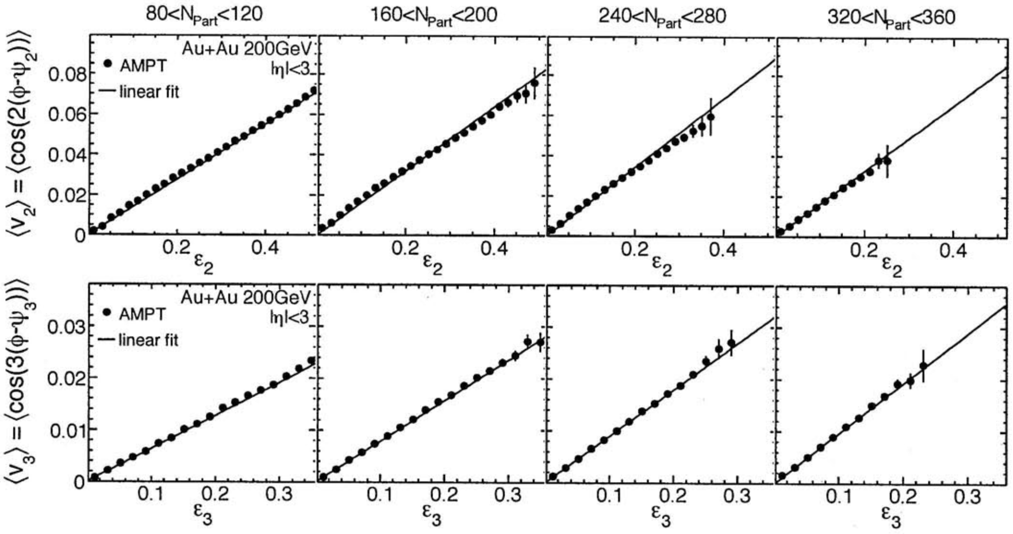

Figure 3.3: Top: average elliptic flow, $\langle v_2 \rangle$, as a function of eccentricity, ε_2; bottom: average triangular flow, $\langle v_3 \rangle$, as a function of triangularity, ε_3, in $\sqrt{s_{\mathrm{NN}}} = 200$ GeV Au+Au collisions from the AMPT model in bins of number of participating nucleons. Error bars indicate statistical errors. A linear fit to the data is shown.

Generator (HIJING) [75]. HIJING uses a Glauber Model implementation that is similar to the PHOBOS implementation to determine positions of participating nucleons. It is possible to calculate the values of ε_2, ψ_2, ε_3 and ψ_3 event-by-event from the positions of these nucleons. Next, the magnitudes of elliptic and triangular flow can be calculated with respect to ψ_2 and ψ_3 respectively as defined in Equations 3.3 and 3.5 from the position of final particles in the AMPT model events.

The average value of elliptic flow, v_2, and triangular flow, v_3, for particles in the pseudorapidity range $|\eta|<3$ in Au+Au collisions at $\sqrt{s_{\mathrm{NN}}} = 200$ GeV from AMPT are shown as a function of ε_2 and ε_3 in Fig. 3.3 for different ranges of number of participating nucleons. As previously expected, the magnitude of v_2 is found to be proportional to ε_2. A similar linear relation is also observed to be present between triangular flow and triangularity, demonstrating that the triangular anisotropy in initial collision geometry leads to a triangular anisotropy in particle production in the AMPT model.

The next question is whether the triangular flow in AMPT is strong enough to account for the observed ridge and broad away side features in two-particle azimuthal correlations. Consider the Fourier expansion of the distribution of azimuthal separation between particle pairs, $\Delta\phi$,

$$\frac{\mathrm{d}N^{\mathrm{pairs}}}{\mathrm{d}\Delta\phi} = \frac{N^{\mathrm{pairs}}}{2\pi}\left(1 + \sum_{n} 2\mathbf{V}_n \cos(n\Delta\phi)\right). \tag{3.7}$$

For a given pseudorapidity window, $\mathbf{V}_n$ can be calculated in AMPT by averaging $\cos(n\Delta\phi)$ over all particle pairs. Contributions from elliptic (triangular) flow is

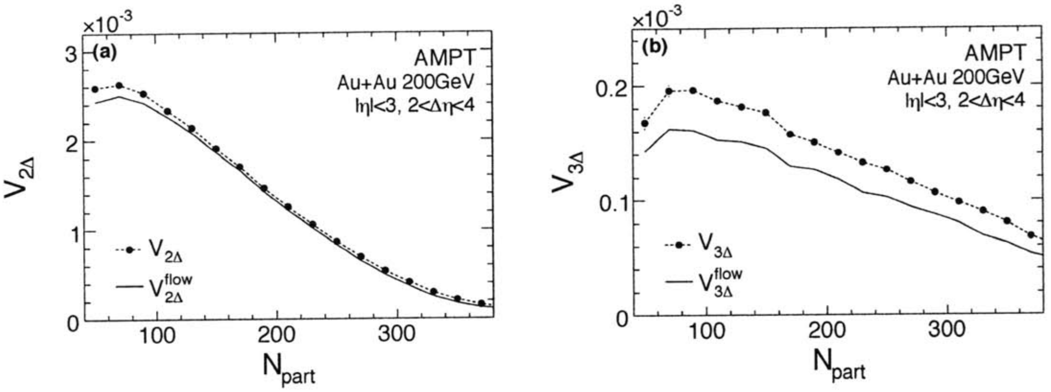

Figure 3.4: Dashed lines show (a) second Fourier coefficient, $\mathbf{V}_2$, and (b) third Fourier coefficient, $\mathbf{V}_3$, of azimuthal correlations as a function of number of participating nucleons, N_{part}, in Au+Au collisions at $\sqrt{s_{\text{NN}}} = 200$ GeV from the AMPT model. Solid lines show the contribution to these coefficients from flow calculated with respect to the minor axes of eccentricity and triangularity.

present in the second (third) Fourier coefficient of $\Delta\phi$ distribution since

$$\int \frac{1}{4\pi^2} \left\{1 + 2v_n \cos(n\phi)\right\} \times \left\{1 + 2v_n \cos(n(\phi + \Delta\phi))\right\} \mathrm{d}\phi$$
$$= \frac{1}{2\pi} \left\{1 + 2v_n^2 \cos(n\Delta\phi)\right\}. \quad (3.8)$$

This contribution can be calculated from average elliptic (triangular) flow values as

$$\mathbf{V}_n^{\text{flow}} = \frac{\langle \varepsilon_n^2 \rangle}{\langle \varepsilon_n \rangle^2} \times \frac{\int \frac{\mathrm{d}N}{\mathrm{d}\eta}(\eta_1) \frac{\mathrm{d}N}{\mathrm{d}\eta}(\eta_2) \left\langle v_n(\eta_1) \right\rangle \left\langle v_n(\eta_2) \right\rangle \mathrm{d}\eta_1 \mathrm{d}\eta_2}{\int \frac{\mathrm{d}N}{\mathrm{d}\eta}(\eta_1) \frac{\mathrm{d}N}{\mathrm{d}\eta}(\eta_2) \mathrm{d}\eta_1 \mathrm{d}\eta_2}, \quad (3.9)$$

where $n = 2$ ($n = 3$) and the integration is over the pseudorapidity range of particle pairs. The ratio $\langle \varepsilon_n^2 \rangle \,/\, \langle \varepsilon_n \rangle^2$ accounts for the difference between $\langle v_n(\eta_1) \times v_n(\eta_2) \rangle$ and $\langle v_n(\eta_1) \rangle \times \langle v_n(\eta_2) \rangle$ expected from initial geometry fluctuations.

The second and third Fourier components of two-particle azimuthal correlations for particle pairs in $\sqrt{s_{\text{NN}}} = 200$ GeV Au+Au collisions from AMPT within the pseudorapidity range $|\eta| < 3$ and $2 < \Delta\eta < 4$ are presented in Fig. 3.4 as a function of number of participating nucleons. Also shown in the same figure are the expected contributions to these components from elliptic and triangular flow, calculated with Eq. 3.9. More than 80% of the third Fourier coefficient of azimuthal correlations can be accounted for by triangular flow with respect to the minor axis of triangularity. The difference between $\mathbf{V}_3$ and $\mathbf{V}_3^{\text{flow}}$ may be due to two different effects: There might be contributions from correlations other than triangular flow to $\mathbf{V}_3$ or the angle with respect to which the global triangular anisotropy develops might not be given precisely by the minor axis of triangularity calculated from positions of participant

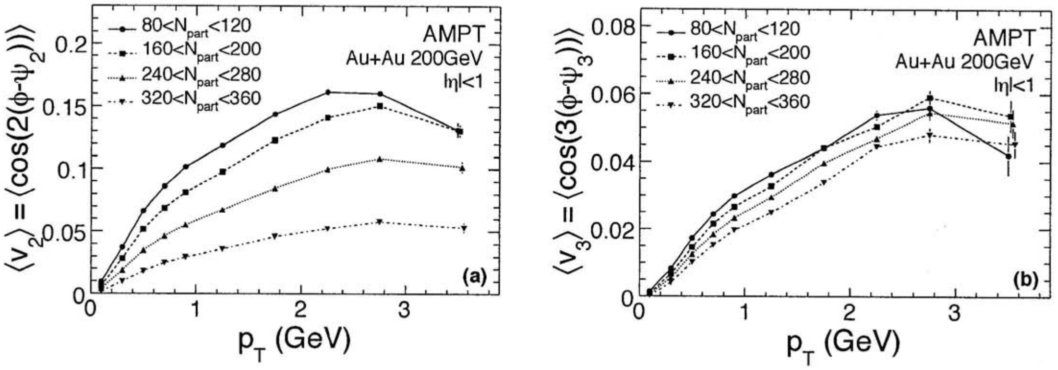

Figure 3.5: (a) Elliptic flow, v_2, and (b) triangular flow, v_3, as a function of transverse momentum, p_{T}, in bins of number of participating nucleons, N_{part}, for particles at mid-rapidity ($|\eta| < 1$) in Au+Au collisions at $\sqrt{s_{\mathrm{NN}}} = 200$ GeV from the AMPT model. Error bars indicate statistical errors.

nucleons, i.e. $v_3 = \langle(\cos(3(\phi - \psi_3))\rangle$ might be an underestimate for the magnitude of triangular flow. More detailed studies are needed to distinguish between these two effects.

The magnitudes of elliptic and triangular flow in the AMPT model can also be studied more differentially as a function of transverse momentum and number of participating nucleons. Fig. 3.5 shows the results as a function of transverse momentum for particles at mid-rapidity ($|\eta| < 1$) for different ranges of number of participating nucleons. The dependence of triangular flow on transverse momentum is observed to show similar gross features as elliptic flow. A more detailed comparison can be made by taking the ratio of triangular to elliptic flow, shown in Fig. 3.6 as a function of number of participating nucleons for different ranges of transverse momentum. The relative strength of triangular flow is observed to increase with centrality and transverse momentum. This observation is qualitatively consistent with the trends in experimentally measured ridge yield.

3.3 Third Fourier Coefficient of Azimuthal Correlations in Heavy Ion Collisions

Triangular flow has not been directly studied in heavy ion collisions. However, the magnitude of triangular flow can be extracted from two-particle correlation measurements. Different correlation measures such as $R(\Delta\eta, \Delta\phi)$ [68], $N\hat{r}(\Delta\eta, \Delta\phi)$ [77] and $1/N_{\mathrm{trig}}\mathrm{d}N/\mathrm{d}\Delta\phi(\Delta\eta, \Delta\phi)$ [36] have been used to study different sources of particle correlations. The azimuthal projection of all of these correlation functions have the form

$$C(\Delta\phi) = A\frac{\mathrm{d}N^{\mathrm{pairs}}}{\mathrm{d}\Delta\phi} + B, \tag{3.10}$$

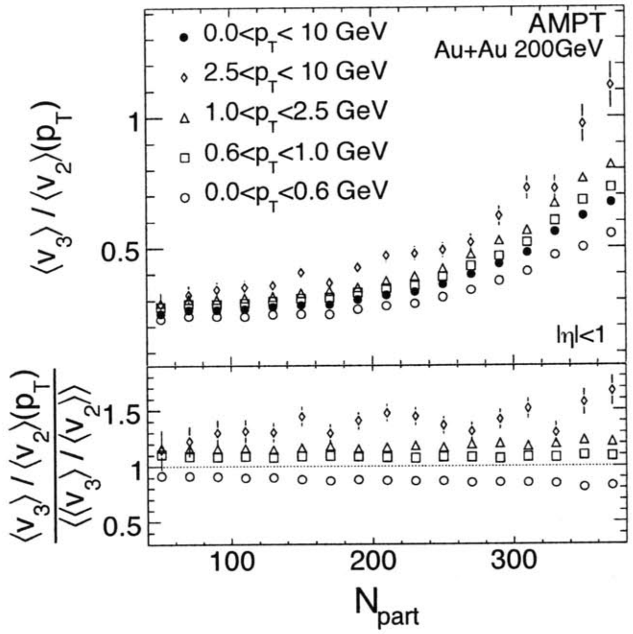

Figure 3.6: Top: the ratio of triangular flow to elliptic flow, $\langle v_3 \rangle / \langle v_2 \rangle$, as a function of number of participating nucleons, N_{part}, for particles at mid-rapidity ($|\eta| < 1$) in Au+Au collisions at $\sqrt{s_{\text{NN}}} = 200$ GeV from AMPT. Open points show different transverse momentum bins and the filled points show the average over all transverse momentum bins. Bottom: the ratio of different p_{T} bins to the average value. Error bars indicate statistical errors.

where the scale factor A and offset B depend on the definition of the correlation function as well as the pseudorapidity range of the projection [36].

Contributions from correlations other than flow, such as jets and resonances, are most prominent in short pseudorapidity separations ($\Delta\eta$). To reduce contribution from such non-flow correlations and obtain more precise values of elliptic and triangular, the correlation functions can be projected at pseudorapidity separations of $1.2 < \Delta\eta < 1.9$ for STAR data and $2 < \Delta\eta < 4$ for PHOBOS data. Examples of azimuthal correlation distributions are shown in Fig. 3.7 for inclusive correlations from PHOBOS and STAR and high p_T triggered correlations from PHOBOS for mid-central Au+Au collisions [36, 68, 76]. The first three Fourier components of the correlations and the residual after these components are taken out are also shown in the same figure. The data is found to be well described by the three Fourier components.

To study different correlation measures on equal footing, the ratio of their third and second Fourier coefficients can be calculated by

$$\frac{\mathbf{V}_3}{\mathbf{V}_2} = \frac{\int C(\Delta\phi)\cos(3\Delta\phi)\mathrm{d}\Delta\phi}{\int C(\Delta\phi)\cos(2\Delta\phi)\mathrm{d}\Delta\phi}. \tag{3.11}$$

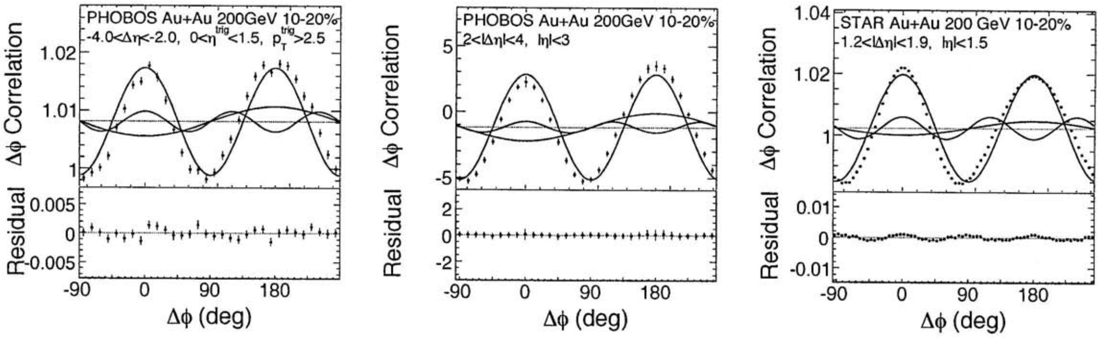

Figure 3.7: Top: azimuthal correlation functions for mid-central (10-20%) Au+Au collisions at $\sqrt{s_{\mathrm{NN}}} = 200$ GeV obtained from projections of two-dimensional $\Delta\eta, \Delta\phi$ correlation measurements by PHOBOS [36, 68] and STAR [76]. The transverse momentum and pseudorapidity ranges are indicated on the figures. Errors bars are combined systematic and statistical errors. The first three Fourier components are shown in solid lines. Bottom: the residual correlation functions after the first three Fourier components are subtracted.

The factors A and B in Eq. 3.10 cancel out in this ratio. Results for PHOBOS [36, 68] and STAR [76] measurements are plotted as a function of number of participating nucleons in Figures 3.8(a) and (b), respectively. It is observed that $\mathbf{V}_3/\mathbf{V}_2$ increases with centrality and with the transverse momentum of the trigger particle. Comparing inclusive correlations from STAR and PHOBOS, it is also observed that the value of $\mathbf{V}_3/\mathbf{V}_2$ is higher for STAR measurements. The ratio $\mathbf{V}_3/\mathbf{V}_2$ calculated for the same PHOBOS measurement in the range $1.2 < |\Delta\eta| < 2$ is found to be consistent with the values for $2 < |\Delta\eta| < 4$ within the systematic uncertainties. The difference between the STAR and PHOBOS measurements is, therefore, likely caused by the differences in pseudorapidity and transverse momentum acceptance of the two experiments.

Also shown in Fig. 3.8 are the results for $\mathbf{V}_3/\mathbf{V}_2$ for the AMPT model with similar η, $\Delta\eta$ and p_{T} selections to the available experimental data. The calculations from the model show a qualitative agreement with the data in term of the dependence of $\mathbf{V}_3/\mathbf{V}_2$ on the pseudorapidity region, trigger particle momentum and centrality. Since the $\mathbf{V}_3$ signal in AMPT is known to be mainly due to triangular flow, this agreement suggests that triangular flow is the source of the ridge and broad away side features observed in the data.

A closer look at the properties of the ridge and broad away side is possible via studies of three-particle correlations. Triangular flow predicts a very distinct signature in three-particle correlation measurements. Two recent publications by the STAR experiment present results on correlations in $\Delta\phi_1$-$\Delta\phi_2$ space for $|\eta| < 1$ [41] and in $\Delta\eta_1$-$\Delta\eta_2$ space for $|\Delta\phi| < 0.7$ [78]. In $\Delta\phi_1$-$\Delta\phi_2$ space, off diagonal away side correlations have been observed (e.g. first associated particle at $\Delta\phi_1 \approx 120°$ and second associated particle at $\Delta\phi_2 \approx -120°$) consistent with expectations from triangular

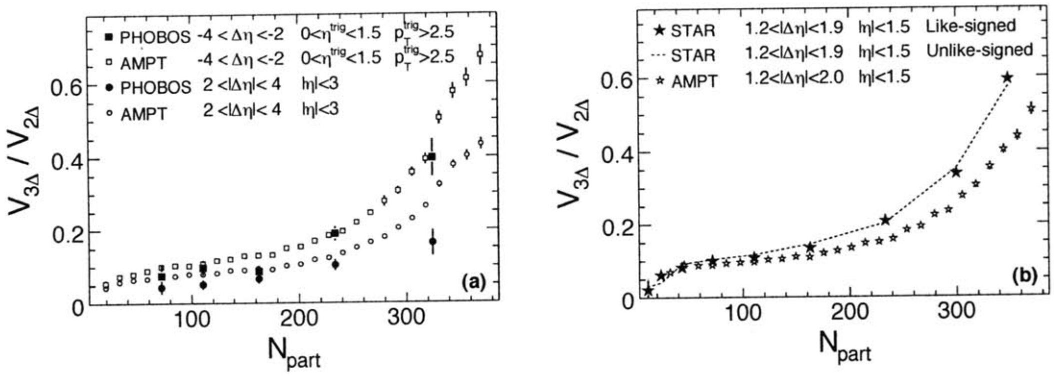

Figure 3.8: The ratio of the third to second Fourier coefficients of azimuthal correlations, $\mathbf{V}_3/\mathbf{V}_2$, as a function of number of participating nucleons, N_{part}, for Au+Au collisions at $\sqrt{s_{\text{NN}}} = 200$ GeV. Filled points show (a) PHOBOS [36, 68] and (b) STAR [76] data. Pseudorapidity and trigger particle transitive momentum ranges for different measurements are indicated on the figures. Open points show results from the AMPT model for similar selection of pseudorapidity and transverse momentum to the available data. Error bars indicate statistical errors for AMPT and combined statistical and systematic errors for the experimental data.

flow. In $\Delta\eta_1$-$\Delta\eta_2$ space, no correlation structure between the two associated ridge particles was detected, also consistent with triangular flow.

These findings suggest that elliptic and triangular flow, along with a first Fourier component due to momentum conservation and directed flow successfully describes azimuthal correlations at large pseudorapidity separations and that the contribution from local correlations such as jets and resonances is small for correlations at $\Delta\eta > 1.2$. The description of the ridge and broad away side features in two-particle correlations in terms of triangular flow relies crucially on the existence of initial geometry fluctuations. The measurement of elliptic flow fluctuations presented in the following chapters presents an important test of this description.

4 The PHOBOS Experiment

The PHOBOS experiment at the Relativistic Heavy Ion Collider (RHIC) was designed to study the global event characteristics of heavy ion collisions. The large η–ϕ coverage of the PHOBOS detector is well suited for elliptic flow and particle correlation studies. The data presented in this thesis for Au+Au collisions at $\sqrt{s_{\rm NN}} = 200$ GeV were collected during RHIC Run 4 (2004). The experimental setup of the PHOBOS detector and the triggering, reconstruction, characterization and selection of collision events are summarized in this chapter. The current list of members of the PHOBOS Collaboration can be found in Appendix B.

A diagram of the PHOBOS detector setup is shown in Fig. 4.1. Collision triggers use the time and energy information in the fast detectors to determine if a particular event is useful and should be recorded. The two main components of the PHOBOS detector are an array of multiplicity detectors covering almost the entire solid angle of produced particles, and a two-arm magnetic spectrometer to study the detailed properties of a small fraction of these particles ($\sim 2\%$). Once the signal in the various detectors has been read out and processed, the vertex position and fractional cross-section are determined. The information from the complete event reconstruction allows further selection on the utility of recorded collisions for different physics analyses.

4.1 The Collision Trigger

RHIC provides a "crossing-clock" to the four experiments which reports the crossing time of beam bunches at the experiment collision points. In principle, the crossing-clock can be used to determine when the signal in the detectors should be recorded. However, a Au+Au collision occurs only about once every 10000 times the bunches cross at the PHOBOS collision point [79]. If the detector was triggered using the crossing-clock, most of the data written to tape would have to be later discarded. Furthermore, due to the slow readout of the detector, every crossing-clock event could not be recorded, leading to a lower number of real collision events stored. Therefore, the trigger system has been vital to the recording of billions of collision events by PHOBOS.

4.1.1 Trigger Detectors

The primary trigger detectors used in nucleus-nucleus collisions are the two scintillator Paddle counters. The Zero-Degree Calorimeters (ZDCs) have been utilized

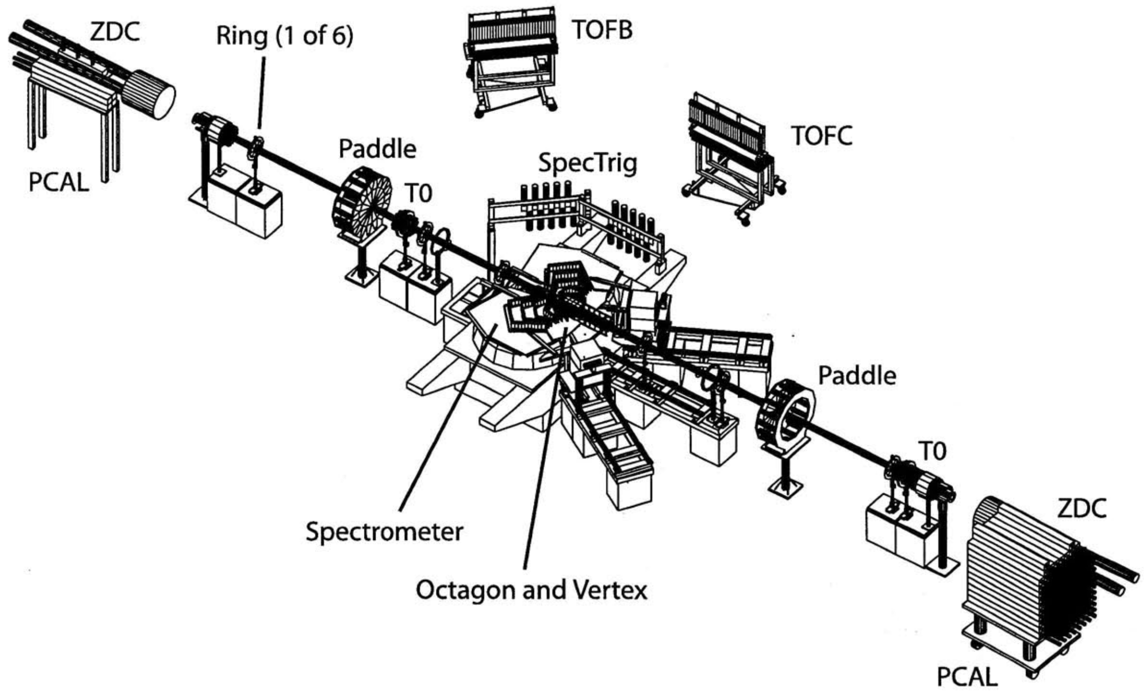

Figure 4.1: The complete PHOBOS detector setup in 2003. The calorimeters were roughly three times further from the interaction point than shown.

to reject beam-gas events for very high background runs. The fast Time-Zero Counters (T0s) provide online collision vertex information allowing a more restricted triggering and higher data quality.

Paddle Counters

The Paddle counters [80] are two arrays of 16 wedge-shaped scintillators located at ±3.21 m from the nominal interaction point. A diagram of one of the arrays is shown in Fig. 4.2(a) [80]. The Paddle counters cover the pseudorapidity region $3 < |\eta| < 4.5$ and have an active area of 99%. When a particle passes through one of the paddles, it gives off scintillating light which registers as an energy signal in the phototube coupled to the scintillator. An energy signal above a certain threshold is counted as a "hit" in that module. The plastic scintillators have a large dynamic range (from one Minimum Ionizing Particle (MIP) up to 50 per collision) and a timing resolution of about 1 ns. The high efficiency and fast response of the Paddle counters make the detector ideal for minimum bias triggering. Due to the large dynamic range, the Paddle counters are also used in the collision centrality determination.

Time-Zero Counters

The Time-Zero Counters (T0s) are two arrays of ten Bicron BC800 Cerenkov radiators positioned at ±5.3 m from the nominal interaction point. They are coupled to fast

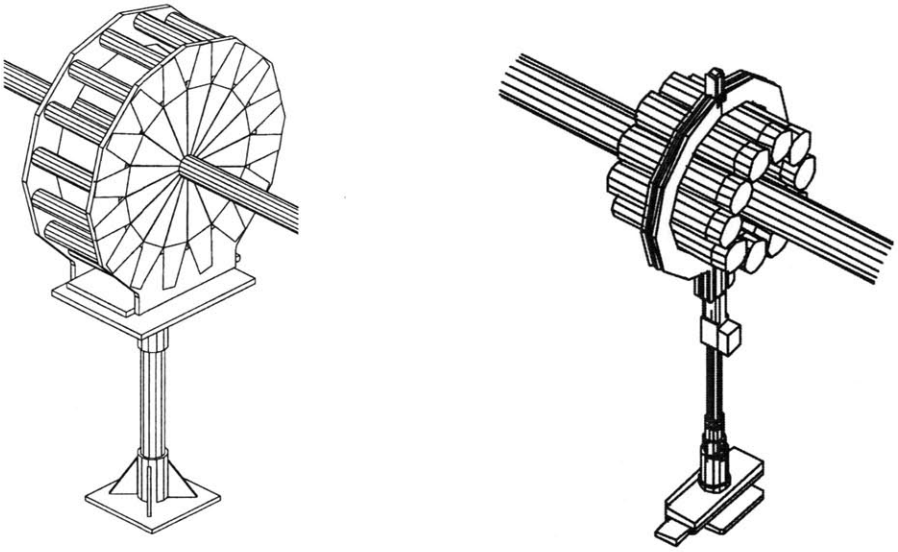

(a) Paddle Counter (b) Time-Zero Counter (T0)

Figure 4.2: Schematic diagrams of the trigger counters: (a) Paddle counter [80] (b) Time-Zero Counter (T0).

Hamamatsu R2083 Photomultiplier Tubes (PMTs). A diagram of one of the T0s is shown in Fig. 4.2(b). The Cerenkov radiators are 25 mm thick and 50 mm in diameter. The T0s have an intrinsic time resolution of 110 ps. Because of their fast response time, the T0s provide real-time vertex information for use in triggering. However, their smaller geometrical acceptance results in some loss in efficiency for very low multiplicity events.

Zero-Degree Calorimeters

Each of the four RHIC experiments contain an identical set of Zero-Degree Calorimeters (ZDCs) that serve as a common device to measure luminosity and centrality using free neutrons created from fragmentation of the colliding nuclei. The ZDCs are located at $z = \pm 18.5$ m just after the DX magnet where the RHIC beam branches back into two beam pipes, as shown in Fig. 4.3. The region immediately behind the DX magnet is especially well-suited for the measurement of free neutrons, since all charged particles are swept away by the magnet.

The ZDCs are hadron shower, sampling calorimeters that consist of three identical modules. The calorimeters are designed to minimize energy loss from the transverse leakage of the shower utilizing the limited available space in the "zero-degree" region. They are made of alternating layers of tungsten and optical fibers to detect Cherenkov light. All fibers from one module are bundled and fed into a single photomultiplier tube.

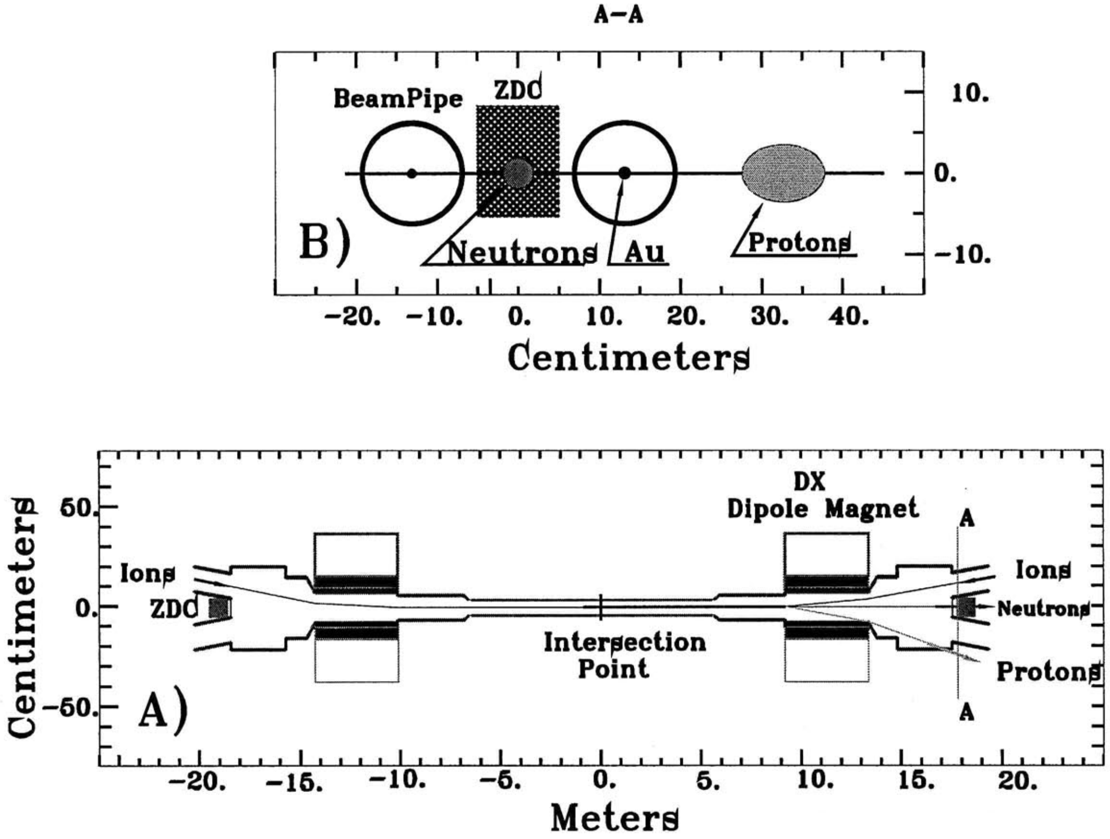

Figure 4.3: "Beam's eye" (top) and plan (bottom) views of the ZDC location and the paths taken by gold beams and proton and neutron fragments [81].

4.1.2 Trigger Setup

The Paddle counters act as the primary event trigger. The Minimum-Bias triggers (*MinBias*) are designed to capture a large fraction of the total cross-section with minimal losses in efficiency. For the Au+Au collisions at $\sqrt{s_{\rm NN}} = 200$ GeV the *AAMinBias* setup required at least two hit slats in each Paddle detector. The Minimum-Bias triggered data is used for centrality determination, multiplicity analyses and data quality controls.

A higher quality data is selected by employing the less efficient Vertex trigger (*AAVertex*). The time difference between the signals from the two T0s is used to calculate the collision vertex with a resolution of roughly 3 cm in the beam direction. The nominal vertex range for PHOBOS detector is $-10 < z_{\rm vtx} < 10$ cm. For the 2004 run, a wider vertex window of $-40 < z_{\rm vtx} < 20$ cm was chosen since the very negative vertex positions can be useful to certain analyses (e.g. reconstruction of the ϕ meson via the two kaon decay channel).

The high luminosities achieved during the Au+Au run in 2004 resulted in a high rate of lost beam particles hitting the beam pipe and forming a cloud of electrons within the beam pipe [82]. For very high background runs, the *AAMinBias* and

AAVertex triggers allow a large amount of background in from double-beam-gas events. In such runs, a double ZDC coincidence was also required in the *AAzdcMinBias* and *AAzdcVertex* trigger setups. The ZDC requirement is found to remove a large amount of background effects with little effect on the trigger efficiency.

More detail on the different trigger setups can be found in [79].

4.2 Silicon Detector Design and Hit Reconstruction

The PHOBOS multiplicity array uses single layers of silicon to measure the number and angular distribution of charged particles. Particles produced at $|\eta| < 3.2$ are detected in the Octagon, an octagonal barrel of sensors that surrounds the beam-pipe. Particles emitted at more forward angles are detected by six Ring counters, mounted perpendicular to the beam-pipe, extending the pseudorapidity coverage to $|\eta| < 5.4$. Above and below the interaction region, two layers of the finely segmented Vertex detector provide high precision vertex information. The PHOBOS two-arm Spectrometer, located on either side of the beam-pipe is used in reconstructing the momentum of a small fraction of the particles produced in the collisions, as well as aiding in vertex determination.

Octagon Detector

The Octagon detector, shown in Fig. 4.4(a) [83], is composed of single layer silicon sensors centered around the nominal collision point and spans $|z| < 55$ cm. It is made up of eight ladders of silicon that run parallel to the beam and surround the beam pipe in a barrel-shaped configuration. The diameter of the Octagon in the plane transverse to the beam is approximately 90 mm between ladder faces. Each ladder contains up to 13 silicon sensors that run parallel to the beam pipe in the longitudinal direction. Near the midrapidity region, sensors have been removed from the ladders facing the Spectrometer and the Vertex detectors to allow full acceptance of particles into these detectors with no additional scattering from the Octagon sensors. Fig. 4.5 shows the positions of the Spectrometer and Vertex detectors with respect to the Octagon. Each Octagon "hole" spans three Octagon sensor layers. Other than these holes, the Octagon has nearly full azimuthal coverage and provides a pseudorapidity coverage of $|\eta| < 3.2$. Each 84 mm × 36 mm sensor is divided into four rows of 30 pads each. The Octagon is mounted to a lightweight aluminum frame that provides support and also transports chilled water through the system to cool the electronic readout chips that are attached to each sensor.

Ring Detectors

There are six Ring detectors located at $z = \pm1.13$, ±2.35, and ±5.05 m from the nominal collision point and extend the pseudorapidity coverage of the multiplicity array to $|\eta| < 5.4$. A single Ring module is shown in Fig. 4.4(b) [83]. Each Ring is made up of eight trapezoidal silicon sensors that surround the beam pipe. Each

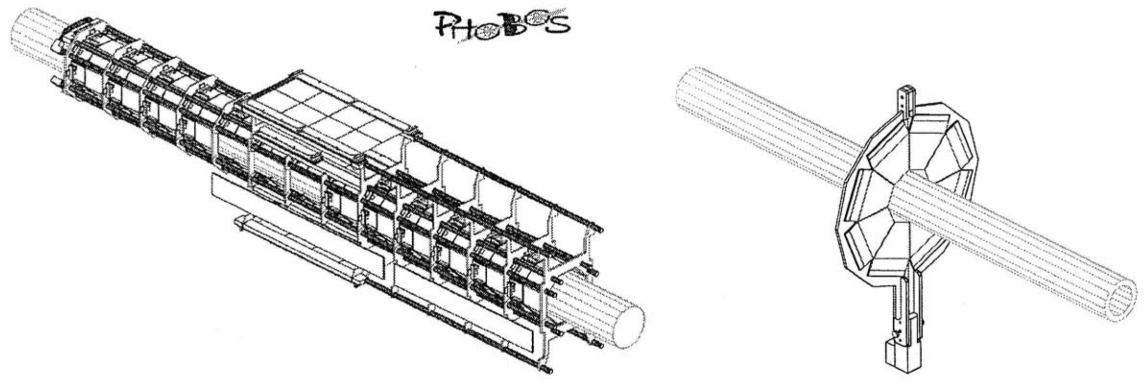

(a) Octagon and Vertex Detectors (b) Ring Detector

Figure 4.4: The PHOBOS multiplicity detectors [83].

sensor is made up of 64 pads arranged in 8 rows in the azimuthal direction by 8 columns in the radial direction from the beam pipe. The pad sizes are chosen so that each pad covers the same angular coverage of $\Delta\eta \approx 0.1$ and $\Delta\phi \approx \pi/32$. The pad sizes closest to the beam pipe are 3.8 mm × 5.1 mm while those furthest from the beam pipe are 10.2 mm × 10.2 mm.

Vertex Detector

The Vertex detector consists of four planes of silicon, two above and two below the collision point. It was designed to measure the location of the primary collision vertex within the range $|z_{\text{vtx}}| < 10$ cm to an accuracy of 0.2 mm in high multiplicity Au+Au events.

The layers closer to the collision point (Inner Vertex) are located at $y = \pm 56$ mm and are each made up of four sensors laid out in a line along the beam direction. The pads on each Inner Vertex sensor are arranged in four columns of 128 pads. In the azimuthal direction, the 12 mm long pads are similar in dimension to the Octagon. Along the beam direction, the pads have a finer segmentation of 0.473 mm, to achieve the desired vertexing precision.

The Outer Vertex layers are located at $y = \pm 118$ mm from the collision axis. Each plane contains eight sensors, four along the longitudinal direction and two in the azimuthal direction. Each sensor is divided into 256 pads, with two rows of pads in the azimuthal direction and 128 columns in the longitudinal direction. The outer Vertex pad sizes are 0.474 mm × 24.070 mm.

In addition to providing vertex information, the Vertex detectors, with a solid angle corresponding approximately to the removed Octagon sensors, complement the Octagon detector in different physics analyses. For collisions at the nominal vertex position, the Inner Vertex covers $|\eta| < 1.54$ and the Outer Vertex covers $|\eta| < 0.92$. Both layers have an azimuthal coverage of almost $\Delta\phi = \pi/4$. The upper 4×2 array of Outer Vertex sensors can be seen in Fig. 4.4(a) [83].

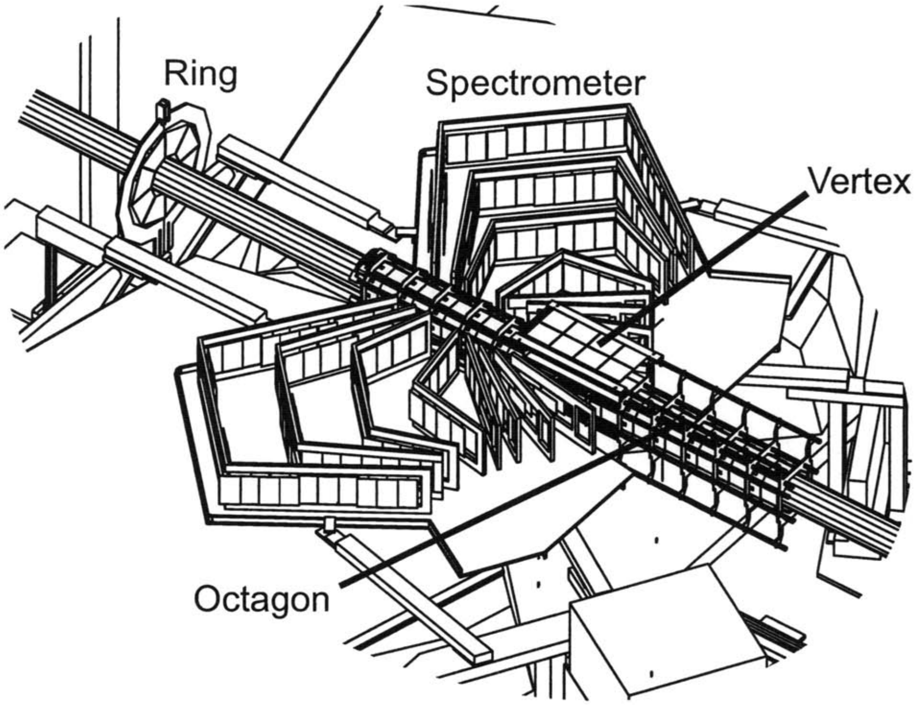

Figure 4.5: The PHOBOS silicon detectors in the proximity of the interaction point. The top yoke of the PHOBOS magnet is not shown [17].

The Spectrometer

The PHOBOS Spectrometer, shown in Fig. 4.5 [17], consists of two arms in the $x-z$ plane located on opposite sides of the beam-line. Each arm consists of 137 silicon sensors of various sizes arranged into sixteen layers. Each Spectrometer arm sits in a dipole magnetic field with a maximum field strength of 2 T. The first six planes of each Spectrometer arm sit in a region that is outside the strong magnetic field. The main purpose of this region is to provide starting tracks for curved tracking algorithms in the high magnetic field region. The straight-line tracks reconstructed in this region are also used in the determination of the collision vertex.

The Spectrometer was designed to study the detailed properties of a small fraction of the particles produced in the collision ($\sim 2\%$). The particles bend as they traverse the magnetic field, which allows for momentum determination using curved tracking algorithms. The Spectrometer has a charged hadron transverse momentum reach of up to $p_{\mathrm{T}} \approx 6$ GeV/c. Particle identification is done by measuring the $\mathrm{d}E/\mathrm{d}x$ energy loss of charged particles as they pass through the planes. Pions and kaons can be identified up to 700 MeV/c, while the ability to distinguish protons from pions/kaons has been achieved for momenta up to 1.2 GeV/c.

In total, the Spectrometer consists of 135,168 separate channels. The small horizontal width of the silicon pads (0.427-1.000 mm) in all layers is crucial for a good resolution in the bending direction of tracks. The vertical dimension of the pads ranges between 1.0-19.0 mm, increasing at large distances from the interaction point to reduce the cost of the sensors at the expense of some decreased azimuthal resolution.

Silicon Sensor Design

Although the silicon pads of the various subdetectors vary in shape and size, they share a common basic design [84]. Figure 4.6 shows the schematic diagram of a typical silicon pad. Each pad is nominally 300 μm thick and composed of a fully depleted, reversed biased p-n junction. When a charged particle passes through the pad, ionization leads to the creation of electron-hole pairs which register as a measurable current in the readout chips which are located at the edge of each sensor.

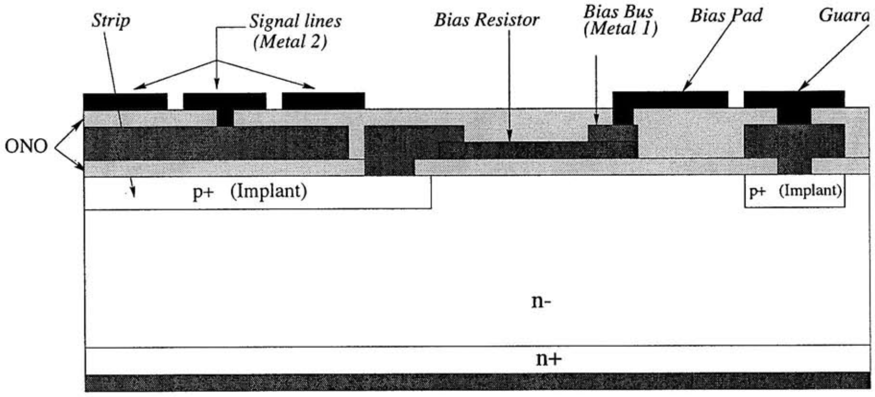

Figure 4.6: Cross-section of a silicon sensor [84].

Each sensor is a single sided, AC coupled detector that uses double-metal layers to route signals from the pads to the readout chips. The p^+ implants in the sensor act as rectangular pads and provide two dimensional position information of charged particles. The implants are capacitively coupled to the aluminum pickup pads via a 0.2 μm thick layer of silicon Oxide-Nitrous-Oxide (ONO) dielectric material. The induced current from each pad is read-out by its own metal line that leads to the front-end electronics at the edge of the sensor. The network of signal lines is separated from the aluminum pickups by a 1.2 μm thick ONO layer. The read-out of the silicon channels is handled by commercially available chips, which integrate the collected signals from the silicon pads.

Signal Processing

The pre-amplified signals from the silicon detector read-out chips are digitized by 12-bit Analog-to-Digital Converters (ADCs). The digitized signal is corrected and calibrated in three steps. First, the quasi-static offset, known as the "pedestal", is periodically determined for each channel and subtracted. Second, the common mode noise, which is an offset that varies with each readout and is shared among all of the elements in the same detector region is calculated and taken out. Finally, the differing degree of pre-amplification for each channel is determined from the distribution of the ADC signal and the calibration factor between the ADC values and the deposited energy is calculated.

The angular coordinates (η, ϕ) of charged particles are determined using the location of the energy deposited in the silicon detectors. After merging of signals in neighboring pads, in cases where a particle travels through more than a single pad, the deposited energy is corrected for the angle of incidence, assuming that the charged particle originated from the primary vertex. Noise and background hits are rejected by placing a lower threshold on the corrected deposited energy. Depending on η, merged hits with less than 50-60% of the energy loss expected for a minimum ionizing particle are rejected. Details of silicon signal processing and hit reconstruction can be found in [85].

4.3 Vertex Reconstruction

A reliable determination of the collision point is crucial for all physics analyses. The angular coordinates of particles are determined by relating the position of the signals registered in the detector to the collision vertex. As mentioned before, the timing signals from the paddles and T0 detectors provide the z coordinate of the vertex with an accuracy of a few centimeters. A rough estimate of the x and y coordinates of the collision vertex, referred to as the "beam orbit", is provided by RHIC.

A much more precise measurement of the three vertex coordinates is achieved with different algorithms utilizing the different silicon detectors. In Au+Au events, the vertex is determined by the *RMSSelVertex* algorithm, which itself is combination of vertexing algorithms using various detectors. The *ZVertex* algorithm uses the clusters of hits on the Vertex detectors to determine the y and z coordinates of the collision vertex. Straight lines joining combinations of hits in the Inner and Outer layers are projected back onto the $x = 0$ plane. The peaks in the y and z distributions of these line segments correspond to the vertex position. *SpecMainVertex* and *SpecVertex SpecPN* algorithms use the hits in the first four and six layers of the Spectrometer to construct straight tracks using road-following technique. The distance of closest approach between pairs of tracks is used to determine the vertex position in three-dimensions. *SpecVertex SpecPN* algorithm provides the most precise determination of the x coordinate. The *RMSSelVertex* algorithm combines the information from the above three algorithms to determine if a valid vertex position can be reconstructed and achieves the best resolution in all three coordinates. A more detailed description of the different vertex-finding procedures can be found in [86].

4.4 Offline Event Selection

The information from the complete event reconstruction allows further selection on the utility of recorded collisions for different physics analyses offline. The event quality is ensured by the following selections [79]:

- The difference between the positive and negative Paddle times (PdlTDiff) is required to be less than 5.0 ns. This selection elects collisions from the center of the detector (±75 cm), rejecting beam-gas events outside the Paddle region.
- A valid time signal from both ZDCs is required to reject beam-gas events which pass the cut on PdlTDiff.
- "Good L1 timing" requirement is imposed, which ensures that the fast clearing of the trigger signals, when a prior event is rejected by the trigger logic, is fully completed before the current event is read out.
- Events that are triggered less than 5 μs after another event are flagged as "pre-pileup" to avoid recording signals remaining in the slow silicon sub-detectors from the previous collision.
- Similarly, events that are triggered less than 0.5 μs before another event are flagged as "post-pileup" to avoid recording signal from the following event before the read-out of the current collision is completed.
- "Heartbeat" events which are periodic read-outs of the detector by the Data Acquisition (DAQ) are removed.

Additionally, most physics analyses require the existence of a valid *RMSSelVertex* within the range ($-10 < z_{\text{vtx}} < 10$ cm). This event selection is 100% efficient for the 55% most central events. Physics analyses are only performed on the centrality bins where *RMSSelVertex* is 100% efficient since the selection for more peripheral events will have a bias towards collisions where *RMSSelVertex* can be reconstructed. The same vertex and centrality selections are applied in the analysis of Monte Carlo simulated events. However, the Paddle timing and pile-up cuts are not required since there are no beam-gas or pile-up events in the Monte Carlo.

4.5 Centrality Determination

It is essential to classify events based on the initial geometry of the collision to study the underlying physics of any measurement. Since the impact parameter cannot be directly measured, a centrality classification procedure is employed based on Monte Carlo simulations of heavy ion collisions and the PHOBOS detector response. First, the "trigger efficiency", i.e. the fraction of the total cross-section to which the trigger is sensitive, is estimated by comparing measured distributions in data and GEANT simulations of the detector response based on the HIJING event generator. Next,

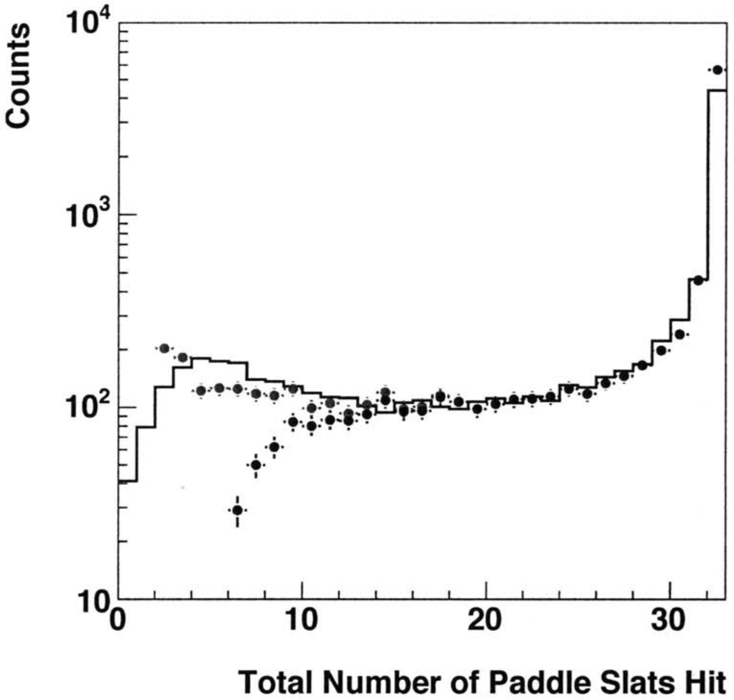

Figure 4.7: The distribution of the number of hit Paddles for HIJING model (black line) and Au+Au data for the $n > 0$ (red points) and $n > 2$ (blue points) MinBias trigger requirements.

using the known efficiency and a multiplicity variable with a monotonic dependence on centrality, the data is divided into bins of fractional cross-section. Finally, the bins in fractional cross-section are related to the variables of the collision geometry such as the impact parameter, b, or average numbers of participating nucleons, N_{part}. The details of the centrality determination procedure are described in [79].

To estimate the missing cross-section, the number of hit Paddle slats (between 0 and 32) is compared between data and HIJING as seen in Fig. 4.7. The different distributions are normalized in the region between 15 and 22 hit Paddles, where they show an approximate agreement. The efficiency is then calculated as the ratio of events seen in data by the sum of data events with sixteen or more hit Paddles and Monte Carlo events with fifteen or fewer hit Paddles.

$$\frac{\text{Data}(0,32)}{\text{MC}(0,15)+\text{Data}(16,32)} \tag{4.1}$$

This method of determining the efficiency ensures that any discrepancy in the most central collisions, which might be sensitive to the particular parameters of HIJING are not included. The final efficiencies for Au+Au collisions at $\sqrt{s_{\text{NN}}} = 200$ GeV are found to be 97% ($n > 0$) and 88% ($n > 2$), where n is the number of hit Paddles required for the trigger.

Once the efficiencies are determined, cuts on experimental measures which divide data events into bins of fractional cross-section are defined. The experimental mea-

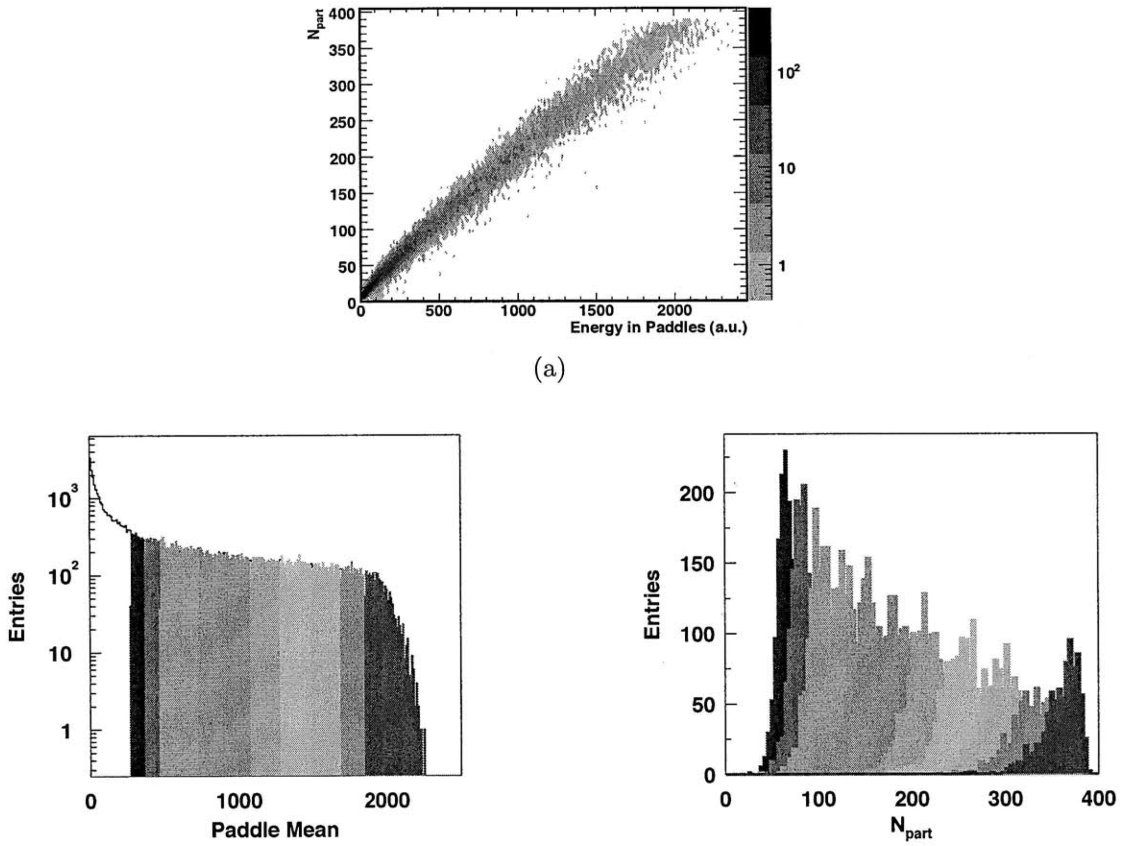

(a)

(b)

(c)

Figure 4.8: Results from simulations of HIJING model events with the PHOBOS detector relating fractional cross section, number of participating nucleons, N_{part}, and the truncated mean signal in the Paddle detectors, PdlMean. (a) N_{part} as a function of PdlMean. (b) The positions of the fractional cross-section cuts on the PdlMean distribution. (c) Distribution of N_{part} in Monte Carlo for the same bins shown in (b).

sure is required to have small statistical fluctuations and a monotonic dependence on centrality. For the Au+Au system at $\sqrt{s_{\text{NN}}} = 200$ GeV, cuts on the the truncated mean of the energy in the Paddles, referred to as Paddle Mean (PdlMean), are used to define bins of fractional cross-section.

Figure 4.8(a) shows the dependence of the number of participating nucleons (N_{part}) in HIJING model events on the energy in the Paddles. The PdlMean is observed to show the two required features for centrality determination. Using the previously calculated efficiency, cuts are made on the PdlMean distribution corresponding to bins of cross-section. For example, the most central bin shown in Fig. 4.8(b) corresponds to the 3% most central collisions.

Since the shapes of the Paddle signal distributions are well-matched between data and HIJING simulations, (see Fig. 4.7), the N_{part} distribution for each cross-section bin can be calculated directly from the corresponding cross-section bin in HIJING events. Figure 4.8(c) shows the distribution of number of participating nucleons for different cross section bins. The N_{part} values obtained from HIJING are related to number of binary collisions and eccentricity using the PHOBOS Glauber Monte Carlo described in Sect. 2.2. The mean and standard deviation values of the N_{part} and N_{coll} distributions for different cross section bins are tabulated in Table 4.1.

Fraction	N_{part}	N_{coll}
0% to 3%	357 ± 19.5	1001 ± 98.2
3% to 6%	330 ± 24.6	887 ± 111.5
6% to 10%	295 ± 25.2	750 ± 104.3
10% to 15%	253 ± 23.9	602 ± 90.9
15% to 20%	213 ± 21.5	470 ± 74.8
20% to 25%	178 ± 19.1	364 ± 63.1
25% to 30%	147 ± 17.2	277 ± 52.5
30% to 35%	122 ± 15.0	211 ± 42.5
35% to 40%	99 ± 13.2	156 ± 33.7
40% to 45%	80 ± 11.5	116 ± 26.4

Table 4.1: Mean and standard deviation of N_{part} and N_{coll} values for the fractional cross section bins used in Au+Au collisions at $\sqrt{s_{\text{NN}}}$ = 200 GeV for PHOBOS data analyses.

5 Technique of Elliptic Flow Fluctuations Measurement

An event-by-event measurement of the anisotropy in heavy ion collisions yields fluctuations from three sources: statistical fluctuations due to the finite number of particles observed, elliptic flow fluctuations and other many-particle correlations, referred to as non-flow correlations. The analysis method developed to account for statistical fluctuations and non-flow contributions and measure elliptic flow fluctuations is presented in this chapter. The methodology is introduced in the the context of a "perfect" PHOBOS-like detector, where the direction of all charged particles from the collision are measured and no secondary particles are produced due to interactions with the detector. Various corrections to reconstruct the observables in the real detector environment is provided in the following chapters.

The measurement of elliptic flow fluctuations in achieved in three steps. First, the dynamic fluctuations in v_2 are determined by unfolding the statistical fluctuations to azimuthal particle distributions. Next, the magnitude of non-flow correlations is measured by utilizing the difference in pseudorapidity dependence of flow and non-flow correlations. Finally, elliptic flow fluctuations are calculated by subtracting the contribution of non-flow correlations to dynamic v_2 fluctuations. A detailed derivation of the relations between observed fluctuations, dynamic v_2 fluctuations, elliptic flow fluctuations and non-flow correlations is presented in Appendix C.

A simple Monte Carlo event generator, called Independent Cluster Model (ICM), with intrinsic flow and particle correlations has been developed as a tool to test the analysis technique. In ICM, events consist of independent clusters which decay isotropically in their rest frame. Flow is introduced by modifying the azimuthal distribution of clusters. This allows to generate event ensembles with the same particle correlation features and with different magnitudes of flow and flow fluctuations. Details of the model is provided in Appendix D. Results of measurements in ICM events are provided in this chapter for demonstration.

5.1 Dynamic v_2 Fluctuations

The observed anisotropy in heavy ion collisions will fluctuate event-by-event, even for the same magnitude of underlying elliptic flow, due to the stochastic particle production process. To account for statistical fluctuations, an "ensemble definition" of v_2 should be considered: An ensemble of events, each composed of particles the azimuthal direction, ϕ, of which are selected randomly from a distribution

$1 + 2v_2\cos(2(\phi - \phi_0))$ with a fixed v_2 value will be defined to have constant v_2 magnitude. With this definition of v_2, interpretation of dynamic fluctuations follows trivially. If an ensemble of events yields a measurement of anisotropy equivalent to an ensemble of events composed of particles the ϕ angle of which are selected randomly from a distribution $1 + 2v_2\cos(2(\phi - \phi_0))$, where v_2 is distributed with $f(v_2)$, this ensemble will be said to have a true distribution given by $f(v_2)$. Therefore the measurement of dynamic v_2 fluctuations is achieved in two steps. First the distribution of event-by-event azimuthal anisotropy is measured. Next, the corresponding underlying v_2 distribution is determined by unfolding the observed distribution.

5.1.1 Event-by-event Measurement Technique

Since statistical fluctuations in an event-by-event measurement of azimuthal particle distribution will decrease with increasing particle multiplicity, it is beneficial to use all the observed particles in any given event. Likelihood maximization provides a natural language to bring together information from different parts of the detector and to apply corrections for missing detector acceptance.

Random processes are described by a probability density which gives the frequency of occurrence of each possible outcome. Formally the outcome of a random process is represented by a random variable x, which ranges over all admissible values in the process. The probability of an outcome x of a random process is given by the Probability density function (PDF), $P(x)$. The random variable is said to be distributed as $P(x)$. In the analysis presented here the measured positions of hits on the detector (η, ϕ) represent the random variable of a sampling process. The PDF $\mathrm{P}(\eta, \phi)$ giving the probability of observing a hit at a given η and ϕ can be written as:

$$P(\eta, \phi) = p(\eta)\,[1 + 2v_2(\eta)\cos(2(\phi - \phi_0))] \tag{5.1}$$

with the normalization condition

$$\int p(\eta)\mathrm{d}\eta = \frac{1}{2\pi}. \tag{5.2}$$

Assuming that the shape of the pseudorapidity dependence does not change event-by-event, $v_2(\eta)$ can be parametrized by a single parameter $\nu_2 \equiv v_2(\eta = 0)$. Two different $v_2(\eta)$ shapes are used, referred to as triangular and trapezoidal parameterizations:

$$\begin{aligned} v_2(\eta) &= \nu_2 \times (1 - |\eta|/6) \\ v_2(\eta) &= \begin{cases} \nu_2 & \text{if } |\eta| < 2 \\ \frac{3}{2}\nu_2 \times (1 - |\eta|/6) & \text{if } |\eta| > 2. \end{cases} \end{aligned} \tag{5.3}$$

These parametrization describe the main feature of the pseudorapidity dependence of v_2 over a range of centralities, as shown in Fig. 5.1 [87].

Thus, a generative model has been constructed: Given $\mathrm{d}N/\mathrm{d}\eta$, ν_2 and ϕ_0, an event can be stochastically generated. Likelihood maximization can be applied for the

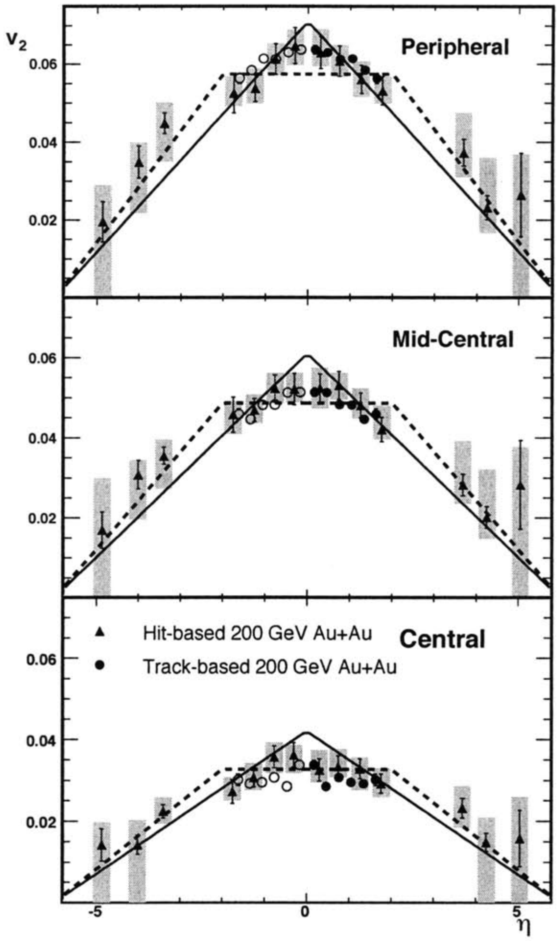

Figure 5.1: Elliptic flow as a function of pseudorapidity, $v_2(\eta)$, for charged hadrons from 200 GeV Au+Au collisions for three different centrality classes, ranging from peripheral to central (25-50%, 15-25%, and 3-15%) from top to bottom [87].

reverse problem of estimating ν_2 and ϕ_0 from the given positions of particles. Refer to the measurement, i.e. the position of particles as $X = \eta_1, \phi_1, ...\eta_n, \phi_n$ and the parameters ν_2 and ϕ_0 as Θ. The likelihood function (LF) of Θ given X is given by

$$L(\Theta|X) = p(X|\Theta) = \prod_{i=1}^{n} P(\eta_i, \phi_i|\Theta). \tag{5.4}$$

Treating the measurements X as constants and the parameters Θ as variables in the LF now allows for choosing an estimate of parameters Θ which renders L as large as possible. Instead of maximizing $L(X|\Theta)$, it is more convenient for technical reasons to minimize the auxiliary function $l(X|\Theta)$, defined as:

$$l(X|\Theta) = -\sum_{i=1}^{n} \ln[P(\eta_i, \phi_i|\Theta)]. \tag{5.5}$$

Practically, this means the ν_2 value for a given event is estimated by assuming a ν_2 value (i.e. assuming a set of parameters Θ) in the PDF and calculating the probability of measuring this event. Varying the ν_2 and ϕ_0 values in the PDF and repeating the probability calculation the "most likely" ν_2 value for the given event can be obtained. This value will be referred to as the observed result (ν_2^{obs}).

5.1.2 Calculation of Fluctuations

Let $f(\nu_2)$ be the true ν_2 distribution for a set of events, and $g(\nu_2^{\mathrm{obs}})$ the corresponding observed distribution. The true and observed distributions are related by

$$g(\nu_2^{\mathrm{obs}}) = \int K(\nu_2^{\mathrm{obs}}, \nu_2) f(\nu_2) \mathrm{d}\nu_2, \tag{5.6}$$

where $K(\nu_2^{\mathrm{obs}}, \nu_2)$ is the expected distribution of ν_2^{obs} for events with fixed input flow magnitude ν_2.

For a perfect detector, the response function for v_2 measurement on events with n particles, $K(\nu_2^{\mathrm{obs}}, \nu_2, n)$ is given by a Bessel-Gaussian distribution [50] defined as (See C.1[1]):

$$K(\nu_2^{\mathrm{obs}}, \nu_2, n) = \mathrm{BG}\left(\nu_2^{\mathrm{obs}}; \nu_2, \sigma_n\right) \equiv \frac{1}{\sigma_n^2} \exp\left(-\frac{(\nu_2^{\mathrm{obs}})^2 + \nu_2^2}{2\sigma_n^2}\right) I_0\left(\frac{\nu_2^{\mathrm{obs}}\nu_2}{\sigma_n^2}\right), \tag{5.7}$$

where $\sigma_n = 1/\sqrt{2n}$ is magnitude of the statistical fluctuations and I_0 is the modified Bessel function. The response function for a set of events in a given centrality bin is calculated by folding the response with the observed multiplicity distribution $N(n)$:

$$K(\nu_2^{\mathrm{obs}}, \nu_2) = \int K(\nu_2^{\mathrm{obs}}, \nu_2, n) N(n) \mathrm{d}n, \tag{5.8}$$

where it is assumed that the true v_2 distribution, $f(v_2)$, is independent of the number of particles for a set of events in the same centrality class.

The true event-by-event ν_2 distribution, $f(\nu_2)$, is assumed to be a Gaussian in the range $\nu_2 > 0$, with two parameters, $\bar{\nu}_2$ and σ_{ν_2}, denoting the mean and standard deviation in the given range. For given values of the parameters, it is possible to take the integral in Eq. 5.6 numerically to obtain the expected ν_2^{obs} distribution. Comparing the expected and observed distributions, the values of $\bar{\nu}_2$ and σ_{ν_2} are found by a maximum-likelihood fit. Most of the scale uncertainties, in particular those due to the pseudorapidity dependence modeling, cancel in the ratio which defines "relative dynamic fluctuations in v_2", $\sigma_{\mathrm{dyn}}/\langle v_2\rangle = \sigma_{\nu_2}/\bar{\nu}_2$.

---

[1] ν_2^{obs} is equivalent to r defined in Appendix C.1 up to a scale factor accounting for the pseudorapidity dependence of v_2.

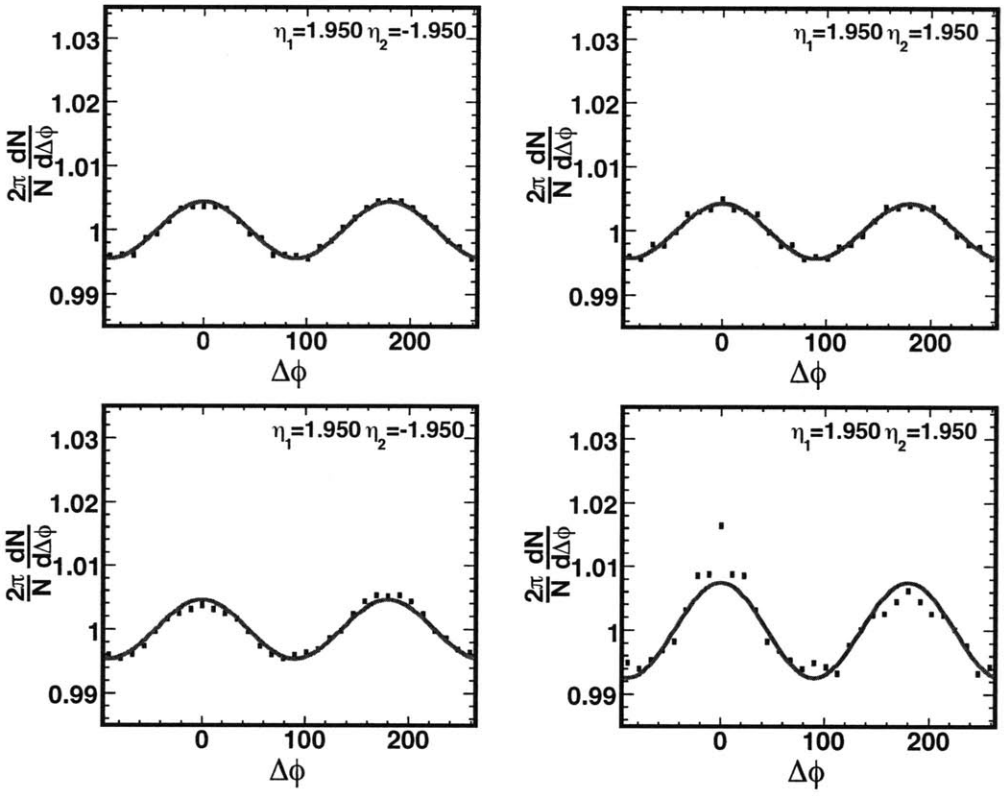

Figure 5.2: Normalized $\Delta\phi$ distributions for particle pairs from $\eta_1 = -1.95, \eta_2 = 1.95$ (left) and $\eta_1 = 1.95, \eta_2 = 1.95$ (right) for different sets of ICM events. Top row shows the distribution for events where the correlation between particles is due to elliptic flow only and the bottom row is for events with both cluster-type correlations and elliptic flow.

5.2 Non-flow Correlations

Next, the contribution of non-flow correlations to the observed dynamic v_2 fluctuations needs to be determined. If the only correlations between particles is due to elliptic flow, then the distribution of the azimuthal angular separation between particles, $\Delta\phi$, is given by $1 + 2\mathbf{V}_2 \cos(2\Delta\phi)$, where $\mathbf{V}_2 = v_2(\eta_1) \times v_2(\eta_2)$. In general, the second Fourier coefficient of the $\Delta\phi$ distribution, $\mathbf{V}_2$, has contributions from both flow and non-flow correlations.

5.2.1 Decomposition of Flow and Non-flow Correlations

Flow and non-flow contributions to azimuthal correlations can be separated with a detailed study of the η and $\Delta\eta$ dependence of the $\Delta\phi$ correlation function. Consider the distribution of $\Delta\phi$ between particles selected from two η windows centered at η_1 and η_2. The second Fourier coefficient of this distribution is given by

$$\mathbf{V}_2(\eta_1, \eta_2) \equiv \langle\cos(2\Delta\phi)\rangle\,(\eta_1, \eta_2). \tag{5.9}$$

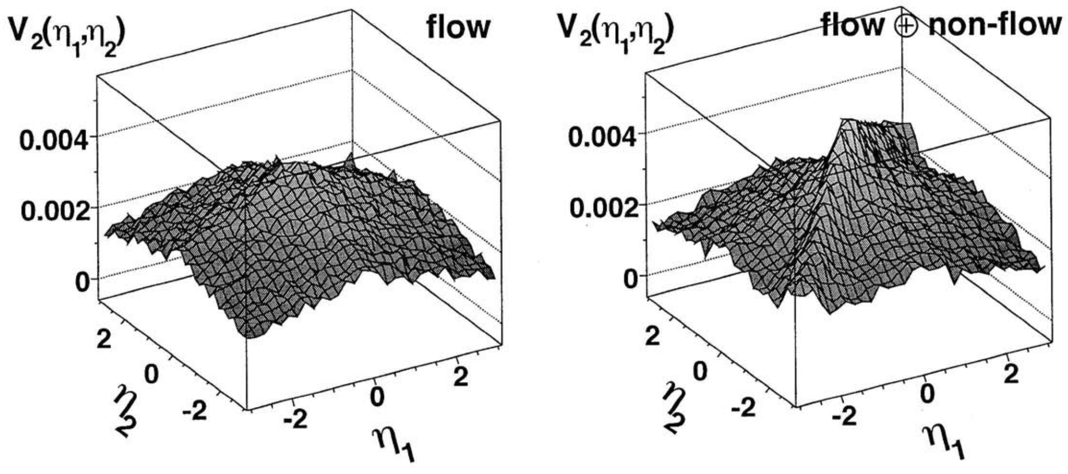

(a) Only flow correlations

(b) Flow and non-flow correlations

Figure 5.3: Distribution of $\mathbf{V}_2(\eta_1, \eta_2)$ for two sets of ICM events (a) without and (b) with non-flow correlations.

Using the fact that elliptic flow leads to a correlation between all particles in the event and creates a signal which only depends on pseudorapidity ($v_2(\eta)$), it is possible to write:

$$\mathbf{V}_2(\eta_1, \eta_2) = v_2(\eta_1) \times v_2(\eta_2) + \delta(\eta_1, \eta_2), \tag{5.10}$$

where δ is the contribution of non-flow correlations [88].

Normalized $\Delta\phi$ distributions for two sample (η_1, η_2) bins for different sets of ICM events are shown in Fig. 5.2. It can be seen that for events with no non-flow correlations $\Delta\phi$ distribution is perfectly described by a function $1 + 2\mathbf{V}_2 \cos(2\Delta\phi)$, whereas events that have non-flow correlations have a richer correlation structure at short $\Delta\eta \equiv \eta_1 - \eta_2$ range. Fig. 5.3 shows the distributions of $\mathbf{V}_2(\eta_1, \eta_2)$ for the same events. The distribution of $\mathbf{V}_2(\eta_1, \eta_2)$ is separable in η_1 and η_2 for events with no non-flow correlations. When the non-flow correlations are turned on, the contribution of two different sources to $\mathbf{V}_2(\eta_1, \eta_2)$ can be observed: a flow plateau, $v_2(\eta_1) \times v_2(\eta_2)$, which is separable in η_1 and η_2 and a non-flow ridge along the diagonal $\eta_1 = \eta_2$.

At large pseudorapidity separations, e.g. $|\Delta\eta| > 2$, the non-flow component, $\delta(\eta_1, \eta_2)$, is expected to be small. Assuming these correlations to be negligible[2], a separable function can be fit to $\mathbf{V}_2(\eta_1, \eta_2)$:

$$\mathbf{V}_2(\eta_1, \eta_2) = v_2(\eta_1)^{\text{fit}} \times v_2(\eta_2)^{\text{fit}}\,; \quad |\eta_1 - \eta_2| > 2. \tag{5.11}$$

The fit in the selected $\Delta\eta$ region can be used to extract the correlation magnitude due to flow, $v_2(\eta_1)^{\text{fit}} \times v_2(\eta_2)^{\text{fit}}$, in the whole pseudorapidity acceptance. Subtracting the

---

[2] This is true for ICM events where correlations are known to be short-ranged. In data, it is not possible to unambiguously prove that non-flow correlations at large $\Delta\eta$ separations are small. See Section 7.4 for a discussion.

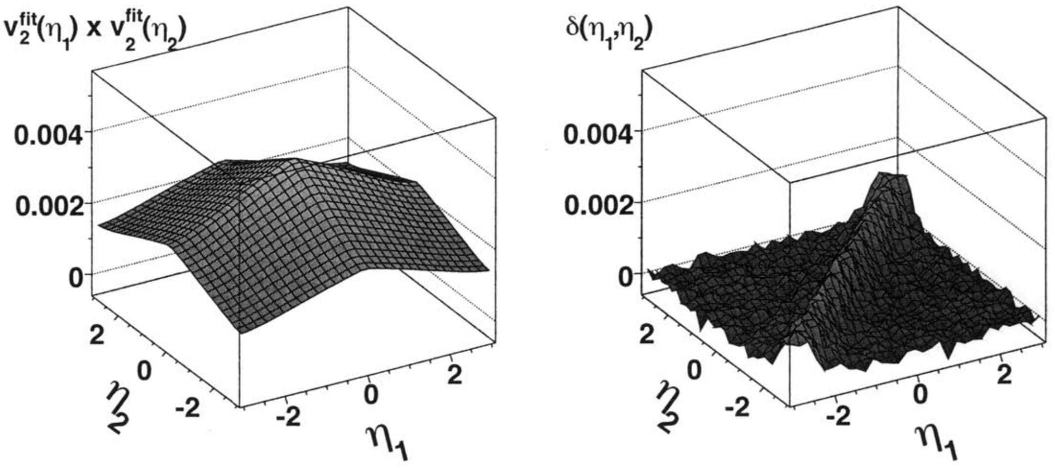

(a) Flow

(b) Non-flow

Figure 5.4: (a) Flow and (b) non-flow components of $\mathbf{V}_2(\eta_1, \eta_2)$ in Fig. 5.3(b) obtained by Eq. 5.11 and 5.12 assuming non-flow correlations at $|\Delta\eta| > 2$ are negligible.

correlations due to flow, the contribution of non-flow correlations can be determined:

$$\delta(\eta_1, \eta_2) = \mathbf{V}_2(\eta_1, \eta_2) - v_2(\eta_1)^{\text{fit}} \times v_2(\eta_2)^{\text{fit}}. \tag{5.12}$$

The two components of $\mathbf{V}_2(\eta_1, \eta_2)$ for ICM events in Fig. 5.3 are shown in Fig. 5.4. The non-flow component that is retrieved with this method is found to be equal to the Monte Carlo input non-flow within statistical errors.

Different flow measurements with different methods and pseudorapidity acceptances are influenced differently by the non-flow correlation signal. To calculate the effects of non-flow correlations on the measurement of dynamic v_2 fluctuations, the average of the $\delta(\eta_1, \eta_2)$ and $\mathbf{V}_2(\eta_1, \eta_2)$ distributions over all particle pairs can be calculated:

$$\begin{aligned} \langle \delta \rangle &= \frac{\int \delta(\eta_1, \eta_2) \frac{\mathrm{d}N}{\mathrm{d}\eta_1} \frac{\mathrm{d}N}{\mathrm{d}\eta_2} \mathrm{d}\eta_1 \mathrm{d}\eta_2}{\int \frac{\mathrm{d}N}{\mathrm{d}\eta_1} \frac{\mathrm{d}N}{\mathrm{d}\eta_2} \mathrm{d}\eta_1 \mathrm{d}\eta_2} & (5.13) \\ \langle \mathbf{V}_2 \rangle &= \frac{\int \mathbf{V}_2(\eta_1, \eta_2) \frac{\mathrm{d}N}{\mathrm{d}\eta_1} \frac{\mathrm{d}N}{\mathrm{d}\eta_2} \mathrm{d}\eta_1 \mathrm{d}\eta_2}{\int \frac{\mathrm{d}N}{\mathrm{d}\eta_1} \frac{\mathrm{d}N}{\mathrm{d}\eta_2} \mathrm{d}\eta_1 \mathrm{d}\eta_2}, & (5.14) \end{aligned}$$

where $\mathrm{d}N/\mathrm{d}\eta$ is the observed charged-particle pseudorapidity distribution. The scale uncertainties in these quantities cancel in the "non-flow ratio" given by $\langle \delta \rangle / \langle \mathbf{V}_2 \rangle$.

5.2.2 Measurement of the Correlation Function

With a perfect detector with complete particle acceptance, the distribution of $\Delta\phi$ can be easily calculated by summing over all observed particles pairs. In a real detector with imperfect particle acceptance and secondary particles from interactions with the detector, the distribution of $\Delta\phi$ is most easily calculated in the context of correlation function measurements.

Define the two-particle correlation function in two-particle $(\eta_1, \eta_2, \phi_1, \phi_2)$ space as:

$$R_n(\phi_1, \phi_2, \eta_1, \eta_2) = \left\langle \frac{\rho_n^{II}(\phi_1, \phi_2, \eta_1, \eta_2)}{\rho_n^{I}(\phi_1, \eta_1)\rho_n^{I}(\phi_2, \eta_2)} - 1 \right\rangle, \tag{5.15}$$

where

$$\rho_n^{\mathrm{I}}(\eta, \phi) = \frac{1}{n\Sigma_n}\frac{d^2\Sigma_n}{\mathrm{d}\eta\mathrm{d}\phi}$$

is the single charged particle density distribution and

$$\rho_n^{\mathrm{II}}(\eta_1, \eta_2, \phi_1, \phi_2) = \frac{1}{n(n-1)\Sigma_n}\frac{d^4\Sigma_n}{\mathrm{d}\eta_1\mathrm{d}\eta_2\mathrm{d}\phi_1\mathrm{d}\phi_2}$$

denotes the charged two-particle pair distribution. Here Σ_n is the total cross section of observing events with n charged particles. The above distributions obey the normalization relations:

$$\int \rho_n^{\mathrm{I}}(\eta, \phi)\,\mathrm{d}\eta\mathrm{d}\phi = 1$$

and

$$\int \rho_n^{\mathrm{II}}(\eta_1, \eta_2, \phi_1, \phi_2)\,\mathrm{d}\eta_1\mathrm{d}\eta_2\mathrm{d}\phi_1\mathrm{d}\phi_2 = 1.$$

In this study, the quantity of interest is the difference in azimuthal angle between paired particles. The correlation function in Eq. 5.15 is simplified by averaging over $-\pi < (\phi_1 + \phi_2)/2 < \pi$ reducing the dimensionality of the parameter space to $\Delta\phi(=\phi_1 - \phi_2)$ with a range of $|\Delta\phi| < \pi$:

$$R_n(\Delta\phi, \eta_1, \eta_2) = \left\langle \frac{\rho_n^{II}(\Delta\phi, \eta_1, \eta_2)}{\rho_n^{\mathrm{mixed}}(\Delta\phi, \eta_1, \eta_2)} - 1 \right\rangle. \tag{5.16}$$

The pair distribution $\rho_n^{\mathrm{II}}(\Delta\phi, \eta_1, \eta_2)$ is determined by taking particle pairs from the same event, then averaging over all events. The mixed-event background, $\rho^{\mathrm{mixed}}(\Delta\phi, \eta_1, \eta_2)$ is constructed by randomly selecting single particles from two different events with similar acceptance and multiplicity, representing a product of two single-particle distributions. The same-event $\rho_n^{\mathrm{II}}(\Delta\phi, \eta_1, \eta_2)$ and mixed-event distributions, $\rho^{\mathrm{mixed}}(\Delta\phi, \eta_1, \eta_2)$ are referred to as the foreground (F) and background (B) respectively. Calculating the correlation function in bins of (η_1, η_2), the foreground and background distributions can be normalized

$$\int F(\Delta\phi; \eta_1, \eta_2)\mathrm{d}\Delta\phi = 1 \tag{5.17}$$

$$\int B(\Delta\phi; \eta_1, \eta_2)\mathrm{d}\Delta\phi = 1 \tag{5.18}$$

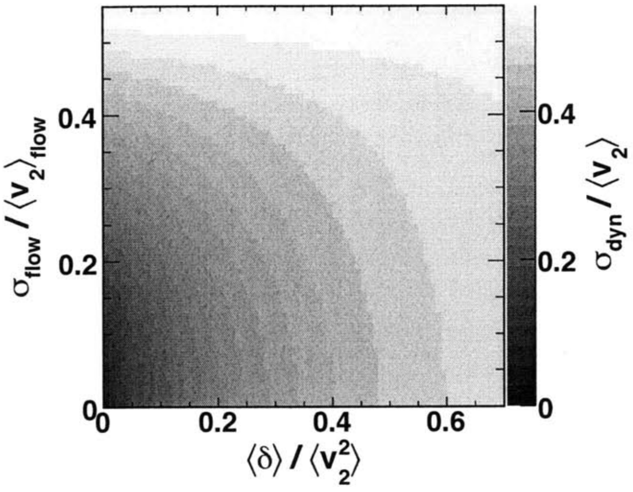

Figure 5.5: Dynamic v_2 fluctuations ($\sigma_{\rm dyn}/\langle v_2 \rangle$) as a function of elliptic flow fluctuations ($\sigma_{\rm flow}/\langle v_2 \rangle_{\rm flow}$) and non-flow ratio ($\langle \delta \rangle / \langle \mathbf{V}_2 \rangle$) for $\sigma_n/\langle v_2 \rangle_{\rm flow} = 0.6$.

for each (η_1, η_2) bin. In the case of complete detector acceptance, the background distribution will be flat in the $\Delta\phi$ direction. The correlation function defined in this way accurately accounts for missing particle acceptance leading to

$$\mathbf{V}_2(\eta_1, \eta_2) = \frac{1}{\pi} \int R_n(\Delta\phi; \eta_1, \eta_2) \cos(2\Delta\phi) \mathrm{d}\Delta\phi \tag{5.19}$$

for any acceptance with complete $\Delta\phi$ coverage.

5.3 Elliptic Flow Fluctuations

For a perfect detector, elliptic flow fluctuations can be obtained by modifying the response function defined in Eq. 5.7 to account for non-flow correlations. In the measurement of real data, it is preferable to calculate the magnitude of elliptic flow fluctuations from the final values of relative dynamic v_2 fluctuations, $\sigma_{\rm dyn}/\langle v_2 \rangle$ and non-flow ratio, $\langle \delta \rangle / \langle \mathbf{V}_2 \rangle$, such that the systematic uncertainties from the both measurements are reduced.

The calculation of elliptic flow fluctuations ($f_{\rm flow}(v_2)$) from measured dynamic fluctuations ($f_{\rm dyn}(v_2)$) can be summarized by the following equation:

$$\int_0^1 K_n(v_2^{\rm obs}, v_2) f_{\rm dyn}(v_2) \mathrm{d}v_2 = \int_0^1 K_{n,\delta}(v_2^{\rm obs}, v_2) f_{\rm flow}(v_2) \mathrm{d}v_2, \tag{5.20}$$

where $K_n(v_2^{\rm obs}, v_2)$ and $K_{n,\delta}(v_2^{\rm obs}, v_2)$ are the response functions for an ideal detector with and without non-flow correlations respectively. Equation 5.20 gives the distribution of observed anisotropy $g(v_2^{\rm obs})$, such that on the left hand side the non-flow correlations are encoded in the dynamic v_2 fluctuations, and on the right hand side,

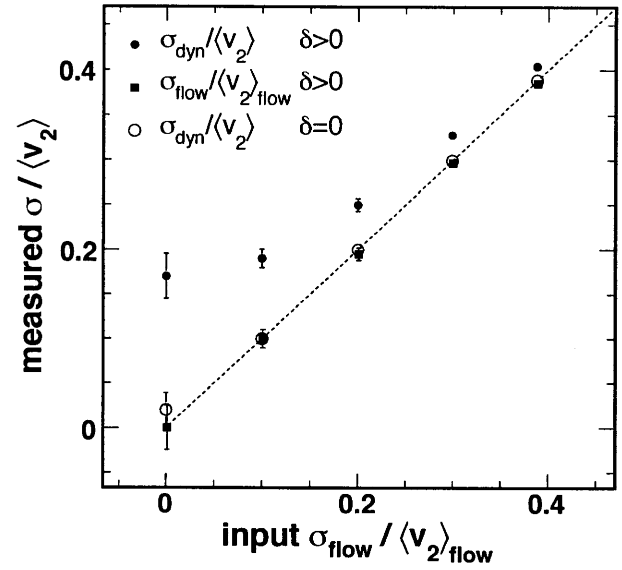

Figure 5.6: Measured scaled fluctuations ($\sigma_{\text{dyn}}/\left\langle v_2\right\rangle$, $\sigma_{\text{flow}}/\left\langle v_2\right\rangle_{\text{flow}}$) in ICM events as a function of the input flow fluctuations. Filled (open) circles show the extracted dynamic v_2 fluctuations for events with (without) cluster-type correlations. Squares show the measured value of $\sigma_{\text{flow}}/\left\langle v_2\right\rangle_{\text{flow}}$ for events with cluster-type correlations, obtained by correcting the results of dynamic v_2 fluctuations measurement (filled circles) for non-flow correlations as described in the text.

they are accounted for in the response function $K_{n,\delta}(v_2^{\text{obs}}, v_2)$. The response functions $K_n(v_2^{\text{obs}}, v_2)$ and $K_{n,\delta}(v_2^{\text{obs}}, v_2)$ are given by (see Eq. 5.7):

$$\begin{aligned} K_{n,\delta}(v_2^{\text{obs}}, v_2) &= \text{BG}\left(v_2^{\text{obs}}; v_2, \sqrt{\sigma_n^2 + \sigma_\delta^2}\right) && (5.21) \\ K_n(v_2^{\text{obs}}, v_2) &= \text{BG}\left(v_2^{\text{obs}}; v_2, \sigma_n\right), && (5.22) \end{aligned}$$

where $\sigma_\delta = \sqrt{\langle\delta\rangle/2}$.

Equation 5.20 cannot be simplified analytically. However, it can be solved numerically to calculate relative elliptic flow fluctuations ($\sigma_{\text{flow}}/\left\langle v_2\right\rangle_{\text{flow}}$) that correspond to the measured dynamic v_2 fluctuations ($\sigma_{\text{dyn}}/\left\langle v_2\right\rangle$) and the non-flow ratio ($\langle\delta\rangle / \langle \mathbf{V}_2\rangle$). The details of the numerical calculation are given in Appendix C. The resulting relation between $\sigma_{\text{dyn}}/\left\langle v_2\right\rangle$, $\sigma_{\text{flow}}/\left\langle v_2\right\rangle_{\text{flow}}$ and $\langle\delta\rangle / \langle \mathbf{V}_2\rangle$ is plotted in Fig. 5.5.

The complete analysis procedure described in this chapter has been applied to ICM events. Fig. 5.6 shows the measured elliptic flow fluctuations as a function of input elliptic flow fluctuations for two sets of events with and without non-flow correlations. The results demonstrate that the analysis procedure is successful in reconstructing the input elliptic flow fluctuations.

6 Measurement of Dynamic v_2 Fluctuations

Following the development of the formalism and methodology in Chapter 5, the procedure of obtaining dynamic v_2 fluctuations in the data is described in this chapter. Various corrections to reconstruct the observables in the real detector environment is provided and studies of systematic uncertainties are outlined. The results are presented as a function of collision centrality [89].

The data presented in this chapter for Au+Au collisions at $\sqrt{s_{\rm NN}} = 200$ GeV were collected during RHIC Run 4 (2004) using the large-acceptance PHOBOS multiplicity array consisting of the Octagon, Vertex and Ring detectors with the PHOBOS magnet turned off. Events which passed the quality cuts described in Sect. 4.4 were further selected to be within $|z_{\rm vtx}| < 10$ GeV using the *RMSSelVertex* algorithm and 6-45% most central bins using PdlMean cuts. The analysis is performed in 2 cm wide $z_{\rm vtx}$ and 5% wide centrality bins (except the most central bin, which is 6-10% central). Total number of events selected for the analysis is 450k.

6.1 Event-by-event Measurement of $v_2^{\rm obs}$

A method for the event-by-event measurement of $v_2^{\rm obs}$ has been introduced in Sect. 5.1.1. The method needs to be modified slightly in a real detector environment to take into account the (η, ϕ) coverage of the PHOBOS multiplicity array.

The variation in angular particle acceptance of the PHOBOS multiplicity array can be seen in Fig. 6.1, which shows the distribution of reconstructed hits for a set of Au+Au events at $\sqrt{s_{\rm NN}} = 200$ GeV. Consider the PDF defined in Eq. 5.1:

$$P(\eta, \phi) = p(\eta)\,[1 + 2v_2(\eta)\cos(2(\phi - \phi_0))]\,. \tag{6.1}$$

This PDF folded with the detector acceptance will have a different integral for different sets of parameters (v_2 and ϕ_0). If this PDF is used to measure the likelihood of the parameters, the maximum likelihood estimator will yield values that have a higher integral in the acceptance folded PDF. This bias can be removed by normalizing the PDF as a function of v_2 and ϕ_0 for different values of η. For this purpose, the normalization parameter, $s(\eta, v_2, \phi_0)$, is introduced. Taking out pseudorapidity probability distribution $p(\eta)$, which does not play a role in the likelihood calculation, the scaled probability of observing a hit at a certain ϕ angle is defined as

$$P(\phi) = s(\eta, v_2, \phi_0) \times [1 + 2v_2(\eta)\cos(2(\phi - \phi_0))]\,. \tag{6.2}$$

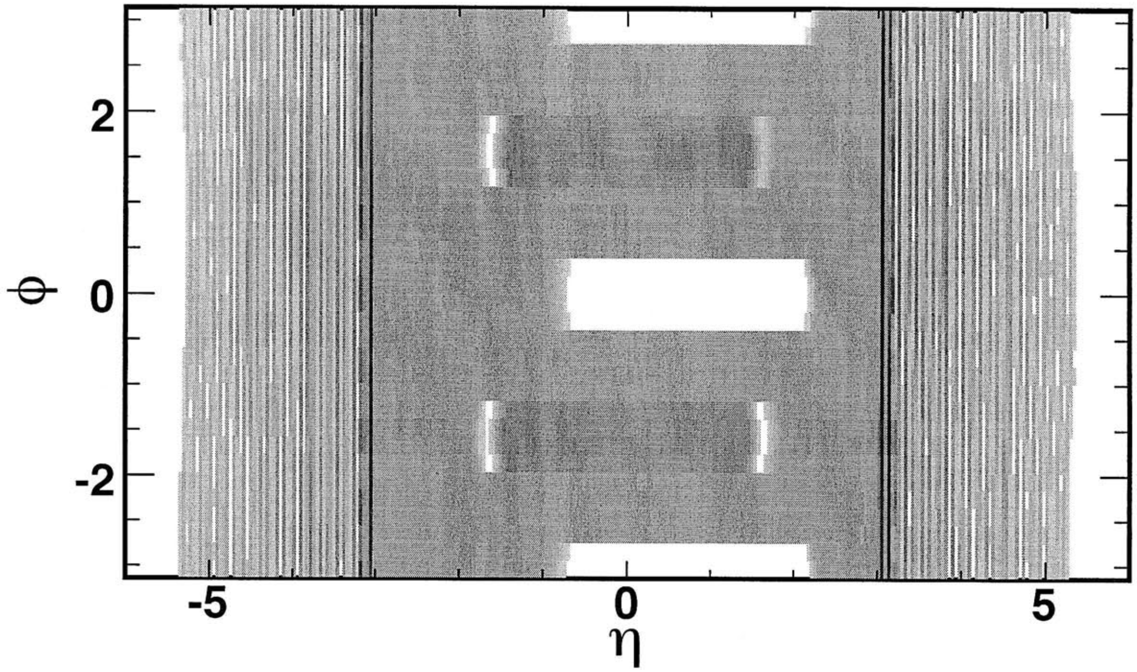

Figure 6.1: Positions of the reconstructed hits on the PHOBOS multiplicity array in a set of events from the Run 4 data selected to be within $|z_{\mathrm{vtx}}| < 1$ cm.

The normalization parameter $s(\eta, \nu_2, \phi_0)$ is calculated in bins of pseudorapidity for each vertex and centrality bin. For a given vertex bin, a pseudorapidity bin corresponds to a group of silicon pads on the multiplicity array. Define the hit rate of a pad with index i (h_i) as how often a pad gets hit for a given centrality and vertex bin. The normalization parameter s is then given as:

$$s(\eta, v_2, \phi_0) = \frac{\sum_i h_i}{\sum_i h_i[1 + 2v_2(\eta_i)\cos(2(\phi_i - \phi_0))]}. \tag{6.3}$$

The PDF defined in Eq. 6.2 accurately accounts for missing acceptance in the detector. Using this PDF, ν_2^{obs} is estimated event-by-event by likelihood maximization as described in Sect. 5.1.1. The event-by-event measurement is performed twice, once for each $v_2(\eta)$ distribution assumption, triangular and trapezoidal, given in Eq. 5.3. Fig. 6.2 shows the distribution of ν_2^{obs} for a set of events using the triangular $v_2(\eta)$ assumption.

6.2 The Response Function

In Sect. 5.1.2, the procedure to obtain relative v_2 fluctuations from the ν_2^{obs} distribution was introduced. This procedure involves unfolding the true ν_2 distribution from the observed ν_2^{obs} distribution using the relation given in Eq. 5.6 with the response function $K(\nu_2^{\mathrm{obs}}, \nu_2, n)$ given in Eq. 5.7.

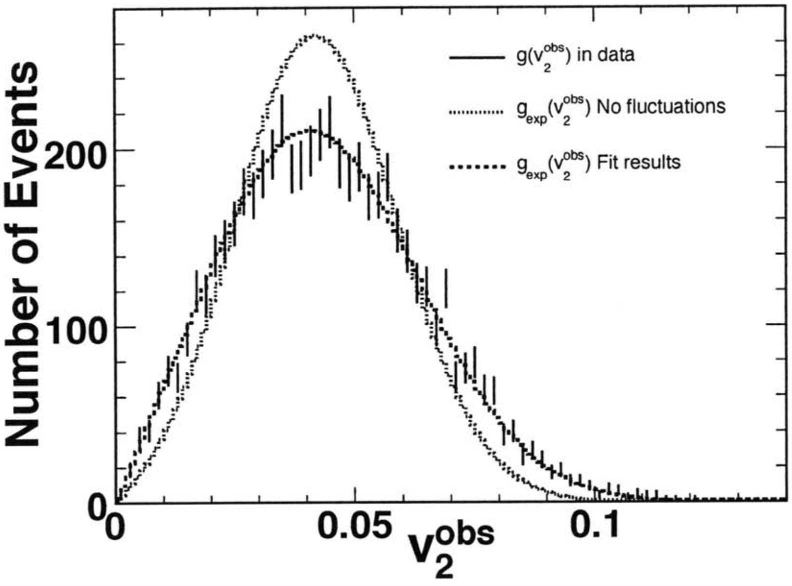

Figure 6.2: Distribution of the event-by-event measured quantity $\nu_2^{\rm obs}$ for 40-45% central events within $-2 < z_{\rm vtx} < 0$. Dashed lines shows expected distributions for different values of $\sigma_{\rm dyn}$.

In a real detector environment, the $\nu_2^{\rm obs}$ signal is diluted by various effects such as production of secondary particles from the interaction of primary particles with the detector. To determine the response function modified by this dilution effect, the event-by-event analysis is performed on GEANT simulations of the detector response based on the HIJING event generator. The HIJING model does not incorporate elliptic flow effects. Flow is introduced to the model by redistributing the generated particles in each event in the ϕ direction according to the probability distribution $[1 + 2v_2(\eta)\cos(2(\phi - \phi_0))]$. For the two parameterizations of $v_2(\eta)$, triangular and trapezoidal, used in the event-by-event measurement, the corresponding response functions, $K^{\rm tri}$ and $K^{\rm trap}$, are calculated. Fitting smooth functions through the observed response functions decreases bin-to-bin fluctuations and allows for interpolation in ν_2 and n. The dilution of the v_2 signal is observed to be well modeled by the introduction of four parameters to the perfect detector response:

$$K(\nu_2^{\rm obs}, \nu_2, n) = \frac{\nu_2^{\rm obs}}{(\sigma^{\rm mod})^2} \times \exp\left(-\frac{\left(\nu_2^{\rm obs}\right)^2 + \left(\nu_2^{\rm mod}\right)^2}{2(\sigma^{\rm mod})^2}\right) I_0\left(-\frac{\nu_2^{\rm obs}\nu_2^{\rm mod}}{(\sigma^{\rm mod})^2}\right), \qquad (6.4)$$

with $\nu_2^{\rm mod} = (A + Bn)\nu_2$ and $\sigma^{\rm mod} = (C + D\sqrt{n})\sigma_n$.

The values of the four dilution parameters A, B, C and D are obtained by fits to observed $K(\nu_2^{\rm obs}, \nu_2, n)$ in the modified HIJING samples in $z_{\rm vtx}$ bins. The values of the parameters are plotted as a function of $z_{\rm vtx}$ in Fig. 6.3 for the triangular $v_2(\eta)$ distribution. The detector response function shows a suppression in the extracted flow signal ($A < 1$) more so with increasing multiplicity ($B < 0$). The magnitude

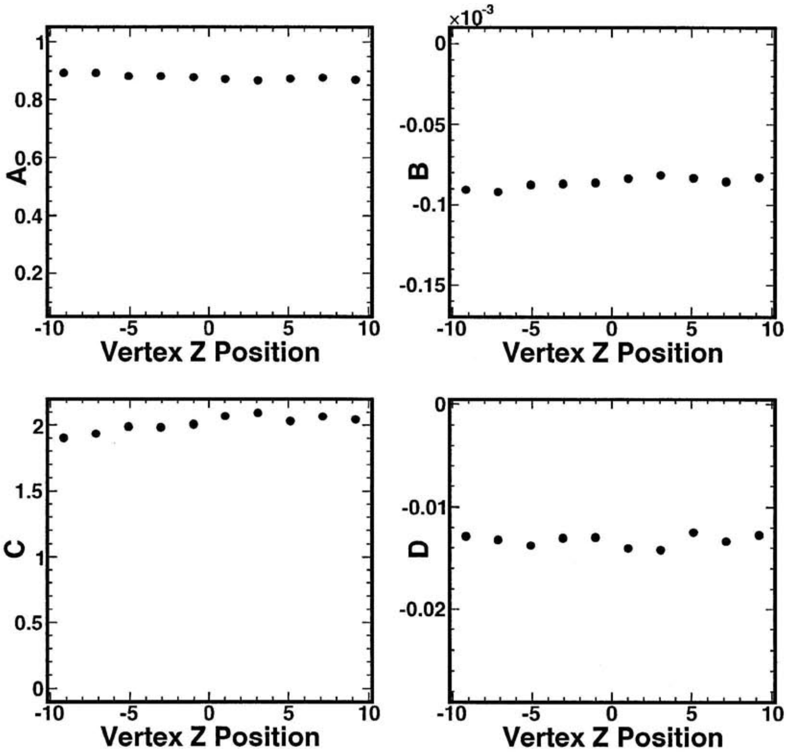

Figure 6.3: The values of the four modified response function parameters defined in Eq. 6.4 as a function of z_{vtx}.

of statistical fluctuations (σ_n) is relatively less modified ($C = 1.1 \pm 0.1$) and also shows a slight suppression with increasing multiplicity ($D < 0$). Overall the effect of statistical fluctuations ($\sim C/A$) is enhanced due to the detector response.

The corresponding response function for a set of data events in a given centrality bin is calculated by folding the modified response with the observed multiplicity distribution (see Eq. 5.8). The resulting response function, $K(\nu_2^{\mathrm{obs}}, \nu_2)$, for 40-45% central events within $-2 < z_{\mathrm{vtx}} < 0$ is shown in Fig. 6.4.

6.3 Results

The quantities $\bar{\nu}_2$ and σ_{ν_2} are obtained by unfolding the distribution of ν_2^{obs} with the corresponding response function for each centrality and vertex bin as described in Sect. 5.1.2. The results over different vertex bins are then averaged. The complete analysis chain is repeated for triangular and trapezoidal $v_2(\eta)$ distributions given in Eq. 5.3 and the results from the two methods are averaged. The averages are

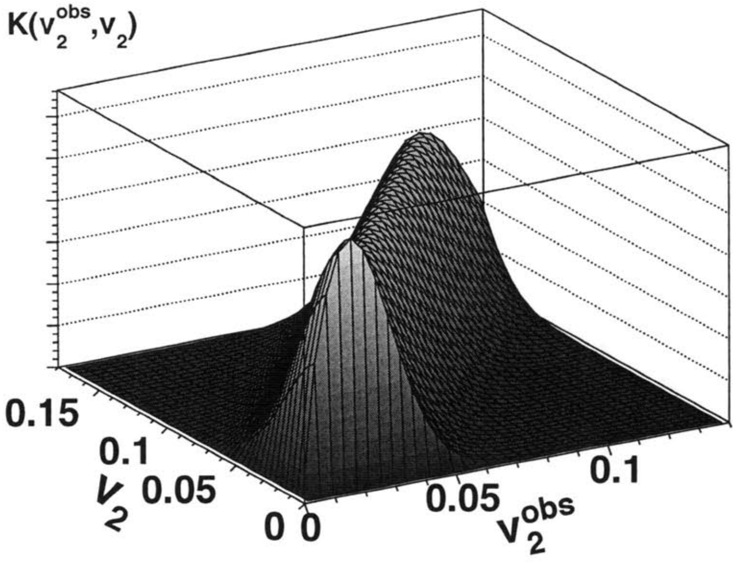

Figure 6.4: Response function, $K(\nu_2^{\rm obs}, \nu_2)$, for 40-45% central events within $-2 < z_{\rm vtx} < 0$. Each ν_2 slice represents the expected $\nu_2^{\rm obs}$ distribution for a measurement on events with a constant value of ν_2.

calculated to obtain estimates of $\langle v_2 \rangle$ and $\sigma_{\rm dyn}$ in the region $|\eta| < 1$.

$$\langle v_2 \rangle = 0.5 \left(\frac{11}{12} \bar{\nu}_2^{\rm tri} + \bar{\nu}_2^{\rm trap} \right) \tag{6.5}$$

$$\sigma_{\rm dyn} = 0.5 \left(\frac{11}{12} \sigma_{\nu_2}^{\rm tri} + \sigma_{\nu_2}^{\rm trap} \right), \tag{6.6}$$

where the factor $\frac{11}{12}$ comes from integration over η. Finally, the induced v_2 fluctuations arising from fluctuations in the number of participating nucleons are calculated by parameterizing the $\langle v_2 \rangle$ versus $N_{\rm part}$ results and folding them with the $N_{\rm part}$ distribution in each centrality bin.

Fig. 6.5 shows the mean, $\langle v_2 \rangle$, and the standard deviation, $\sigma_{\rm dyn}$, of the true v_2 distribution at midrapidity as a function of the number of participating nucleons, in Au+Au collisions at $\sqrt{s_{\rm NN}} = 200$ GeV for 6-45% most central events. The results for $\langle v_2 \rangle$ are in agreement with the previous PHOBOS v_2 measurements [90], which were obtained with the event-plane method for charged hadrons within $|\eta| < 1$. The uncertainties in $\mathrm{d}N/\mathrm{d}\eta$ and $v_2(\eta)$, as well as differences between HIJING and the data in these quantities, introduce a large uncertainty in the overall scale in the event-by-event analysis due to the averaging procedure over the wide pseudorapidity range. Because of these scale errors, which dominate the systematic uncertainty on $\langle v_2 \rangle$ and $\sigma_{\rm dyn}$, a detailed comparison of the $\langle v_2 \rangle$ results from this analysis to previous measurements is not possible.

Most of the scale errors cancel in the ratio, $\sigma_{\rm dyn}/\langle v_2 \rangle$, which defines "relative dynamic v_2 fluctuations", shown in Fig. 6.6 as a function of the number of participating

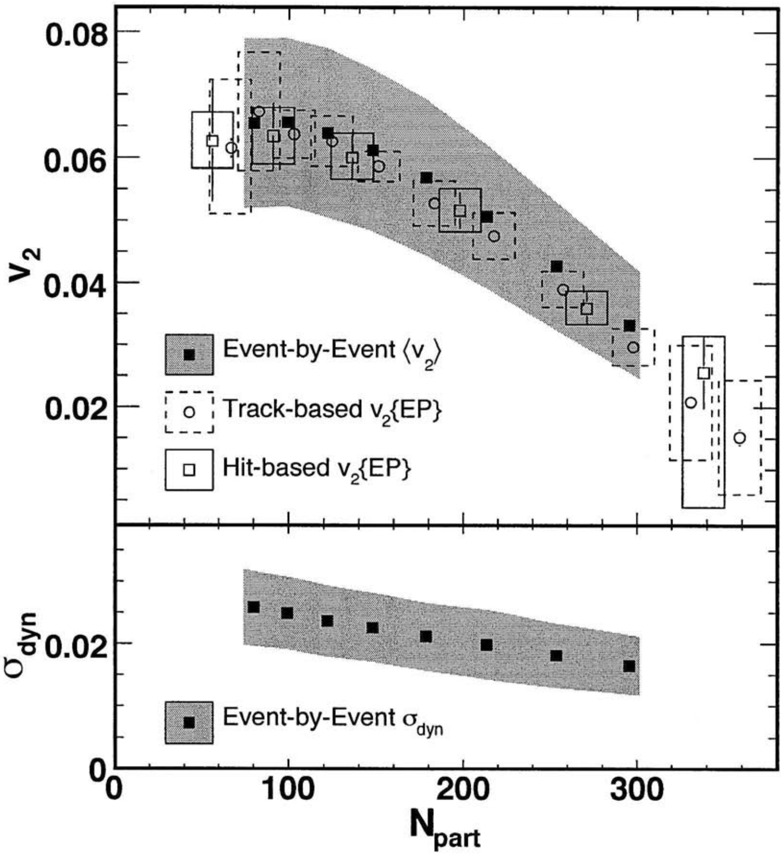

Figure 6.5: $\langle v_2 \rangle$ (top) and σ_{dyn} (bottom) versus N_{part} for Au+Au collisions at $\sqrt{s_{\text{NN}}} = 200$ GeV. Previously published event-plane v_2 results for the same collision system are shown for comparison [90]. Boxes and gray bands show 90% C.L. systematic errors and the error bars represent 1-σ statistical errors. The results are for $0 < \eta < 1$ for the track-based method and $|\eta| < 1$ for hit-based and event-by-event methods.

nucleons. Large relative fluctuations of approximately 40% are observed.

The measured dynamic fluctuations in v_2 are directly comparable to models that incorporate both elliptic flow and two-particle correlations. Furthermore, without making any assumptions about non-flow, these data establish an upper limit on the magnitude of underlying elliptic flow fluctuations. Also shown in Fig. 6.6 are $\sigma_{\varepsilon_{\text{part}}} / \langle \varepsilon_{\text{part}} \rangle$ at fixed values of N_{part} obtained in MC Glauber [66] and Color Glass Condensate (CGC) [91] calculations. The 90% confidence level systematic errors for MC Glauber calculations (shown as a contour line in Fig. 6.6) are estimated by varying Glauber parameters as discussed in Ref. [35]. The CGC model calculations are based on participant-nucleon-position fluctuations in the Glauber model and take into account gluon saturation effects at low momentum, leading to a higher value of average eccentricity [91]. Due to the uncertainties in non-flow effects discussed previously, it is not possible to conclude which of these two models is more consistent

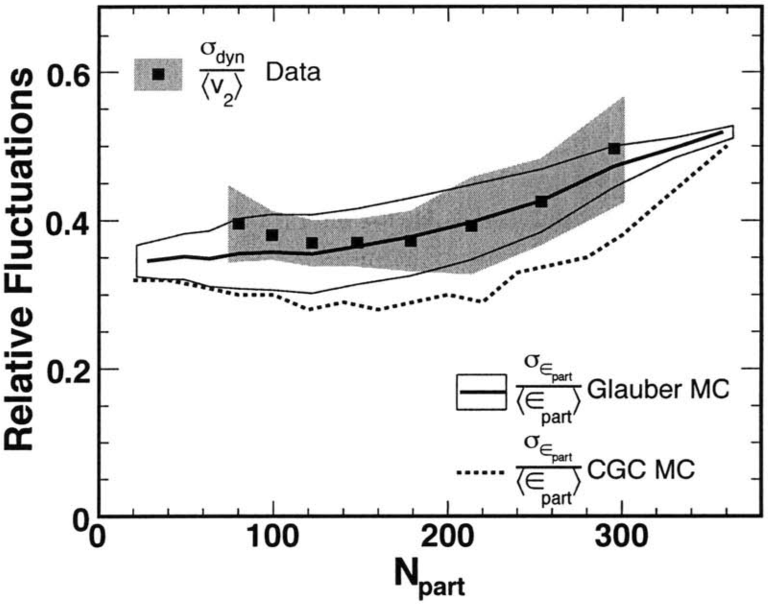

Figure 6.6: Dynamic v_2 fluctuations, $\sigma_{\text{dyn}}/\langle v_2 \rangle$, as a function of number of participating nucleons, N_{part}, for Au+Au collisions at $\sqrt{s_{\text{NN}}} = 200$ GeV. The continuous and dashed thick black lines show $\sigma(\epsilon_{part})/\langle \epsilon_{part} \rangle$ calculated in Glauber MC and CGC [91] models, respectively. The shaded grey band (for data) and thin black contour line (for Glauber MC) show 90% C.L. systematics errors.

with the measured dynamic v_2 fluctuations. A more proper comparison can be made in Ch. 7 after the contribution of non-flow correlations to the measured v_2 fluctuations is subtracted.

6.4 Systematic Errors

Systematic errors have been investigated in three main classes: variations to the event-by-event analysis, response of the measurement to known input σ_{dyn}, and intrinsic differences between HIJING events and data. Various modifications to the event-by-event analysis have been applied. Corrections, used in the hit-based event-plane analysis [90, 92], to account for signal dilution due to detector occupancy and to create an appropriately symmetric acceptance have been applied to both HIJING and data events. Hit definitions have been varied. These changes lead to at most 4% variations in the observed relative fluctuations demonstrating a good understanding of the response function. The determination of the response function and the final fitting procedure have been studied by performing the analysis on sets of modified HIJING events with varying input σ_{dyn}. Differences between input and reconstructed σ_{dyn} have been identified as a contribution to the systematic uncertainty. The sensitivity of the measurement has been observed to be limited for very low $\langle v_2 \rangle$ values.

Therefore the 0-6% most central events, where the reconstructed $\langle v_2 \rangle$ is below 3%, have been omitted. Differences between HIJING and data in terms of $\mathrm{d}N/\mathrm{d}\eta$, and $v_2(\eta)$ can, in principle, lead to a miscalculation of the response function. A sample of MC events has been generated, in which the $\mathrm{d}N/\mathrm{d}\eta$ distribution of HIJING events is widened by a simple scaling to match the measurements in data. The difference between results obtained with and without this modification, as well as the difference between results with two different parameterizations of $v_2(\eta)$ are identified as contributions to the systematic uncertainty. Other systematic studies include using a flat, rather than Gaussian, ansatz for the true ν_2 distribution, $f(\nu_2)$, and performing the analysis in different collision vertex and event-plane angle bins. The uncertainty in the contribution of N_{part} induced fluctuations has also been estimated via different parameterizations of the $\langle v_2 \rangle$ versus N_{part} results. Contributions from all error sources described above are added in quadrature to derive the 90% confidence level error shown in Figures 6.5 and 6.6.

7 Measurement of Non-flow Correlations and Elliptic Flow Fluctuations

The analysis procedure to measure non-flow correlations was described in Sect. 5.2. In this chapter, the application of this procedure to the PHOBOS detector is presented. The corrections to reconstruct the observables in the real detector environment are described and studies of systematic uncertainties are outlined. The effect of non-flow correlations at large pseudorapidity separations to the analysis is discussed. Finally, results on non-flow ratio and elliptic flow fluctuations are presented [93].

In the analysis of non-flow correlations, a similar event selection is applied as the dynamic v_2 fluctuation measurement presented in Chapter 6. The study of non-flow correlations is performed on the larger statistics data collected with the PHOBOS magnet turned on during the same RHIC Run. The total number of events selected for this analysis is 10 million. The correction procedure in correlation analyses for the incomplete particle acceptance of the detector necessitates a more precise understanding of the detector in small bins of geometric acceptance. To obtain a more uniform signal, only the hits in the octagon detector are utilized in this analysis. The analysis is also performed in finer vertex bins of width 0.2 cm in the range $|z_{\mathrm{vtx}}|<6$.

7.1 Preliminary Results of Raw Data

Figure 7.1 shows the $\Delta\phi$ foreground and background distributions and the corresponding correlation function for a set of data events in a narrow centrality and collision vertex bin for illustrative (η_1, η_2) bins. The irregular structures which exist in both the foreground and background distributions are due to the geometric particle acceptance of the detector. However, after dividing the foreground by the background, all the structures induced by the detector acceptance are essentially canceled out in the correlation function $R_n(\Delta\phi, \eta_1, \eta_2)$.

Correlation function results from different vertex bins are averaged and the second Fourier coefficient is calculated to yield $\mathrm{V}_2(\eta_1, \eta_2)$, shown in Fig. 7.2(a). The expected plateau and ridge features, due to contributions from flow and non-flow can be observed. However, along the ridge, the $\mathrm{V}_2(\eta_1, \eta_2)$ distribution appears to have unphysical structures. Similar irregularities are also observed in $\mathrm{V}_2(\eta_1, \eta_2)$ distribution in simulated Monte Carlo events in Fig. 7.2(b). MC studies show that these structures are mainly contributed by the secondary detector effects such as

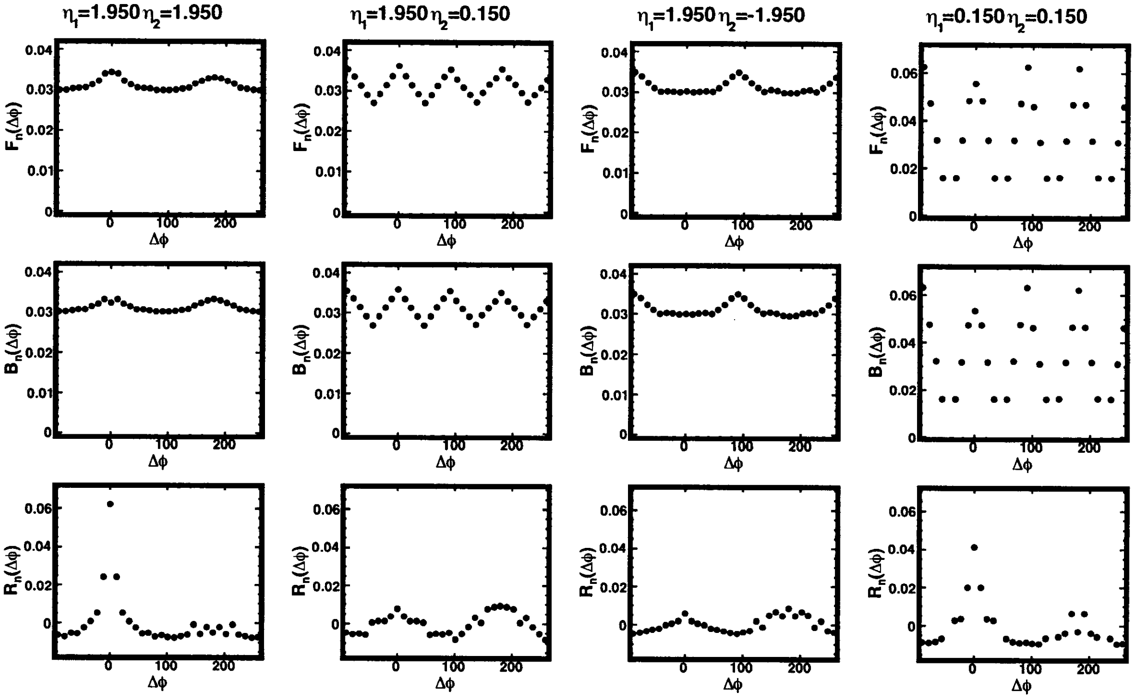

Figure 7.1: The raw foreground (top), background (middle) and correlation function (bottom) distributions as a function of $\Delta\phi$ in different η_1, η_2 bins (columns) for 40-45% most central events within the vertex range $0 < z_{\rm vtx} < 0.2$ cm.

δ-electrons[1], γ conversions[2] and weak decays.

7.2 Correction Procedure to Raw Correlation Function

With the single layer silicon Octagon detector, only one hit from each charged particle track can be measured. Secondary effects which are mainly caused by the interactions between primary particles and experimental material (beam pipe, detector etc.), such as δ-electrons, γ conversions and weak decays cannot be directly rejected. These effects modify the shape of the measured correlation function, especially at short-range in $\Delta\eta$ as discussed in the previous section.

The overall correlation structure consists of both intrinsic and secondary correlations and these two sources of correlations are found to be largely independent of each other in MC studies, i.e. the correlation from secondaries is mostly determined by sensor thickness, detector geometry, known cross-sections and decay kinemat-

---

[1] Electrons knocked out from the detector material by energetic charged particles.

[2] photons converting into an e^+e^- pair via interactions with the detector material.

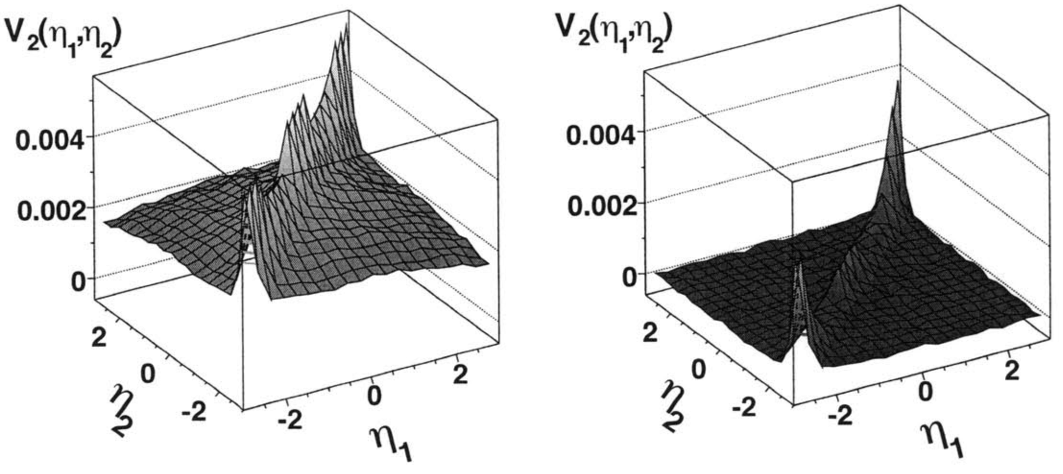

(a) Data

(b) Simulated HIJING

Figure 7.2: Distribution of raw $\mathbf{V}_2(\eta_1, \eta_2)$ for (a) 40-45% most central data and (b) 30-45% most central simulated HIJING (same average multiplicity as data) events.

ics.[3] Within a narrow vertex range (0.2 cm), the generator level MC correlation function, $R^{\mathrm{MC}}_{n\ \mathrm{pri}}(\Delta\phi, \eta_1, \eta_2)$, is compared to the correlation function observed after processing the same MC events with all the primary hadrons through the GEANT simulation, $R^{\mathrm{MC}}_{n\ \mathrm{sim}}(\Delta\phi, \eta_1, \eta_2)$. The difference between the two correlation functions, $S(\Delta\phi, \eta_1, \eta_2)$, is attributed to the effects of secondary interactions, weak decays, and

---

[3] To be precise, the correlation from secondaries also depends on the multiplicity, if quantified by the correlation function R_n. Since the number of pairs increase as $\sim n^2$, pairwise correlations, such as those between primary and secondary particles are diluted in the measure R_n. This effect does not play a role in this study since Monte Carlo events that have the same multiplicity as data are used for each centrality bin. Correlation studies focused on measuring pairwise correlation strength use correlation measures such as $R \equiv \langle (n-1)(F/B-1) \rangle$ which are not diluted by increasing multiplicity.

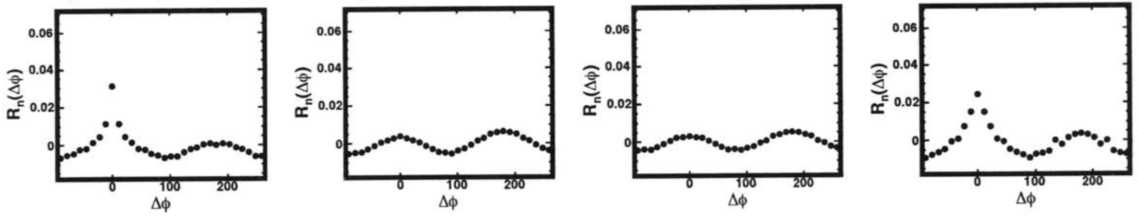

Figure 7.3: The corrected correlation function distribution as a function of $\Delta\phi$ in different η_1, η_2 bins for 40-45% most central events averaged over the vertex range $-6 < z_{\mathrm{vtx}} < 6\mathrm{cm}$.

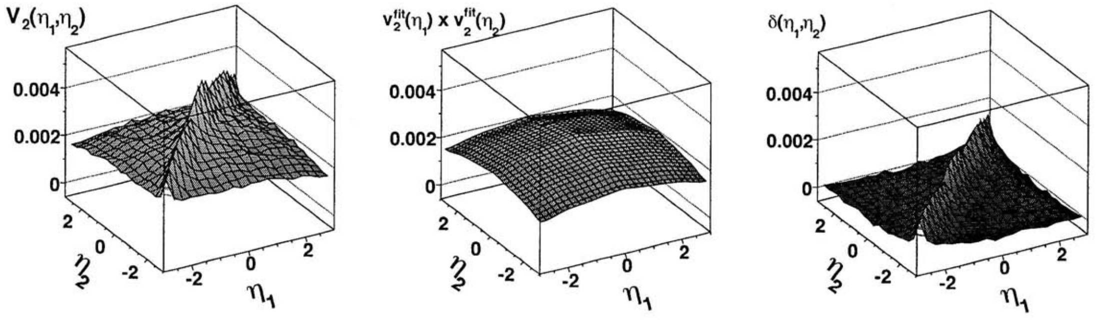

(a) (b) (c)

Figure 7.4: (a) Distribution of corrected $\mathbf{V}_2(\eta_1, \eta_2)$ for 40-45% most central Au+Au collisions at $\sqrt{s_{\mathrm{NN}}} = 200$ GeV. (b) Flow and (c) Non-flow components of the $\mathbf{V}_2(\eta_1, \eta_2)$ distribution in (a) assuming non-flow correlations at $|\Delta\eta| > 2$ are negligible.

the reconstruction procedure:

$$\begin{aligned} S(\Delta\phi, \eta_1, \eta_2) &= R^{\mathrm{MC}}_{n\ \mathrm{sim}}(\Delta\phi, \eta_1, \eta_2) - R^{\mathrm{MC}}_{n\ \mathrm{pri}}(\Delta\phi, \eta_1, \eta_2) && (7.1) \\ R^{\mathrm{data}}_{n}(\Delta\phi, \eta_1, \eta_2) &= R^{\mathrm{data}}_{n\ \mathrm{raw}}(\Delta\phi, \eta_1, \eta_2) + S(\Delta\phi, \eta_1, \eta_2). && (7.2) \end{aligned}$$

Fig. 7.3 shows the corrected correlation function $R_n(\Delta\phi, \eta_1, \eta_2)$, for the same event and pseudorapidity selection as Fig. 7.1. The resulting $\mathbf{V}_2(\eta_1, \eta_2)$ distribution for these events is shown in Fig. 7.4(a). The flow and non-flow components of the $\mathbf{V}_2(\eta_1, \eta_2)$ distribution in Fig. 7.4(a), shown in Figures 7.4(b) and(c), are obtained by the fit function defined in Eq. 5.11, assuming that non-flow correlations are negligible for $|\Delta\eta| > 2$. The non-flow ratio is calculated from the fit results as described in Sect. 5.2.1.

7.3 Systematic Errors

The systematic uncertainty has been evaluated for the various stages of the non-flow ratio calculation including the calculation of the correlation function and the fit to $\mathbf{V}_2(\eta_1, \eta_2)$ to obtain the non-flow ratio. A "digital" occupancy correction with only the event-by-event hit density distribution and no $\mathrm{d}E/\mathrm{d}x$ information has been used. Hits on the Vertex detector, which has a different granularity from the Octagon detector have been added to the analysis. Monte Carlo samples with different average multiplicity from the data have been used in the correction procedure. The $\Delta\eta$ cut used in the fit has been varied between 1.2 and 2.7[4]. Different fit functions $v_2(\eta)^{\mathrm{fit}}$ have been used from second order up to eighth order polynomials. Finally

---

[4] The Octagon detector with a pseudorapidity coverage of $-3 < \eta < 3$ allows particle pairs to be studied up to $\Delta\eta = 6$. However, in this study the $\Delta\eta$ cut is constrained to $\Delta\eta_c < 3$ such that particles from all η values contribute in the fit to obtain $v_2(\eta)$.

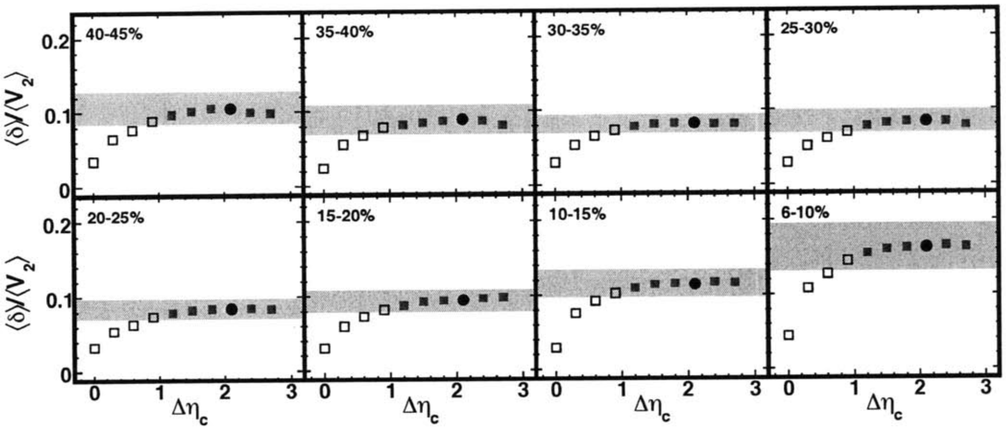

Figure 7.5: Measured value of the non-flow ratio, $\langle\delta\rangle \,/\, \langle\mathbf{V}_2\rangle$, as a function of the $\Delta\eta$ cut, $\Delta\eta_c$, where non-flow correlations are assumed to be zero at $|\Delta\eta| > \Delta\eta_c$ for different centrality bins. The black circles (one for each panel) show values for $\Delta\eta_c = 2.1$ with the gray band denoting the 90% C.L. systematic errors on those results as described in the text. The gray squares show values for $1.2 \leq \Delta\eta_c \leq 2.7$, which are used in the systematic error estimation. Open squares show values for $\Delta\eta_c < 1$.

the complete analysis chain has been performed by dividing the data set into 6×2cm wide vertex bins. Systematic errors are estimated for different steps in the analysis using the variation in the results with respect to the baseline due to these changes in the analysis. The errors in the different steps are added in quadrature to obtain the 90% confidence interval on the measurement of non-flow ratio.

7.4 Correlations at Large $\Delta\eta$ Separations

The success of the non-flow correlation measurement on ICM events, demonstrated in Chapter 5, relies on the fact that non-flow correlations are short-ranged in the model. It is not a priori known that the same should be true in real data. As discussed in Chapter 3, a rich correlation structure in high p_{T}-triggered correlations that extend out to $|\Delta\eta| > 2$ has been observed in 200 GeV Au+Au collision at RHIC after the estimated elliptic flow signal is subtracted [36]. Studies of similar correlation structures in the AMPT model suggest that this rich correlation structure is mainly due to triangular flow and does not necessarily indicate a large non-flow signal. However, measurements of the correlation function in p+p collisions show that non-flow correlations do extend out to $|\Delta\eta| > 2$ in elementary collisions [94]. Therefore, it is important to evaluate the possible effect of non-flow at $|\Delta\eta| > 2$ on the non-flow ratio results quantitatively.

The study of the non-flow ratio as a function of the $\Delta\eta$ cut ($\Delta\eta_c$) for the $v_2(\eta)^{\mathrm{fit}}$ fit carries important information on the magnitude of non-flow at large $\Delta\eta$ separations. If non-flow correlations are short ranged, it is expected that the fits should yield

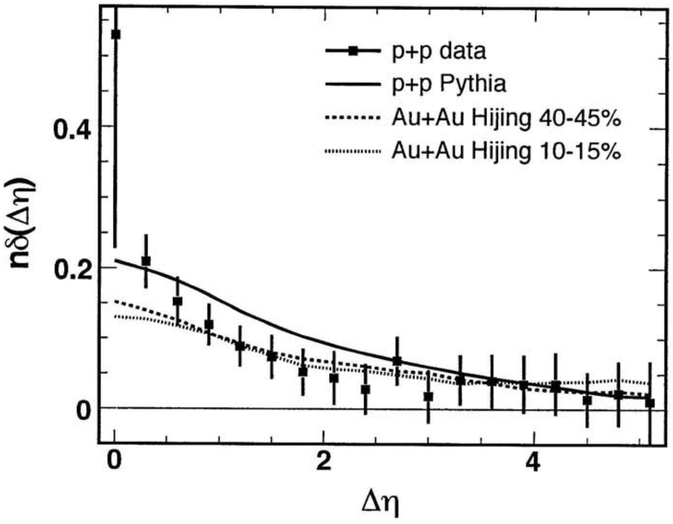

Figure 7.6: The magnitude of non-flow correlations, δ, scaled by the charged particle multiplicity, n, in the pseudorapidity range $|\eta| < 3$ as a function of particle pair pseudorapidity separations, $\Delta\eta$, for p+p data and different Monte Carlo generators with no flow correlations at $\sqrt{s_{\rm NN}} = 200$ GeV. The results for p+p data (squares) with 90% C.L. systematic errors are obtained from two-particle $\Delta\eta, \Delta\phi$ correlations [94]. Statistical errors are not shown.

non-flow ratio results that saturate for large values of $\Delta\eta_c$. The extracted value of $\langle\delta\rangle / \langle \mathbf{V}_2\rangle$ is plotted as a function of the $\Delta\eta_c$, where it is assumed that δ is zero for $|\Delta\eta| > \Delta\eta_c$, for different centrality bins in Fig. 7.5. The saturation expected if non-flow correlations are short-range is indeed observed. However, it should be noted that the same saturation pattern could also be observed with a finite magnitude of non-flow that has little $\Delta\eta$ dependence in the region $\Delta\eta > 1.2$.

To quantitatively assess the effect of non-zero non-flow correlations at large $\Delta\eta$ separations, the correlation functions obtained from Monte Carlo event generators are analyzed. In p+p collisions, the magnitude of non-flow correlations, δ, can be directly calculated as the second Fourier coefficient of $\Delta\phi$ correlations since elliptic flow is not present [94]. If A+A collisions were a superposition of p+p collisions, the value of δ would be diluted due to the presence of uncorrelated particles. To compare the strength of non-flow correlations in HIJING (Au+Au) and PYTHIA (p+p) models and p+p collisions, the value of δ scaled by the average event multiplicity is calculated. As shown in Fig. 7.6[5], both models are observed to roughly reproduce the strength of non-flow correlations in p+p collisions at large $\Delta\eta$. Due to large systematic uncertainties in the p+p data, HIJING simulations are used to model the long range non-flow correlations in Au+Au collisions by assuming non-flow correlations

---

[5] The large uncertainty in the p+p data at $\Delta\eta = 0$ is due to δ-electrons and γ conversions, which may not be completely described by GEANT simulations [94].

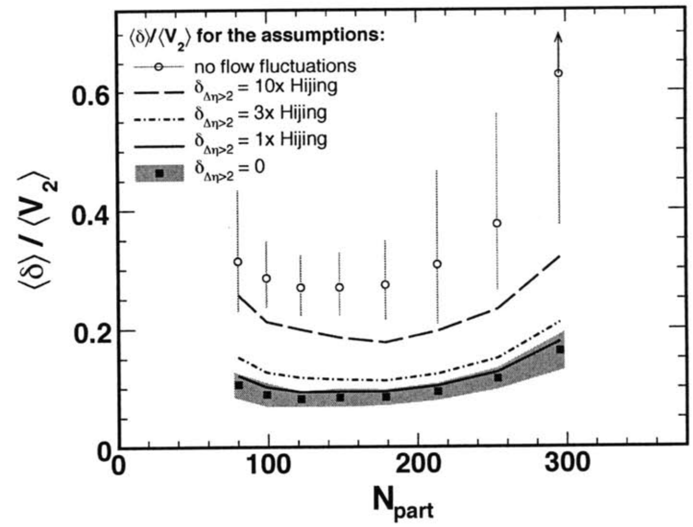

Figure 7.7: The non-flow ratio, $\langle\delta\rangle / \langle\mathbf{V}_2\rangle$, as a function of number of participating nucleons, N_{part}. The black squares show the results with the assumption that non-flow correlations are negligible at $|\Delta\eta| > 2$. The shaded band shows the 90% C.L. systematic errors. The lines show different assumptions about non-flow at $|\Delta\eta| > 2$. The open circles with 90% C.L. systematic errors, show the upper limit on $\langle\delta\rangle / \langle\mathbf{V}_2\rangle$ obtained by assuming that the measured dynamic fluctuations in v_2 are due to non-flow alone.

in data are some multiplicative factor, m, times the non-flow in HIJING, $\delta_{\text{MC}}(\eta_1, \eta_2)$, for $|\Delta\eta| > 2$. This can be incorporated by modifying Eq. 5.11:

$$\mathbf{V}_2(\eta_1, \eta_2) - m\delta_{\text{MC}}(\eta_1, \eta_2) = v_2(\eta_1)^{\text{fit}} \times v_2(\eta_2)^{\text{fit}}\ ;\ |\Delta\eta| > 2. \tag{7.3}$$

7.5 Non-flow Ratio Results

The resulting non-flow ratio, $\langle\delta\rangle / \langle\mathbf{V}_2\rangle$, found by applying Eqs. 5.12-5.14 with the modified $v_2(\eta)^{\text{fit}}$ results, is plotted as a function of centrality in Fig. 7.7 for different assumptions on the magnitude of non-flow at $|\Delta\eta| > 2$. If non-flow correlations are assumed to be present only in $|\Delta\eta| < 2$ ($m = 0$), it is found that they account for approximately 10% of the observed $\mathbf{V}_2$ signal averaged over $|\eta| < 3$. The results do not change significantly if the long range non-flow correlations ($\delta_{|\Delta\eta|>2}$) are taken to be the same as the correlations in HIJING ($m = 1$ instead of $m = 0$).

The upper limit on the non-flow ratio, also shown in Fig. 7.7, is drawn from the measurement of dynamic v_2 fluctuations assuming that the observed fluctuations are solely due to non-flow correlations. The calculation of this limit is described in Appendix C. The limit corresponds to non-flow correlations in Au+Au collisions that

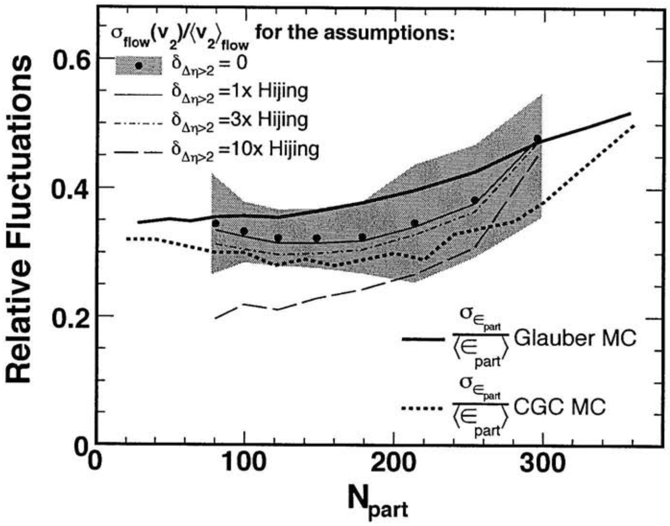

Figure 7.8: Elliptic flow fluctuations, $\sigma_{\text{flow}}/\left<v_2\right>_{\text{flow}}$, as a function of number of participating nucleons, N_{part}, for Au+Au collisions at $\sqrt{s_{\text{NN}}} = 200$ GeV. The black circles show the results with the assumption that non-flow correlations are negligible at $|\Delta\eta| > 2$. The shaded band shows the 90% confidence systematic errors. The thin lines show results for different assumptions on the magnitude of non-flow at $|\Delta\eta|>2$. The continuous and dashed thick lines show $\sigma(\epsilon_{part})/\langle\epsilon_{part}\rangle$ values calculated in Glauber MC and CGC [91] models, respectively.

are more than an order of magnitude higher than the expected correlations from p+p collisions for $|\Delta\eta|>2$ ($m > 10$).

7.6 Elliptic Flow Fluctuation Results

The measured values of relative dynamic v_2 fluctuations and non-flow ratio can be used to determine elliptic flow fluctuations as described in Sect. 5.3. The systematic error in the magnitude of relative elliptic flow fluctuations is obtained by propagating the errors in the measured quantities $\sigma_{\text{dyn}}/\left<v_2\right>$ and $\left<\delta\right>/\left<\mathbf{V}_2\right>$ and by varying the procedure to calculate $\sigma_{\text{flow}}/\left<v_2\right>_{\text{flow}}$ from these quantities. The errors from different sources are added in quadrature to obtain the 90% confidence interval. The error propagated from the uncertainty in $\sigma_{\text{dyn}}/\left<v_2\right>$ is the dominant contribution to the uncertainty in $\sigma_{\text{flow}}/\left<v_2\right>_{\text{flow}}$.

The relative fluctuations in the event-by-event elliptic flow, corrected for contribution of non-flow correlations are presented in Fig. 7.8 as a function of the number of participating nucleons in Au+Au collisions at $\sqrt{s_{\text{NN}}} = 200$ GeV for 6–45% most central events. The elliptic flow fluctuations are found to be roughly 30–40% if the magnitude of non-flow correlations are assumed to be small for $|\Delta\eta|>2$. Also shown in Fig. 7.8 are relative fluctuations in the participant eccentricity obtained from MC

Glauber and CGC [91] calculations. The measured values of elliptic flow fluctuations are observed to be consistent with both models over the centrality range under study if the long range non-flow correlations are neglected. The same conclusion holds if the long range correlations are assumed to be three times stronger than in p+p collisions, as modeled by HIJING.

8 Conclusion

The significantly large values of elliptic flow in Cu+Cu collisions lead to the proposition that initial geometry fluctuations may be crucial in understanding the dynamics of heavy ion collisions. Two studies have been presented in this thesis in the context of these fluctuations:

1. It has been proposed that previously unexplained ridge and broad away side features in azimuthal two-particle correlations may be understood as being due to the next order anisotropy in the initial collision geometry, i.e. participant triangularity. It has been demonstrated that event-by-event fluctuations lead to a finite triangularity value in Glauber Monte Carlo events and that this triangular anisotropy in the initial geometry leads to a triangular anisotropy in particle production in the AMPT model. The third Fourier coefficient of azimuthal correlations at large pseudorapidity separations have been found to be dominated by triangular flow in the model. The ratio of the third and second Fourier coefficients of azimuthal correlations in experimental data and the AMPT model has been studied as a function of centrality, pseudorapidity range and trigger particle momentum. A qualitative agreement between the data and the model has been observed.

2. Results have been presented on relative fluctuations in event-by-event elliptic flow for Au+Au collisions at $\sqrt{s_{\rm NN}} = 200$ GeV as a function of centrality. Large relative fluctuations of approximately 30-40% have been observed. The magnitude of relative fluctuations has been found to be consistent with predictions based on initial geometry fluctuations.

A unified picture of the collective dynamics of heavy ion collisions emerges from these studies. The collision of ultrarelativistic heavy ions starts as a quantum mechanical "measurement" of the positions of nucleons in the nuclei. The energy density distribution in the early stages of the collision is determined by this initial measurement. The fluctuations in the positions of nucleons for different events lead to an anisotropic energy density distribution even for the most central collisions. The dominant anisotropy is in the second Fourier coefficient of transverse nucleon distributions with respect to the center of mass of the overlap region, i.e. eccentricity. A significantly large anisotropy is also observed in the third Fourier coefficient of transverse nucleon distributions, defined as triangularity. The anisotropy in the initial energy density translates to a final state anisotropy event-by-event through collective flow of the produced medium.

This emerging picture, as well as the methodology developed in this thesis may have important implications in the future studies of collective flow and two-particle correlations in heavy ion collisions.

1. This study suggests that the values of elliptic flow scaled by eccentricity, v_2/ε_2, have been over-estimated in previous studies which did not account for initial geometry fluctuations. a) The value of ε_2 calculated with respect to the reaction plane is smaller than the actual eccentricity of the system created in the early stages of heavy ion collisions. b) Experimental measurements of elliptic flow are sensitive to the RMS of v_2, $\sqrt{\langle v_2\rangle^2}$, which is approximately 10% higher than $\langle v_2\rangle$.

2. Triangular flow has a different dependence on transverse momentum, centrality and pseudorapidity in comparison to elliptic flow in both the AMPT model and experimental data. Differential and comparative studies of triangular flow as a function of these parameters may provide new information on the initial conditions of heavy ion collisions and the subsequent collective expansion of the system.

3. Experimental measurements of collective flow and two-particle correlations are highly convoluted. Many different approaches have been taken to reduce non-flow effects in flow measurements and to subtract elliptic flow contribution to two-particle correlations. This convolution presents the biggest uncertainties in the experimental determination of both observables. A number of observations made in this thesis suggest that non-flow correlations are small at large pseudorapidity separations. Therefore, the best approach to untangle the two types of correlations may be achieved by a systematic study of their pseudorapidity dependence with large acceptance detectors, similar to the measurement of non-flow correlations presented in this thesis.

A Kinematic Variables

A right-handed coordinate system, where the z axis points in the beam direction, is used to parameterize kinematic variables. Different conventions are used to define the transverse coordinates x and y. In the description of initial collision geometry, x axis points in the direction of the impact parameter. The PHOBOS geometry is described with the x and y axes parallel and perpendicular to the ground, respectively. The azimuthal angle is given by ϕ. The azimuthal separation between two particles is given by $\Delta\phi$. The projection of the momentum of a particles to the transverse plane, i.e. transverse momentum, is given by p_{T}.

In high-energy physics, it is customary to parametrize the longitudinal axis in terms of the rapidity variable, y:

$$\begin{aligned} y &= \frac{1}{2}\ln\left(\frac{E+p_z}{E-p_z}\right). \\ &= \frac{1}{2}\ln\left(\frac{1+\beta}{1-\beta}\right). \end{aligned} \tag{A.1}$$

The rapidity variable is additive under Lorentz transformation. In this sense, rapidity in relativistic mechanics is analogous to velocity in non-relativistic mechanics, where velocity is additive under Galilean transformations. In experimental situations where the momentum or identity of a particle is unknown, it is convenient to approximate rapidity with pseudorapidity which can be determined based only on the polar angle θ:

$$y \approx \eta \equiv \ln\left(\tan(\theta/2)\right). \tag{A.2}$$

This is a good approximation in the high-energy limit where the particle mass is small compared to its momentum. The separation between two particles in pseudorapidity space is denoted by $\Delta\eta$.

B PHOBOS Collaboration List

B. Alver[4], B. B. Back[1], M. D. Baker[2], M. Ballintijn[4], D. S. Barton[2], R. R. Betts[6], R. Bindel[7], W. Busza[4], Z. Chai[2], V. Chetluru[6], E. García[6], T. Gburek[3], K. Gulbrandsen[4], J. Hamblen[8], I. Harnarine[6], C. Henderson[4], D. J. Hofman[6], R. S. Hollis[6], R. Hołyński[3], B. Holzman[2], A. Iordanova[6], J. L. Kane[4], P. Kulinich[4], C. M. Kuo[5], W. Li[4], W. T. Lin[5], C. Loizides[4], S. Manly[8], A. C. Mignerey[7], R. Nouicer[2], A. Olszewski[3], R. Pak[2], C. Reed[4], E. Richardson[7], C. Roland[4], G. Roland[4], J. Sagerer[6], I. Sedykh[2], C. E. Smith[6], M. A. Stankiewicz[2], P. Steinberg[2], G. S. F. Stephans[4], A. Sukhanov[2], A. Szostak[2], M. B. Tonjes[7], A. Trzupek[3], G. J. van Nieuwenhuizen[4], S. S. Vaurynovich[4], R. Verdier[4], G. I. Veres[4], P. Walters[8], E. Wenger[4], D. Willhelm[7], F. L. H. Wolfs[8], B. Wosiek[3], K. Woźniak[3], S. Wyngaardt[2], B. Wysłouch[4]

[1] Argonne National Laboratory, Argonne, IL 60439-4843, USA
[2] Brookhaven National Laboratory, Upton, NY 11973-5000, USA
[3] Institute of Nuclear Physics PAN, Kraków, Poland
[4] Massachusetts Institute of Technology, Cambridge, MA 02139-4307, USA
[5] National Central University, Chung-Li, Taiwan
[6] University of Illinois at Chicago, Chicago, IL 60607-7059, USA
[7] University of Maryland, College Park, MD 20742, USA
[8] University of Rochester, Rochester, NY 14627, USA

C Relations between Elliptic Flow, Fluctuations and Two-Particle Correlations

In this section, various useful relations between elliptic flow, elliptic flow fluctuations and two particles correlations are derived.

C.1 Event-by-event Distributions

Independent Particle Production with Constant Flow

Consider an event with n particles where each particle is independently produced with a random azimuthal direction selected from a distribution $1 + 2v_2 \cos(2\phi)$. Define direction vector $\vec{q}$ for each particle with unit length:

$$q_x \equiv \cos(2\phi), \tag{C.1}$$

$$q_y \equiv \sin(2\phi). \tag{C.2}$$

Summing the direction vectors for all particles in the given event, the event-by-event $\vec{Q}$ vector is constructed as [51]:

$$\vec{Q} \equiv \sum_i^n \vec{q_i}. \tag{C.3}$$

Mathematically, the $\vec{Q}$ vector can be thought of as the result of a two-dimensional random walk with n steps. For large n, central limit theorem dictates that Q_x and Q_y will be distributed with Gaussian distributions:

$$p(Q_x) = \frac{1}{\sqrt{2\pi}\sigma_{Qn}} \exp\left(-\frac{(Q_x - nv_2)^2}{2\sigma_{Qn}^2}\right) \tag{C.4}$$

$$p(Q_y) = \frac{1}{\sqrt{2\pi}\sigma_{Qn}} \exp\left(-\frac{Q_y^2}{2\sigma_{Qn}^2}\right), \tag{C.5}$$

where $\sigma_{Qn} = \sqrt{n/2}$.

In the distribution of the $\vec{Q}$ vector, v_2 appears with a scale factor of the multiplicity n. It is customary to take out this dependence by defining $\vec{r} \equiv \vec{Q}/n$.

$$p(r_x) = \frac{1}{\sqrt{2\pi}\sigma_n} \exp\left(-\frac{(r_x - v_2)^2}{2\sigma_n^2}\right) \tag{C.6}$$

$$p(r_y) = \frac{1}{\sqrt{2\pi}\sigma_n} \exp\left(-\frac{r_y^2}{2\sigma_n^2}\right), \tag{C.7}$$

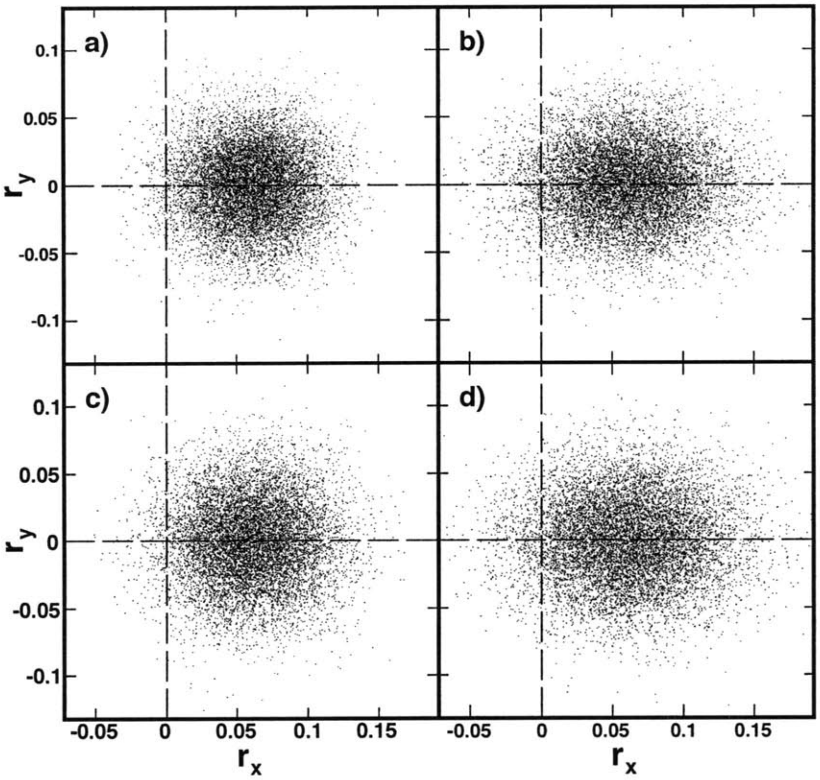

Figure C.1: Distribution of $\vec{r}$ vector for a set of Monte Carlo events with $\langle v_2 \rangle = 0.06$ and $\sigma_n = 0.028$. Figures a), b), c) and d) are for events with fluctuation and correlation magnitudes of $\sigma_{\text{flow}} = 0, \sigma_\delta = 0$; $\sigma_{\text{flow}} = 0.024, \sigma_\delta = 0$; $\sigma_{\text{flow}} = 0, \sigma_\delta = 0.014$ and $\sigma_{\text{flow}} = 0.024, \sigma_\delta = 0.014$ respectively.

where $\sigma_n = 1/\sqrt{2n}$. Distribution of the $\vec{r}$ vector for different samples of events with varying fluctuation and correlation magnitudes is shown in Fig. C.1.

In an experimental setup, the direction with respective to which flow builds up, ϕ_0[1], is unknown. However, the length of the $\vec{Q}$ vector can be measured since it does not depend

---

[1] The direction of the event-plane angle, ϕ_0, is expected to align with the reaction plane angle if the initial geometry of heavy ion collisions is defined by two smooth Wood-Saxon distributions or with the participant eccentricity axis if initial geometry fluctuations are indeed present. The derivations provided here are independent of the underlying microscopic picture.

on the selection of reaction plane angle:

$$
\begin{aligned}
Q^2 = \quad & \left(\sum_i^n \cos(2\phi_i - 2\phi_0)\right)^2 + \left(\sum_i^n \sin(2\phi_i - 2\phi_0)\right)^2 && \text{(C.8)} \\
= \; & \sum_{i,j}^n \Big(\cos(2\phi_i - 2\phi_0)\Big) \times \Big(\cos(2\phi_j - 2\phi_0)\Big) \\
& \quad + \Big(\sin(2\phi_i - 2\phi_0)\Big) \times \Big(\sin(2\phi_j - 2\phi_0)\Big) && \text{(C.9)} \\
= \; & \sum_{i,j}^n \Big(\cos(2\phi_i)\cos(2\phi_0) + \sin(2\phi_i)\sin(2\phi_0))\Big) \times \Big(\cos(2\phi_j)\cos(2\phi_0) + \sin(2\phi_j)\sin(2\phi_0))\Big) \\
& \quad + \Big(\sin(2\phi_i)\cos(2\phi_0) - \cos(2\phi_i)\sin(2\phi_0)\Big) \times \Big(\sin(2\phi_j)\cos(2\phi_0) - \cos(2\phi_j)\sin(2\phi_0)\Big) \\
& && \text{(C.10)} \\
= \; & \sum_{i,j}^n \cos^2(2\phi_0) \times \Big(\cos(2\phi_i)\cos(2\phi_j) + \sin(2\phi_i)\sin(2\phi_j)\Big) \\
& \quad + \cos(2\phi_0)\sin(2\phi_0) \times \Big(\cos(2\phi_i)\sin(2\phi_j) + \sin(2\phi_i)\cos(2\phi_j) \\
& \qquad\qquad - \sin(2\phi_i)\cos(2\phi_j) - \cos(2\phi_i)\sin(2\phi_j)\Big) \\
& \quad + \sin^2(2\phi_0) \times \Big(\sin(2\phi_i)\sin(2\phi_j) + \cos(2\phi_i)\cos(2\phi_j)\Big) && \text{(C.11)} \\
= \; & \sum_{i,j}^n \Big(\sin(2\phi_i)\sin(2\phi_j) + \cos(2\phi_i)\cos(2\phi_j)\Big). && \text{(C.12)}
\end{aligned}
$$

The distribution of the length of the $\vec{r}$ vector is given as:

$$
\begin{aligned}
p(r|v_2) &= \int_0^{\pi} \frac{\mathrm{d}\phi}{2\pi\sigma_n^2} \exp\left(\frac{-(r\cos(2\phi) - v_2)^2 - (r\sin(2\phi))^2}{2\sigma_n^2}\right) && \text{(C.13)} \\
&= \frac{1}{2\pi\sigma_n^2} \exp\left(-\frac{r^2 + v_2^2}{2\sigma_n^2}\right) \int_0^{2\pi} \mathrm{d}\phi \exp\left(\frac{r v_2 \cos(2\phi)}{\sigma_n^2}\right) && \text{(C.14)} \\
&= \frac{1}{\sigma_n^2} \exp\left(-\frac{r^2 + v_2^2}{2\sigma_n^2}\right) I_0\left(\frac{r v_2}{\sigma_n^2}\right), && \text{(C.15)}
\end{aligned}
$$

where I_0 is the modified Bessel function. This function is referred to as the Bessel-Gaussian distribution:

$$
\mathrm{BG}\left(r; v_2, \sigma_n\right) \equiv \frac{1}{\sigma_n^2} \exp\left(-\frac{r^2 + v_2^2}{2\sigma_n^2}\right) I_0\left(\frac{r v_2}{\sigma_n^2}\right), \qquad \text{(C.16)}
$$

The first two moments of this distribution are given as:

$$
\begin{aligned}
\langle r \rangle &= \frac{1}{2\sigma_n} \exp\left(\frac{-v_2^2}{4\sigma_n^2}\right) \sqrt{\frac{\pi}{2}} \left[(v_2^2 + 2\sigma_n^2) I_0\left(\frac{v_2^2}{4\sigma_n^2}\right) + v_2^2 I_1\left(\frac{v_2^2}{4\sigma_n^2}\right)\right] && \text{(C.17)} \\
\langle r^2 \rangle &= v_2^2 + 2\sigma_n^2 && \text{(C.18)}
\end{aligned}
$$

Non-flow Correlations

To first order, non-flow correlations can be assumed to be the same in all azimuthal directions independent of ϕ_0. Therefore non-flow correlations broaden the $\vec{Q}$ vector distribution in both the x and the y directions. The broadening caused by non-flow correlations can be quantified by a parameter σ_δ such that σ_n will effectively be replaced by $\sqrt{\sigma_n^2 + \sigma_\delta^2}$ leading to:

$$
\begin{aligned}
p(r_x|v_2, \sigma_\delta) &= \frac{1}{\sqrt{2\pi(\sigma_n^2 + \sigma_\delta^2)}} \exp\left(-\frac{(r_x - v_2)^2}{2(\sigma_n^2 + \sigma_\delta^2)}\right) && \text{(C.19)} \\
p(r_y|v_2, \sigma_\delta) &= \frac{1}{\sqrt{2\pi(\sigma_n^2 + \sigma_\delta^2)}} \exp\left(-\frac{r_y^2}{2(\sigma_n^2 + \sigma_\delta^2)}\right) && \text{(C.20)} \\
p(r|v_2, \sigma_\delta) &= \mathrm{BG}\left(r; v_2, \sqrt{\sigma_n^2 + \sigma_\delta^2}\right) && \text{(C.21)}
\end{aligned}
$$

Elliptic Flow Fluctuations

Consider a set of events where the magnitude of elliptic flow is not constant but fluctuates event-by-event. Assume Gaussian fluctuations with a mean of $\langle v_2 \rangle_{\mathrm{flow}}$ and standard deviations σ_{flow}. The fluctuations in elliptic flow will broaden the $\vec{Q}$ vector distribution only in the x direction leading to:

$$
\begin{aligned}
p(r_x| \langle v_2 \rangle_{\mathrm{flow}}, \sigma_\delta, \sigma_{\mathrm{flow}}) &= \frac{1}{\sqrt{2\pi(\sigma_n^2 + \sigma_\delta^2 + \sigma_{\mathrm{flow}}^2)}} \exp\left(-\frac{(r_x - \langle v_2 \rangle_{\mathrm{flow}})^2}{2(\sigma_n^2 + \sigma_\delta^2 + \sigma_{\mathrm{flow}}^2)}\right) && \text{(C.22)} \\
p(r_y| \langle v_2 \rangle_{\mathrm{flow}}, \sigma_\delta, \sigma_{\mathrm{flow}}) &= \frac{1}{\sqrt{2\pi(\sigma_n^2 + \sigma_\delta^2)}} \exp\left(-\frac{r_y^2}{2(\sigma_n^2 + \sigma_\delta^2)}\right) && \text{(C.23)} \\
p(r| \langle v_2 \rangle_{\mathrm{flow}}, \sigma_\delta, \sigma_{\mathrm{flow}}) &\propto \int_0^{2\pi} \exp\left(-\frac{(r\cos(2\phi) - \langle v_2 \rangle_{\mathrm{flow}})^2}{2(\sigma_n^2 + \sigma_\delta^2 + \sigma_{\mathrm{flow}}^2)} - \frac{(r\sin(2\phi))^2}{2(\sigma_n^2 + \sigma_\delta^2)}\right) \mathrm{d}\phi && \text{(C.24)}
\end{aligned}
$$

Dynamic v_2 Fluctuations

The distribution $p(r|v_2)$ given in Eq. C.15 can be thought of as the response function of a measurement where the input is the magnitude of elliptic flow, parametrized by v_2. Therefore, this distribution will be referred to as the kernel: $K_n(r, v_2) \equiv p(r|v_2)$. If the measured distribution of the event-by-event azimuthal anisotropy is given by $g(r)$, the dynamic fluctuations in v_2 can be expressed in terms of the underlying v_2 distribution, $f(v_2)$, as

$$g(r) = \int K_n(r, v_2) f(v_2) \mathrm{d}v_2. \tag{C.25}$$

It is important to note that $f(v_2)$ defined in this way incorporates fluctuations from both elliptic flow fluctuations and non-flow correlations. The dynamic fluctuations in v_2 can be estimated by performing a fit to the measured r distribution and known response function by assuming a functional form for $f(v_2)$ with two parameters mean $\langle v_2 \rangle$ and standard deviation σ_{dyn}.

For small values of $\sigma_{\text{flow}}/v_2 \lesssim 0.05$ and $\sigma_\delta/v_2 \lesssim 0.2$, the r distribution in Eq. C.24 can be approximated as:

$$p(r|v_2, \sigma_\delta, \sigma_{\text{flow}}) \approx \text{BG}\left(r; \sqrt{v_2^2 - \sigma_{\text{flow}}^2}, \sqrt{\sigma_n^2 + \sigma_\delta^2 + \sigma_{\text{flow}}^2}\right). \tag{C.26}$$

Therefore measurement of v_2 fluctuations using the kernel, $K_n(r, v_2) = p(r|v_2)$, from Eq. C.15 on a set of events with flow fluctuations and correlations, $g(r) = p(r|v_2, \sigma_\delta, \sigma_{\text{flow}})$ from Eq. C.24, approximately yields

$$\sigma_{\text{dyn}} \approx \sqrt{\sigma_\delta^2 + \sigma_{\text{flow}}^2}. \tag{C.27}$$

However, this approximation breaks down for higher values of σ_{flow}/v_2. Therefore, the calculation of elliptic flow fluctuations from measured dynamic fluctuations and non-flow correlations is performed numerically.

C.2 Two-Particle Correlations

In this section, the relation between elliptic flow and two-particle azimuthal correlations are derived.

Independent Particle Production

Again, it is useful to start by considering a scenario where the only correlation between particles is due to elliptic flow:

$$p(\phi) = \frac{1}{2\pi}\left\{1 + 2v_2(\eta)\cos(2(\phi - \phi_0))\right\}. \tag{C.28}$$

The probability to observe two particles from η_1 and η_2 with an azimuthal separation of $\Delta\phi$ is given as:

$$\begin{aligned}
p(\Delta\phi) &= \left(\frac{1}{4\pi}\right)^2 \int \left\{1 + 2v_2(\eta_1)\cos(2(\phi - \phi_0))\right\} && \text{(C.29)}\\
&\qquad \times \left\{1 + 2v_2(\eta_2)\cos(2(\phi + \Delta\phi - \phi_0))\right\} d\phi \\
&= \left(\frac{1}{4\pi}\right)^2 \int 1 + 2\left[v_2(\eta_1)\cos(2(\phi - \phi_0)) + v_2(\eta_2)\cos(2(\phi + \Delta\phi - \phi_0))\right] \\
&\qquad + 4\left[v_2(\eta_1) \times v_2(\eta_2)\right]\cos(2(\phi - \phi_0))\cos(2(\phi + \Delta\phi - \phi_0)) d\phi \\
&= \left(\frac{1}{4\pi}\right)^2 \int 1 + 2\left[v_2(\eta_1) \times v_2(\eta_2)\right]\left\{\cos(4\phi + 2\Delta\phi - 4\phi_0) + \cos(2\Delta\phi)\right\} d\phi \\
&= \frac{1}{2\pi}\left\{1 + 2\left[v_2(\eta_1) \times v_2(\eta_2)\right]\cos(2\Delta\phi)\right\}. && \text{(C.30)}
\end{aligned}$$

Therefore

$$\mathbf{V}_2^{\text{flow}}(\eta_1, \eta_2) = \langle\cos(2\Delta\phi)\rangle(\eta_1, \eta_2) = \langle v_2(\eta_1) \times v_2(\eta_2)\rangle. \tag{C.31}$$

Correlated Particle Production

Starting from Eq. C.12:

$$
\begin{aligned}
Q^2 &= \sum_{i,j}^{n} \Big(\sin(2\phi_i)\sin(2\phi_j) + \cos(2\phi_i)\cos(2\phi_j) \Big) && \text{(C.32)} \\
&= \sum_{i,j}^{n} \cos(2(\phi_i - \phi_j)) && \text{(C.33)} \\
&= \sum_{i}^{n} \cos(2(\phi_i - \phi_i)) + \sum_{i \neq j}^{n} \cos(2(\phi_i - \phi_j)) && \text{(C.34)} \\
&= n + \sum_{i \neq j}^{n} \cos(2(\phi_i - \phi_j)) && \text{(C.35)} \\
r^2 &= \frac{1}{n} + \overline{\cos(2(\phi_i - \phi_j))} && \text{(C.36)} \\
&= 2\sigma_n^2 + \overline{\cos(2\Delta\phi)}, && \text{(C.37)}
\end{aligned}
$$

where $\overline{x}$ refers to average over all particle pairs in an event.

Taking into account contribution from fluctuations and non-flow correlations Eq. C.18 reads:

$$\langle r^2 \rangle = \langle v_2 \rangle_{\text{flow}}^2 + \sigma_{\text{flow}}^2 + 2\sigma_n^2 + 2\sigma_\delta^2 \qquad \text{(C.38)}$$

Averaging Eq. C.37 over many events and comparing to Eq. C.38 yields

$$\langle \mathbf{V}_2 \rangle = \langle \cos(2\Delta\phi) \rangle = \langle v_2 \rangle_{\text{flow}}^2 + \sigma_{\text{flow}}^2 + 2\sigma_\delta^2. \qquad \text{(C.39)}$$

Therefore the contribution of non-flow correlations to two-particle correlations, δ, is related to the dynamic v_2 fluctuations measurement through:

$$\delta = 2\sigma_\delta^2. \qquad \text{(C.40)}$$

C.3 Numerical Calculation

Using the relations given above, numerical calculations are performed to relate the measured values of dynamic v_2 fluctuations ($\sigma_{\text{dyn}} / \langle v_2 \rangle$) and non-flow ratio ($\langle \delta \rangle / \langle \mathbf{V}_2 \rangle$) to intrinsic elliptic flow fluctuations ($\sigma_{\text{flow}} / \langle v_2 \rangle_{\text{flow}}$).

Assume the mean value of the elliptic flow distribution and the magnitude of statistical fluctuations to be given as $\langle v_2 \rangle_{\text{flow}} = 0.06$ and $\sigma_n = 0.6 \times \langle v_2 \rangle_{\text{flow}} = 0.036$. Then, for given values of $\sigma_{\text{flow}} / \langle v_2 \rangle_{\text{flow}}$ and $\langle \delta \rangle / \langle \mathbf{V}_2 \rangle$, the expected distribution of the observed event-by-event anisotropy r can be calculated as

$$g(r) = \int_0^1 K_{n,\delta}(r, v_2) f_{\text{flow}}(v_2) \mathrm{d}v_2, \qquad \text{(C.41)}$$

where $f_{\text{flow}}(v_2)$ is a Gaussian in the range $v_2 > 0$ with mean and standard deviation values given by $\langle v_2 \rangle_{\text{flow}}$ and σ_{flow}, respectively. The fluctuations encoded in the response function

$K_{n,\delta}(r, v_2)$ are given by $\sigma_n^2 + \sigma_\delta^2$, where σ_δ is calculated from $\langle v_2 \rangle_{\mathrm{flow}}$, σ_{flow} and $\langle \delta \rangle / \langle \mathbf{V}_2 \rangle$:

$$\begin{aligned} 2\sigma_\delta^2 &= \langle \delta \rangle && \text{(C.42)} \\ &= \langle \delta \rangle \times \frac{\langle v_2 \rangle_{\mathrm{flow}}^2 + \sigma_{\mathrm{flow}}^2}{\langle \mathbf{V}_2 \rangle - \langle \delta \rangle} && \text{(C.43)} \\ &= \frac{\langle \delta \rangle / \langle \mathbf{V}_2 \rangle}{1 - \langle \delta \rangle / \langle \mathbf{V}_2 \rangle} \times (\langle v_2 \rangle_{\mathrm{flow}}^2 + \sigma_{\mathrm{flow}}^2). && \text{(C.44)} \end{aligned}$$

Assuming the dynamic v_2 fluctuations are described by a Gaussian, $f_{\mathrm{dyn}}(v_2)$, in the range $v_2 > 0$ with mean and standard deviation values given by $\langle v_2 \rangle$ and σ_{dyn}, the value of $\sigma_{\mathrm{dyn}} / \langle v_2 \rangle$ can be obtained by fitting Eq. C.25. The resulting distribution of $\sigma_{\mathrm{dyn}} / \langle v_2 \rangle$ as a function of $\sigma_{\mathrm{flow}} / \langle v_2 \rangle_{\mathrm{flow}}$ and $\langle \delta \rangle / \langle \mathbf{V}_2 \rangle$ is shown in Fig. 5.5. The value of $\sigma_{\mathrm{flow}} / \langle v_2 \rangle_{\mathrm{flow}}$ corresponding to measured values of $\sigma_{\mathrm{dyn}} / \langle v_2 \rangle$ and $\langle \delta \rangle / \langle \mathbf{V}_2 \rangle$ can be extracted from this distribution. Furthermore, the values for $\sigma_{\mathrm{flow}} / \langle v_2 \rangle_{\mathrm{flow}} = 0$ can be used to set an upper limit on the magnitude of the non-flow ratio.

Since the related quantities are given as ratios, the value of $\langle v_2 \rangle_{\mathrm{flow}}$ set at the beginning is arbitrary. It was observed that $\sigma_n / \langle v_2 \rangle$ is roughly given by 0.6 for the dynamic v_2 fluctuations measurement for all centrality bins in the centrality range studied. The calculation was repeated for values of $\sigma_n / \langle v_2 \rangle_{\mathrm{flow}}$=0.4 and 0.8. The differences in results, which were found to be small, are incorporated in the final systematic errors on elliptic flow fluctuations.

D Independent Cluster Model Monte Carlo

The idea that hadrons are produced in clusters, rather than individually, has had great success in describing many features of multi-particle production in high energy hadronic collisions (see e.g. [95]). In a scenario of independent cluster emission, clusters are formed before the final-state hadrons and are independently emitted according to a dynamically generated distribution in η and ϕ. The clusters subsequently decay isotropically in their own rest frame into the observed final-state hadrons. The postulate of independent emission of isotropic clusters has been widely applied to characterize the short-range properties of inclusive two-particle correlations [95].

A Monte Carlo event generator has been developed on the concept of Independent Cluster Model (ICM) as a testing ground for the analyses presented in this thesis. In this Monte Carlo approach, an event consists of a number of clusters, each generated with a given mass, transverse momentum (p_{T}), azimuthal direction (ϕ) and longitudinal momentum (p_{z}). The clusters decay isotropically in their rest frame into K particles (assumed to be pions) constrained by the available phase space, where the number of particles, K, is referred to as the cluster size.

This approach provides easily tunable event generation with dials for elliptic flow, flow fluctuations and non-flow correlations as well as multiplicity. Flow is introduced by choosing the ϕ direction of clusters randomly from an anisotropic probability distribution. Flow fluctuations are included by generating a sample of events with varying flow magnitude. By selecting only one particle from each cluster to construct events, the non-flow correlations can be destroyed while the one-particle distributions are preserved.

The non-flow correlation structure is determined by setting the values of cluster size, cluster mass and the p_{T} distribution. It is possible to set global momentum conservation by shifting the event to the global center of mass after all clusters are produced. The cluster p_{z} distribution is tuned for each cluster type to reproduce the $\mathrm{d}N/\mathrm{d}\eta$ distribution in data.

The ICM has been used with a wide range of parameters to study the measurement technique described in this thesis. Following model properties have been used for the figures in this thesis:

- Cluster size and mass are given by $K = 3$ and $M = 1.8$ GeV.
- The magnitude of flow is set such that when a flow fluctuations measurement with a triangular $v_2(\eta)$ ansatz is made, the average peak value is given as $\nu_2 = 0.068$.
- The total multiplicity of the events is 1200. These numbers match 40-45% most central data, which is the most peripheral bin used in the analyses.
- The p_{T} of clusters is selected randomly from a distribution given by $p_{\mathrm{T}} \times \exp(-p_{\mathrm{T}}/0.45)$.

E List of Acronyms

Facilities:

AGS Alternating Gradient Synchrotron (http://www.bnl.gov/bnlweb/facilities/AGS.asp)

BNL Brookhaven National Laboratory (http://www.bnl.gov/)

CERN European Organization for Nuclear Research – *Conseil Européen pour la Recherche Nucléaire* (http://public.web.cern.ch/public/)

LHC Large Hadron Collider (http://lhc.web.cern.ch/lhc/)

RHIC Relativistic Heavy Ion Collider (http://www.bnl.gov/RHIC/)

SPS Super Proton Synchrotron (http://ab-dep-op-sps.web.cern.ch/ab-dep-op-sps/)

Physics Terminology:

CGC Color Glass Condensate

QCD Quantum Chromodynamics

QED Quantum Electrodynamics

QGP Quark Gluon Plasma

PHOBOS and RHIC Hardware:

ADC Analog-to-Digital Converter

DAQ Data Acquisition

ONO Oxide-Nitrous-Oxide

PMT Photomultiplier Tube

T0 Time-Zero Counter

ZDC Zero-Degree Calorimeter

Experimental Terminology:

MinBias Minimum Bias

MIP Minimum Ionizing Particle

PdlMean Paddle Mean

PdlTDiff Paddle Time Difference

PDF Probability density function

LF likelihood function

Monte Carlo Event Generators:

HIJING Heavy Ion Jet Interaction Generator

AMPT A Multi-Phase Transport model

ICM Independent Cluster Model

Bibliography

[1] E. Wenger. *Studies of High Transverse Momentum Phenomena in Heavy Ion Collisions Using the PHOBOS Detector.* PhD thesis, Massachusetts Institute of Technology, 2008.

[2] Z. Fodor and S. D. Katz. Critical point of QCD at finite T and mu, lattice results for physical quark masses. *JHEP*, 04:050, 2004. [arXiv:hep-lat/0402006].

[3] Frithjof Karsch. Lattice QCD at high temperature and density. *Lect. Notes Phys.*, 583:209–249, 2002. [arXiv:hep-lat/0106019].

[4] S. S. Gubser, Igor R. Klebanov, and A. W. Peet. Entropy and Temperature of Black 3-Branes. *Phys. Rev.*, D54:3915–3919, 1996. [arXiv:hep-th/9602135].

[5] Hong Liu, Krishna Rajagopal, and Yeming Shi. Robustness and Infrared Sensitivity of Various Observables in the Application of AdS/CFT to Heavy Ion Collisions. *JHEP*, 08:048, 2008. [arXiv:0803.3214].

[6] Mark G. Alford, Andreas Schmitt, Krishna Rajagopal, and Thomas Schafer. Color superconductivity in dense quark matter. *Rev. Mod. Phys.*, 80:1455–1515, 2008. doi: 10.1103/RevModPhys.80.1455. [arXiv:0709.4635].

[7] Dany Page and Sanjay Reddy. Dense Matter in Compact Stars: Theoretical Developments and Observational Constraints. *Ann. Rev. Nucl. Part. Sci.*, 56: 327–374, 2006. [arXiv:astro-ph/0608360].

[8] K. Splittorff. The sign problem in the epsilon-regime of QCD. *PoS*, LAT2006: 023, 2006. [arXiv:hep-lat/0610072].

[9] Philippe de Forcrand and Owe Philipsen. The chiral critical line of N(f) = 2+1 QCD at zero and non-zero baryon density. *JHEP*, 01:077, 2007. [arXiv:hep-lat/0607017].

[10] Christof Roland. Particle ratio fluctuations in NA49. *PoS*, CFRNC2006:012, 2006.

[11] Mikhail A. Stephanov. QCD phase diagram and the critical point. *Prog. Theor. Phys. Suppl.*, 153:139–156, 2004. [arXiv:hep-ph/0402115].

[12] Reinhard Stock. The QCD Phase Diagram: Expectations and Challenges. 2009. [arXiv:0909.0601].

[13] Stephen Scott Adler et al. Centrality dependence of direct photon production in $\sqrt{s_{\mathrm{NN}}} = 200$ GeV Au + Au collisions. *Phys. Rev. Lett.*, 94:232301, 2005. [arXiv:nucl-ex/0503003].

[14] B. B. Back et al. Centrality and energy dependence of charged-particle multiplicities in heavy ion collisions in the context of elementary reactions. *Phys. Rev.*, C74:021902, 2006. [arXiv:nucl-ex/0301017].

[15] Paul Richard Sorensen. *Kaon and Lambda production at intermediate p(T): Insights into the hadronization of the bulk partonic matter created in Au + Au collisions at RHIC.* PhD thesis, University of California, Los Angeles, 2003. [arXiv:nucl-ex/0309003].

[16] Peter F. Kolb and Ulrich W. Heinz. Hydrodynamic description of ultrarelativistic heavy-ion collisions. 2003. [arXiv:nucl-th/0305084].

[17] B. B. Back et al. The PHOBOS perspective on discoveries at RHIC. *Nucl. Phys.*, A757:28–101, 2005. [arXiv:nucl-ex/0410022].

[18] Derek Teaney. Effect of shear viscosity on spectra, elliptic flow, and Hanbury Brown-Twiss radii. *Phys. Rev.*, C68:034913, 2003. [arXiv:nucl-th/0301099].

[19] S. Afanasiev et al. Elliptic flow for ϕ mesons and (anti)deuterons in Au+Au collisions at $\sqrt{s_{\mathrm{NN}}} = 200$ GeV. *Phys. Rev. Lett.*, 99:052301, 2007. [arXiv:nucl-ex/0703024].

[20] B. B. Back et al. Charged hadron transverse momentum distributions in Au + Au collisions at $\sqrt{s_{\mathrm{NN}}} = 200$ GeV. *Phys. Lett.*, B578:297–303, 2004. [arXiv:nucl-ex/0302015].

[21] Stephen Scott Adler et al. High-p(T) charged hadron suppression in Au + Au collisions at $\sqrt{s_{\mathrm{NN}}} = 200$ GeV. *Phys. Rev.*, C69:034910, 2004. [arXiv:nucl-ex/0308006].

[22] John Adams et al. Transverse momentum and collision energy dependence of high p(T) hadron suppression in Au + Au collisions at ultrarelativistic energies. *Phys. Rev. Lett.*, 91:172302, 2003. [arXiv:nucl-ex/0305015].

[23] John Adams et al. Experimental and theoretical challenges in the search for the quark gluon plasma: The STAR collaboration's critical assessment of the evidence from RHIC collisions. *Nucl. Phys.*, A757:102–183, 2005. [arXiv:nucl-ex/0501009].

[24] C. Adler et al. Disappearance of back-to-back high p_T hadron correlations in central Au+Au collisions at $\sqrt{s_{\mathrm{NN}}} = 200$ GeV. *Phys. Rev. Lett.*, 90:082302, 2003. [arXiv:nucl-ex/0210033].

[25] A. Andronic, P. Braun-Munzinger, and J. Stachel. Hadron production in central nucleus nucleus collisions at chemical freeze-out. *Nucl. Phys.*, A772:167–199, 2006. [arXiv:nucl-th/0511071].

[26] Ekkard Schnedermann, Josef Sollfrank, and Ulrich W. Heinz. Thermal phenomenology of hadrons from 200-A/GeV S+S collisions. *Phys. Rev.*, C48:2462–2475, 1993. [arXiv:nucl-th/9307020].

[27] B. Alver et al. Energy and centrality dependence of particle production at very low transverse momenta in Au+Au collisions. *J. Phys.*, G35:104131, 2008. [arXiv:0804.4270].

[28] Stephen Scott Adler et al. Systematic studies of the centrality and $\sqrt{s_{\rm NN}}$ dependence of dE(T)/d mu and d N(ch)/d mu in heavy ion collisions at mid-rapidity. *Phys. Rev.*, C71:034908, 2005. [arXiv:nucl-ex/0409015].

[29] Paul Stankus, (ed.), David Silvermyr, (ed.), Soren Sorensen, (ed.), and Victoria Greene, (ed.). Ultrarelativistic nucleus nucleus collisions. Proceedings, 21st International Conference, Quark matter, Knoxville, USA, March 30-April 4, 2009.

[30] (ed.) Ma, Yu-Gang et al. Ultra-relativistic nucleus-nucleus collisions. Proceedings, 19th International Conference, Quark Matter 2006, Shanghai, P.R. China, November 14-20, 2006. Prepared for 19th International Conference on Ultra-Relativistic Nucleus-Nucleus Collisions: Quark Matter 2006 (QM2006), Shanghai, China, 14-20 Nov 2006.

[31] (ed.) Csörgő, T., (ed.) Lévai, P., (ed.) David, G., and (ed.) Papp, G. Quark matter. Proceedings, 18th International Conference on Ultra-Relativistic Nucleus-Nucleus Collisions, QM'05, Budapest, Hungary, August 4-9, 2005. Prepared for 18th International Conference on Ultrarelativistic Nucleus-Nucleus Collisions: Quark Matter 2005 (QM 2005), Budapest, Hungary, 4-9 Aug 2005.

[32] (ed.) Ritter, H. G. and (ed.) Wang, X. N. Ultra-relativistic nucleus-nucleus collisions. Proceedings, 17th International Conference, Quark Matter 2004, Oakland, USA, January 11-17, 2004. Prepared for 17th International Conference on Ultra Relativistic Nucleus-Nucleus Collisions (Quark Matter 2004), Oakland, California, 11-17 Jan 2004.

[33] K. Adcox et al. Formation of dense partonic matter in relativistic nucleus nucleus collisions at RHIC: Experimental evaluation by the PHENIX collaboration. *Nucl. Phys.*, A757:184–283, 2005. [arXiv:nucl-ex/0410003].

[34] I. Arsene et al. Quark gluon plasma and color glass condensate at RHIC? The perspective from the BRAHMS experiment. *Nucl. Phys.*, A757:1–27, 2005. [arXiv:nucl-ex/0410020].

[35] B. Alver et al. System size, energy, pseudorapidity, and centrality dependence of elliptic flow. *Phys. Rev. Lett.*, 98:242302, 2007. [arXiv:nucl-ex/0610037].

[36] B. Alver et al. High transverse momentum triggered correlations over a large pseudorapidity acceptance in Au+Au collisions at $\sqrt{s_{\mathrm{NN}}} = 200$ GeV. *Phys. Rev. Lett.*, 104:062301, 2010. [arXiv:0903.2811].

[37] John Adams et al. Distributions of charged hadrons associated with high transverse momentum particles in p p and Au + Au collisions at $\sqrt{s_{\mathrm{NN}}} = 200$ GeV. *Phys. Rev. Lett.*, 95:152301, 2005. [arXiv:nucl-ex/0501016].

[38] A. Adare et al. Transverse momentum and centrality dependence of dihadron correlations in Au+Au collisions at $\sqrt{s_{\mathrm{NN}}} = 200$ GeV: Jet-quenching and the response of partonic matter. *Phys. Rev.*, C77:011901, 2008. [arXiv:0705.3238].

[39] B. I. Abelev et al. Long range rapidity correlations and jet production in high energy nuclear collisions. *Phys. Rev.*, C80:064912, 2009. [arXiv:0909.0191].

[40] A. Adare et al. Dihadron azimuthal correlations in Au+Au collisions at $\sqrt{s_{\mathrm{NN}}} = 200$ GeV. *Phys. Rev.*, C78:014901, 2008. [arXiv:0801.4545].

[41] B. I. Abelev et al. Indications of Conical Emission of Charged Hadrons at RHIC. *Phys. Rev. Lett.*, 102:052302, 2009. [arXiv:0805.0622].

[42] Cheuk-Yin Wong. The Momentum Kick Model Description of the Near-Side Ridge and Jet Quenching. *Phys. Rev.*, C78:064905, 2008. [arXiv:0806.2154].

[43] V. S. Pantuev. "Jet-Ridge" effect in heavy ion collisions as a back splash from stopped parton. 2007. [arXiv:0710.1882].

[44] Sean Gavin, Larry McLerran, and George Moschelli. Long Range Correlations and the Soft Ridge in Relativistic Nuclear Collisions. *Phys. Rev.*, C79:051902, 2009. doi: 10.1103/PhysRevC.79.051902. [arXiv:0806.4718].

[45] Adrian Dumitru, Francois Gelis, Larry McLerran, and Raju Venugopalan. Glasma flux tubes and the near side ridge phenomenon at RHIC. *Nucl. Phys.*, A810:91, 2008. doi: 10.1016/j.nuclphysa.2008.06.012. [arXiv:0804.3858].

[46] Jorg Ruppert and Thorsten Renk. Mach cone shock waves at RHIC. *Acta Phys. Polon. Supp.*, 1:633–637, 2008. [arXiv:0710.4124].

[47] Claude A. Pruneau, Sean Gavin, and Sergei A. Voloshin. Transverse Radial Flow Effects on Two- and Three-Particle Angular Correlations. *Nucl. Phys.*, A802: 107–121, 2008. [arXiv:0711.1991].

[48] Rudolph C. Hwa. Hadron Correlations in Jets and Ridges through Parton Recombination. 2009. [arXiv:0904.2159].

[49] J. L. Nagle. Ridge, Bulk, and Medium Response: How to Kill Models and Learn Something in the Process. *Nucl. Phys.*, A830:147c–154c, 2009. [arXiv:0907.2707].

[50] Jean-Yves Ollitrault. Anisotropy as a signature of transverse collective flow. *Phys. Rev.*, D46:229–245, 1992.

[51] S. Voloshin and Y. Zhang. Flow study in relativistic nuclear collisions by Fourier expansion of Azimuthal particle distributions. *Z. Phys.*, C70:665–672, 1996. [arXiv:hep-ph/9407282].

[52] J. Barrette et al. Observation of anisotropic event shapes and transverse flow in Au + Au collisions at AGS energy. *Phys. Rev. Lett.*, 73:2532–2535, 1994. [arXiv:hep-ex/9405003].

[53] J. Barrette et al. Energy and charged particle flow in 10.8-A-GeV/c Au + Au collisions. *Phys. Rev.*, C55:1420–1430, 1997. [arXiv:nucl-ex/9610006].

[54] C. Alt et al. Directed and elliptic flow of charged pions and protons in Pb + Pb collisions at 40-A-GeV and 158-A-GeV. *Phys. Rev.*, C68:034903, 2003. [arXiv:nucl-ex/0303001].

[55] K. H. Ackermann et al. Elliptic flow in Au + Au collisions at $\sqrt{s_{\rm NN}} = 130$ GeV. *Phys. Rev. Lett.*, 86:402–407, 2001. [arXiv:nucl-ex/0009011].

[56] Henning Heiselberg and Anne-Marie Levy. Elliptic flow and HBT in non-central nuclear collisions. *Phys. Rev.*, C59:2716–2727, 1999. [arXiv:nucl-th/9812034].

[57] S. A. Voloshin and Arthur M. Poskanzer. The physics of the centrality dependence of elliptic flow. *Phys. Lett.*, B474:27–32, 2000. [arXiv:nucl-th/9906075].

[58] Sergei A. Voloshin, Arthur M. Poskanzer, and Raimond Snellings. Collective phenomena in non-central nuclear collisions. 2008. [arXiv:0809.2949].

[59] Paul Sorensen. Elliptic Flow: A Study of Space-Momentum Correlations In Relativistic Nuclear Collisions. 2009. [arXiv:0905.0174].

[60] P. Kovtun, D. T. Son, and A. O. Starinets. Viscosity in strongly interacting quantum field theories from black hole physics. *Phys. Rev. Lett.*, 94:111601, 2005. [arXiv:hep-th/0405231].

[61] R. S. Bhalerao, Jean-Paul Blaizot, Nicolas Borghini, and Jean-Yves Ollitrault. Elliptic flow and incomplete equilibration at RHIC. *Phys. Lett.*, B627:49–54, 2005. [arXiv:nucl-th/0508009].

[62] Tetsufumi Hirano. Relativistic hydrodynamics at RHIC and LHC. *Prog. Theor. Phys. Suppl.*, 168:347–354, 2007. [arXiv:0704.1699].

[63] Pasi Huovinen. Chemical freeze-out temperature in hydrodynamical description of Au+Au collisions at $\sqrt{s_{\rm NN}} = 200$ GeV. *Eur. Phys. J.*, A37:121–128, 2008. [arXiv:0710.4379].

[64] Michael L. Miller, Klaus Reygers, Stephen J. Sanders, and Peter Steinberg. Glauber modeling in high energy nuclear collisions. *Ann. Rev. Nucl. Part. Sci.*, 57:205–243, 2007. [arXiv:nucl-ex/0701025].

[65] B. Alver et al. Importance of Correlations and Fluctuations on the Initial Source Eccentricity in High-Energy Nucleus-Nucleus Collisions. *Phys. Rev.*, C77: 014906, 2008. [arXiv:0711.3724].

[66] B. Alver, M. Baker, C. Loizides, and P. Steinberg. The PHOBOS Glauber Monte Carlo. 2008. [arXiv:0805.4411].

[67] H. de Vries, C.W. de Jager, and C. de Vries. *Atomic Data and Nuclear Data Tables*, 36:495, 1987.

[68] B. Alver et al. System size dependence of cluster properties from two- particle angular correlations in Cu+Cu and Au+Au collisions at $\sqrt{s_{\rm NN}} = 200$ GeV. *Phys. Rev.*, C81:024904, 2010. [arXiv:0812.1172].

[69] B. Alver and G. Roland. Collision geometry fluctuations and triangular flow in heavy-ion collisions. *to appear in Phys. Rev.*, C, 2010. [arXiv:1003.0194].

[70] Zi-Wei Lin, Che Ming Ko, Bao-An Li, Bin Zhang, and Subrata Pal. A multi-phase transport model for relativistic heavy ion collisions. *Phys. Rev.*, C72: 064901, 2005. [arXiv:nucl-th/0411110].

[71] G. L. Ma et al. Di-hadron azimuthal correlation and Mach-like cone structure in parton / hadron transport model. *Phys. Lett.*, B641:362–367, 2006. [arXiv:nucl-th/0601012].

[72] G. L. Ma et al. Longitudinal broadening of near side jets due to parton cascade. *Eur. Phys. J.*, C57:589–593, 2008. [arXiv:0807.3987].

[73] S. Zhang et al. Transverse momentum and pseudorapidity dependences of Mach-cone like correlations for central Au + Au collisions at $\sqrt{s_{\rm NN}} = 200$ GeV. *Phys. Rev.*, C76:014904, 2007. [arXiv:0706.3820].

[74] W. Li et al. Reaction Plane Angle Dependence of Di–Hadron Azimuthal Correlations in a Multi-Phase Transport Model. 2009. [arXiv:0903.2165].

[75] Miklos Gyulassy and Xin-Nian Wang. HIJING 1.0: A Monte Carlo program for parton and particle production in high-energy hadronic and nuclear collisions. *Comput. Phys. Commun.*, 83:307, 1994. [arXiv:nucl-th/9502021].

[76] B. I. Abelev et al. Charge Independent(CI) and Charge Dependent(CD) correlations vs. Centrality from $\Delta\phi\Delta\eta$ Charged Pairs in Minimum Bias Au + Au Collisions at 200 Gev. 2008. [arXiv:0806.0513].

[77] John Adams et al. Minijet deformation and charge-independent angular correlations on momentum subspace (eta, phi) in Au-Au collisions at $\sqrt{s_{\rm NN}} = 130$ GeV. *Phys. Rev.*, C73:064907, 2006. [arXiv:nucl-ex/0411003].

[78] B. I. Abelev et al. Identifying the physics of the ridge via three-particle $\Delta\eta$-$\Delta\eta$ correlations in high energy nucleus-nucleus collisions. 2009. [arXiv:0912.3977].

[79] R. Hollis. *Centrality Evolution of Charged Particles Produced in Ultra-relativistic Au+Au and d+Au Collisions.* PhD thesis, University of Illinois at Chicago, 2005.

[80] R. Bindel, E. García, A. C. Mignerey, and L. P. Remsberg. Array of scintillator counters for PHOBOS at RHIC. *Nucl. Instrum. Meth.*, A474:38–45, 2001.

[81] Clemens Adler et al. The RHIC zero degree calorimeters. *Nucl. Instrum. Meth.*, A470:488–499, 2001. [arXiv:nucl-ex/0008005].

[82] W. Fischer et al. Electron cloud observations and cures in the Relativistic Heavy Ion Collider. *Phys. Rev. ST Accel. Beams*, 11:041002, 2008.

[83] B. B. Back et al. The PHOBOS detector at RHIC. *Nucl. Instrum. Meth.*, A499: 603–623, 2003.

[84] R. Nouicer et al. Silicon pad detectors for the PHOBOS experiment at RHIC. *Nucl. Instrum. Meth.*, A461:143–149, 2001. [arXiv:nucl-ex/0208006].

[85] P. Sarin. *Measurement of Charged Particle Multiplicity Distributions in Au+Au Collisions up to 200 GeV.* PhD thesis, Massachusetts Institute of Technology, 2003.

[86] P. Decowski. *Energy and Centrality Dependence of Mid-Rapidity Charged Particle Multiplicity in Relativistic Heavy-Ion Collisions.* PhD thesis, Massachusetts Institute of Technology, 2002.

[87] B. B. Back et al. Centrality and pseudorapidity dependence of elliptic flow for charged hadrons in Au + Au collisions at $\sqrt{s_{\rm NN}} = 200$ GeV. *Phys. Rev.*, C72: 051901, 2005. [arXiv:nucl-ex/0407012].

[88] Arthur M. Poskanzer and S. A. Voloshin. Methods for analyzing anisotropic flow in relativistic nuclear collisions. *Phys. Rev.*, C58:1671–1678, 1998. [arXiv:nucl-ex/9805001].

[89] B. Alver et al. Event-by-event fluctuations of azimuthal particle anisotropy in Au+Au collisions at $\sqrt{s_{\rm NN}} = 200$ GeV. *Phys. Rev. Lett.*, 104:142301, 2010. [arXiv:nucl-ex/0702036].

[90] B. B. Back et al. Energy dependence of elliptic flow over a large pseudorapidity range in Au + Au collisions at RHIC. *Phys. Rev. Lett.*, 94:122303, 2005. [arXiv:nucl-ex/0406021].

[91] Hans-Joachim Drescher and Yasushi Nara. Eccentricity fluctuations from the Color Glass Condensate at RHIC and LHC. *Phys. Rev.*, C76:041903, 2007. [arXiv:0707.0249].

[92] B. B. Back et al. Pseudorapidity and centrality dependence of the collective flow of charged particles in Au + Au collisions at $\sqrt{s_{\mathrm{NN}}} = 130$ GeV. *Phys. Rev. Lett.*, 89:222301, 2002. [arXiv:nucl-ex/0205021].

[93] B. Alver et al. Non-flow correlations and elliptic flow fluctuations in gold-gold collisions at $\sqrt{s_{\mathrm{NN}}} = 200$ GeV. *Phys. Rev.*, C81:034915, 2010. [arXiv:1002.0534].

[94] B. Alver et al. Cluster properties from two-particle angular correlations in p + p collisions at $\sqrt{s} = 200$ GeV and 410 GeV. *Phys. Rev.*, C75:054913, 2007. [arXiv:0704.0966].

[95] R. E. Ansorge et al. Charged Particle Correlations in Anti-p+p collisions at C.M. Energies of 200 GeV, 546 GeV and 900GeV. *Z. Phys.*, C37:191–213, 1988.

List of Figures

Acknowledgments

Very early in the Ph.D. program, I discovered that doing research is a vastly different and a much more challenging task compared to learning about the research done previously by others. Even though there are many people I need to thank for the support and assistance they provided in making this thesis possible, I would like to start by singling out three people, who have played most crucial roles in my education to become a scientist. First and foremost, I would like to thank my advisor Gunther Roland. He is a role model both as a visionary and enthusiastic scientist and as a supportive advisor, who gives his students the confidence to become independent researchers. This thesis is a direct result of his guidance, and I am deeply indebted to him for his support over the years. Along with my advisor, it has been a great pleasure to work under the mentorship of Wit Busza and Constantin Loizides. Wit constantly reminded all of us not to get lost in the technical details, to always think about the underlying physics, and to give the care needed in communicating our work. Constantin has been another great role model as a young motivated scientist and a great colleague who, when I did get lost in the technical details, was always there to teach me the way out.

The heavy ion physics group at MIT has been an inspiring environment. Bolek Wyslouch and George Stephans have been great senior colleagues, both during physics discussions and during the brief period when I "managed" the Tier2 computing center. In my first years, I was fortunate to work with and learn from the senior students, Conor Henderson and Corey Reed and postdocs Kris Gulbrandsen and Gabor Veres. In particular, Gabor was a fun railroad trip mate in India. Constantin, Corey, Kris, Ilya Kravchenko and Maarten Ballintijn have shared with me their technical expertise. It has been fun and stimulating working in a multi-cultural environment with fellow students Wei Li, Edward Wenger and Siarhei Vaurynovich. Wei's work on two-particle correlation analysis founded the base of the non-flow correlation studies in this thesis. I would also like to thank Anna Maria Convertino for her excellent administrative work and Sean Thompson for his technical support.

I was very fortunate to have the opportunity to work with great colleagues in PHOBOS. I should thank Wit and Gunther once again, as they were not only great mentors for me but also played crucial roles, as the spokesperson and the analysis coordinator in the success PHOBOS has been. The flow fluctuations committee, Barbara Wosiek, Steve Manly and Constantin worked very hard to ensure the quality of the data presented in this thesis. Peter Steinberg has made the meetings colorful and exciting by having different opinions from my advisor 80-90% of the time. David Hofman, Vasundhara Chetluru and Richard Bindel have made the PHOBOS meetings memorable, in particular, sharing the tequila Vasu brought to the Maryland meetings.

I would like to thank Andrzej Olszewski and Krzysztof Woźniak, and Marguerite Tonjes for their work on Monte Carlo simulations and data production. As the youngest member (I believe), I joined the collaboration on the last year of data-taking and have missed out on the chance to work closely with a number of members who worked very hard to build the detector and provide the high quality data analyzed in this thesis. I would like to thank all members of the PHOBOS collaboration for the "beautiful" data.